A Fluctuational Electrodynamic Analysis of Microscale Radiative Transfer and the Design of Microscale Thermophotovoltaic Devices

by

MacMurray Davidson Whale

Bachelor of Applied Science in Mechanical Engineering
(University of Toronto, 1990)

Master of Science in Mechanical Engineering
(M.I.T., 1992)

Submitted to the Department of Mechanical Engineering in
partial fulfillment of the requirements for the degree of

Doctor of Philosophy in Mechanical Engineering

at the

MASSACHUSETTS INSTITUTE OF TECHNOLOGY

June 1997

Author .....
Department of Mechanical Engineering
May 9, 1997

Certified by .....
Professor Ernest G. Cravalho
Thesis Supervisor
Department of Mechanical Engineering

Accepted by.....
Professor Ain A. Sonin
Chairman
Departmental Committee on Graduate Studies

A Fluctuational Electrodynamic Analysis of Microscale Radiative Transfer and the Design of Microscale Thermophotovoltaic Devices

by

MacMurray Davidson Whale

Submitted to the Department of Mechanical Engineering on
May 9, 1997 in partial fulfillment of the requirements for the
degree of Doctor of Philosophy in Mechanical Engineering

Abstract

The Stefan-Boltzmann Law has served as the basis for the analytical determination of energy transport between thermally radiating bodies for over 100 years. For systems whose physical dimensions are on the order of the characteristic wavelength of the radiation, ample theoretical and experimental evidence substantiates the significant departure from the Stefan-Boltzmann Law. The experimental data, however, do not correlate well with each other, nor do the theoretical predictions adequately explain the discrepancies.

To explain these inconsistencies, this thesis identifies a set of microscale radiative transfer regimes based on the electron-photon interactions responsible for the absorption in the participating surfaces. Since the data from the various experimental configurations lie in different regimes, the disagreement among the measurements can be traced to the differences in the absorption process. Only measurements that lie in the regime consistent with the basis of the fluctuational electrodynamic formulation agree with the prediction.

The fluctuational electrodynamic approach to microscale radiative transfer arises from the incorporation of the fluctuation-dissipation theorem in Maxwell's equations. This formalism accounts for wave interference and radiation tunneling of the thermal field and provides a rigorous account of the statistical nature of its source. This thesis indicates fundamental limitations of the current approximations to this formalism and presents the derivation of a new proximity function applicable over the entire range of temperature and spacing for which the general formalism is valid. The proximity function indicates the spectral details of the spacing effect, permitting analysis and design of microscale thermal systems.

A new class of energy conversion devices, called microscale thermophotovoltaic devices, is proposed and analyzed using a numerical computation of the full fluctuational electrodynamic formulation. The devices are modeled as pn-junctions of $In_{1-x}Ga_xAs$ and $Hg_{1-x}Cd_xTe$. The results indicate the influence of temperature, alloy composition, doping, and vacuum gap on performance. Microscale radiative transfer can increase power density ten fold without loss of efficiency, thereby reducing initial costs, while decreasing size and weight of such systems. A model of the microscale device is presented and employed to identify the important parameters for the future development of this technology.

Thesis Supervisor: Prof. Ernest G. Cravalho

Title: Professor of Mechanical Engineering

Acknowledgments

I would like thank my thesis committee, Prof. J.L. Smith, Jr., Prof. C.G. Fonstad, Jr., and Dr. J.C. Weaver for their helpful comments and suggestions, in particular, the chairman of the committee and my advisor, Prof. E.G. Cravalho. In the innumerable discussions with Prof. Cravalho throughout this work, I not only gained much from his valuable technical insight, but I learned how to think and write clearly and thoroughly. I thank him for making my doctoral studies, particularly near the end, so enjoyable even as we traveled through some new and often unfamiliar territory.

This desire to explore the unfamiliar was made much easier by many others at MIT, whose insight, though of a non-technical nature, influenced my life and indirectly improved the quality of this work. I thank Col. Kandiah, my boxing coach for the past three years, whose encouragement, wisdom, and goodwill provided support far outside the boxing ring. I am also indebted to Associate Provost Alan Brody, Senior Lecturer Michael Ouellette, and Prof. Janet Sonenberg of the Theater Arts section. I gained much from their generosity of spirit, passion to explore, and commitment to the students and theater arts at MIT. All that I learned from them through the many hours of hard work on theater productions served me well for my thesis defense. I continue to discover new insights from their teaching that informs how I do my work, giving me confidence in the results of my exploration of both science and art.

I wish to thank my colleagues in the Cryogenic Engineering Lab, in particular, Chris Malone and Jeff Hebb, whose friendship supported me through many of the toughest and yet most enjoyable times of my work on this project and my life in Boston. I thank Danielle Tarraf with whom I shared the teaching assistantship of the undergraduate thermodynamics course, making my first teaching experience such a rewarding one.

I cannot fully express how important the love and encouragement of my parents and sisters have been to me. Their patience and support have been a constant source of strength, which helped to renew my focus, kept up my spirits, and permitted me to complete this work.

Biographical Note

MacMurray D. Whale was born February 11, 1967, in Ajax, Ontario, Canada. He attended the University of Toronto from September 1986 until June 1990 when he received a Bachelor of Applied Science with Honors in Mechanical Engineering. He ranked first in his class and was named a 1967 Science and Engineering Scholar by the Natural Sciences and Engineering Research Council of Canada. Prof. C. Ross Ethier advised his bachelor thesis entitled, "Regional Variability of the Juxtacanalicular Tissue." This thesis was presented by Prof. Ethier at the 9th International Congress of Eye Research, July 29-August 4, 1990, Helsinki, and it appears in *Proc. Int. Soc. Eye Res.*, Vol. 6, p. 82 as "Effects of Regional JCT Variability on Outflow," written by C.R. Ethier, M.D. Whale, F.M. Coloma, and A.W. de Kater.

From May 1990 until September 1992, the author studied in the Fluid Mechanics Laboratory at the Massachusetts Institute of Technology where he earned a Master of Science degree. Dr. Mark Johnson supervised his thesis entitled, "The Measurement of Specific Hydraulic Conductivity of Human and Bovine Aortic Wall," which was published in 1996 in *Biorheology*, Vol. 33, No. 1, pp. 17-44 as "The Effect of Aging and Pressure on the Specific Hydraulic Conductivity of the Aortic Wall," written by M.D. Whale, A.J. Grodzinsky, and M. Johnson.

In the summer of 1992, the author moved to the Cryogenic Engineering Laboratory where his focus changed from fluid mechanics to thermodynamics and heat transfer. The author was a teaching assistant for the undergraduate thermodynamics course in the Department of Mechanical Engineering and for a graduate course in the Department of Electrical Engineering taught by Prof. Grodzinsky entitled, "Fields, Forces, Flows: Background to Physiology." He worked during the summer of 1996 at BlazeTech Corp. in Cambridge, MA where he wrote a report to the FAA on "The Potential for Fuel Tank Fire and Hydrodynamic Ram Initiated by Uncontained Engine Debris on Commercial Aircraft."

Several chapters from this thesis were presented at the 1997 National Heat Transfer Conference August 10-12 in Baltimore, MD. Chapter 3 was presented as a paper entitled, "Analysis of the Enhancement of Thermal Radiation between Closely-Spaced Metallic Surfaces Due to Microscale Phenomena." Chapter 4 was presented as a paper entitled, "Regimes of Microscale Radiative Transfer for the Exchange of Thermal Energy between Closely-Spaced Metallic Surfaces."

Contents

Nomenclature

D	=	carrier diffusion coefficient, $m^2\ s^{-1}$
$\mathbf{E}$	=	electric field vector, $V\ m^{-1}$
E	=	scalar fluctuational electric field, $V\ m^{-1}$
$\dot{E}$	=	rate of energy flux to receiver, $W\ m^{-2}$
FF	=	pn-junction fill-factor
G	=	electron-hole generation rate, $m^{-3}\ s^{-1}$
$\mathbf{H}$	=	magnetic field vector, $A\ m^{-1}$
H	=	scalar fluctuational magnetic field, $A\ m^{-1}$
I	=	spectral intensity, $W\ m^{-2}\ \mu m^{-1}\ sr^{-1}$
I_e	=	Hertzian dipole current, A
I_L	=	light-generated current, $A\ m^{-2}$
I_{sc}	=	short-circuit current, $A\ m^{-2}$
L	=	effective active region of the pn-junction = L_e+W+L_h, m
L_0	=	active region of the pn-junction at large vacuum gap, m
L_e	=	electron diffusion length, m
L_h	=	hole diffusion length, m
M	=	proximity function (sum of polarizations), m^{-2}
M_W	=	molecular weight, $kg\ kgmole^{-1}$
N	=	electron or hole number density, m^{-3}
N_{Av}	=	Avogadro's number = $6.02 \times 10^{26}\ kgmole^{-1}$
P	=	net radiative energy flux, $W\ m^{-2}$
$\dot{Q}_c$	=	rate of heat loss from receiver, $W\ m^{-2}$
$\dot{Q}_s$	=	rate of energy supplied to the emitter, $W\ m^{-2}$
Q_e	=	quantum efficiency
S	=	gap-dependent portion of proximity function
$\dot{S}$	=	rate of entropy flux to receiver, $W\ K^{-1}\ m^{-2}$
$\dot{S}_g$	=	rate of entropy generated in receiver, $W\ K^{-1}\ m^{-2}$
S_j	=	oscillator strength in permittivity fit
T	=	temperature, K
T_A	=	absolute thermodynamic temperature, K

T_F = effective flux temperature, K

U = internal energy, J

V_{bi} = built-in voltage, V

V_{oc} = open-circuit voltage, V

W = depletion width of the pn-junction, m

a_λ = absorption coefficient, cm^{-1}

c = speed of an electromagnetic wave in a vacuum = 3.0×10^8 m s^{-1}

d = size of vacuum gap size (separation of surfaces), m

d_e = size of Hertzian dipole, m

d_t = tidal displacement, m

e = electron charge = -1.602×10^{-19} C

e_b = black body emissive power, W m^{-2}

h = Planck's constant = 6.626×10^{-34} J s

i = square root of -1

$\mathbf{j}$ = electric current vector, A m^{-2}

$\mathbf{j}_{0e}$ = extraneous point electric current vector, A m^{-2}

$\mathbf{j}_{0m}$ = extraneous point magnetic current vector, V m^{-2}

$\mathbf{j}_e$ = random electric current vector, A m^{-2}

$j_{e\alpha}$ = αth element of the random electric current vector, A m^{-2}

$\mathbf{j}_m$ = random magnetic current vector, V m^{-2}

$j_{m\alpha}$ = αth element of the random magnetic current vector, V m^{-2}

k = 2π x wave number = ω/c, m^{-1}

$\mathbf{k}$ = wave vector, m^{-1}

k_b = Boltzmann constant = 1.381×10^{-23} J K^{-1}

k_x = x-component of the wave vector, m^{-1}

k_z = z-component of the wave vector, m^{-1}

l = heterojunction layer thickness, m

m = integer value of y

m_0 = electron rest mass = 9.11×10^{-31} kg

m^* = electron effective mass, kg

n = refractive index or summation index

n_b = Bose-Einstein statistical distribution

n_i = intrinsic carrier concentration, m^{-3}

n_j = mean occupancy number of state j

n_ν = spectral mean occupancy number

r = radial displacement from electric dipole, m

$\hat{r}$ = unit vector in the r-direction

t = integrand of M

y = dimensionless spacing = $2k_bTd/hc$

$\Phi_{p\lambda}$ = spectral photon flux, $m^{-2}\,s^{-1}\,\mu m^{-1}$

Φ_p = total photon flux density, $m^{-2}\,s^{-1}$

Γ_j = damping coefficient of oscillator in permittivity fit, cm^{-1}

Λ = mean free path, m

Θ = mean energy of a quantum oscillator, J

δ = penetration depth, m

δ_{ASE} = penetration depth in anomalous skin effect region, m

δ_{NSE} = penetration depth in normal skin effect region, m

$\varepsilon_{\alpha\beta}$ = element of the permittivity tensor, $C^2\,N^{-1}\,m^{-2}$

ϕ = angle, rad

$\hat{\phi}$ = vector in the ϕ-direction

η = efficiency

η_0 = impedance of free space, Ω

η_C = Carnot efficiency

κ = extinction coefficient or integration variable = ik_z

λ = wavelength, m

λ_{th} = thermal de Broglie wavelength, m

λ_W = wavelength at maximum emissive power (Wien's wavelength), m

μ = electron mobility, $m^2\,V^{-1}\,s^{-1}$

μ_0 = permeability of free space = $4\pi \times 10^{-7}$ H m^{-1}

$\mu_{\alpha\beta}$ = element of the permeability tensor, $N\,s^2\,C^{-2}$

ν = frequency, s^{-1}

θ = angle, rad

$\hat{\theta}$ = vector in the θ-direction

ρ = argument of k_z or k_z/ε, rad

σ = dc electrical conductivity, $\Omega^{-1}\,m^{-1}$

σ_{eff} = effective dc electrical conductivity, $\Omega^{-1}\,m^{-1}$

τ = electron scattering time, s

τ_A = carrier lifetime due to Auger recombination, s

τ_T = carrier lifetime due to trap recombination, s

υ_F = Fermi velocity, m s^{-1}

ω = angular frequency, rad s^{-1}

ω_p = plasma frequency, rad s^{-1}

Subscripts

0 = point current source or diffractional field due to point source

1 = material 1

2 = material 2

A = acceptor

D = donor

F = Fermi level

b = black body

c = conduction band

e = electric dipole

g = band gap

m = magnetic dipole

n = nth layer of heterojunction

p = photon

v = vacuum or valence band

$\alpha\beta$ = denotes an element of permittivity or permeability tensor

$\parallel$ = parallel polarization

$\perp$ = perpendicular polarization

Superscripts

top = top layer of heterojunction

bot = bottom layer of heterojunction

far = far field

near = near field

TPV = thermophotovoltaic

List of Figures

List of Tables

Chapter 1

Introduction

1.1 The Limitations of the Stefan-Boltzmann Radiation Law

1.1.1 The Discovery of the Spacing Effect

For nearly 100 years until the 1960's, the Stefan-Boltzmann Radiation Law had served as the primary tool for the analytical determination of energy transport between radiating bodies. The underlying theoretical foundation of this law grew out of an attempt by Max Planck in 1901 to formulate an empirical equation that fit the early experimental data for the spectral emissive power of a black body over the entire spectrum (Planck, 1959). Subsequently, Planck was able to derive the expression which now bears his name (from which the Stefan-Boltzmann Radiation Law can be derived) by postulating a set of assumptions that provided the basis for quantum theory. Since that time, the Stefan-Boltzmann Radiation Law has been the cornerstone of the theory of radiative heat transfer for engineering analysis.

In the mid-1960's, scientists and engineers, challenged by thermal radiation problems associated with the space effort, began to confront the limitations of this well-known law. The effectiveness of cryogenic thermal insulation, measured experimentally, did not agree with the predictions of the Stefan-Boltzmann Radiation Law (Emslie, 1962; Leung et al., 1979). The small spacing between adjacent layers within the insulation (Tien and Cunnington, 1973) violated one of the fundamental assumptions made by Planck. In *The Theory of Heat Radiation*, Planck states: "We are therefore obliged to

introduce right at the start a certain restriction with respect to the size of the parts of space to be considered. Throughout the following discussion it will be assumed that the linear dimensions of all parts of space considered... are large compared to the wave lengths of the rays considered". The long wavelength of radiation at cryogenic temperatures and the small system dimensions of multi-layered thermal insulation conspire to invalidate the original assumptions of Planck through the phenomena of *wave interference* and *radiation tunneling* between adjacent layers of metallic sheets (Born and Wolf, 1965). These phenomena play an important role in determining the effectiveness of many thermal insulation systems.

The effects of wave interference and radiation tunneling have been demonstrated experimentally. The measurements of Cravalho et al. (1968) and Domoto et al. (1970) indicate that the Stefan-Boltzmann Radiation Law is inadequate to describe the exchange of energy between closely-spaced thermally radiating bodies. In the ensuing decades, several experimental studies (Hargreaves, 1969; Hargreaves, 1973; Kutateladze et al., 1979) produced further evidence that the law is limited in its applicability. The proximity effect continues to be important today. Xu et al. (1994) have investigated the role of thermal radiation in scanning thermal microscopy and scanning tunneling microscopy, where the thermal contact between the tip and sample is important. These measurements, however, do not correlate well with each other.

Theoretical predictions, formulated to account for the spacing effect, do not provide suitable agreement to the measurements. Neither the earliest attempts, based on an intensity approach (Boehm and Tien, 1970), nor several analytical models (Polder and Van Hove, 1971; Caren, 1974; Levin et al., 1980; Loomis and Maris, 1994), which involve approximations to a fluctuational electrodynamics approach (Rytov et al., 1987) can account for the measured spacing effect. The lack of a detailed explanation for the

outstanding disagreements prevents the design and analysis of systems, which involve the spacing effect of thermal radiation.

1.1.2 The Importance of the Spacing Effect

Given the current state of technology relative to its status when this phenomenon was first reported, there now exist a number of situations of practical interest in which the spacing effect is operative and in some cases dominant. For example, the ever-growing development of micro-fabrication techniques means that practical devices (micro-structures and micro-machines) can now be built for which the relevant length scale is in the range where the spacing effect is important. This underscores the paramount importance of a fundamental understanding of the effect.

In addition, a deeper understanding of the fundamentals of radiative heat transfer for small surface spacing and at low temperatures may prove useful in the design of cryogenic thermal insulation. State-of-the-art cryogenic thermal insulation utilizes thin sheets of plastic, coated with highly-reflective layers of gold, silver, or aluminum and separated by a highly evacuated space. It is the high reflectance of such coatings that provides effective thermal insulation against radiative heat transfer. However, recent studies by Zhang et al. (1992) show that the reflectance of $YBa_2Cu_3O_7$, a high-T_c superconductor, in the far-infrared spectral region is near unity and even higher than that of gold. Since for temperatures below 30 K, a large portion of the radiative energy is emitted at long wavelengths, precisely where the reflectance of $YBa_2Cu_3O_7$ is the highest, these materials may be very attractive for optimizing super-insulation designs. Such optimization is possible only upon the validation of the existing predictions for radiative transfer that account for the spacing effect and the elucidation of their conditions of applicability.

The feasibility of devices that convert the thermal energy of a hot source to electrical energy by a thermophotovoltaic device may be determined (and their efficiency

improved) by a better understanding of the spacing phenomenon. Thermophotovoltaic devices utilize new semiconductor materials in which electron-hole pairs are created by the absorption of photons emitted by a surface at a higher temperature than the device (Coutts and Benner, 1994). A class of devices called microscale thermophotovoltaics has been proposed (DiMatteo, 1996), which will exploit the enhanced transfer of energy that occurs when bodies are very close. Such devices have the potential to utilize the high temperature source more effectively than conventional methods. The net result will be higher overall energy densities and potentially higher energy conversion efficiencies. The design and analysis of such devices requires a sound knowledge of radiative transfer at small spacing, which this thesis provides.

1.2 The Objectives of the Present Investigation

The objective of this thesis is two-fold: to clarify and address the outstanding issues in the study of the spacing effect, and to introduce and analyze the performance of a class of devices that exploit the spacing effect for enhanced energy conversion.

In order to deepen the understanding of the spacing effect, the first part of this thesis presents an evaluation of the existing predictions and an assessment of their applicability to the experimental measurements. Chapter 2 outlines the physical basis of the spacing effect, describes the two theories most widely used to make predictions, and surveys the results of existing experimental measurements. Chapter 3 examines approximations to the fluctuational electrodynamics approach to predict the spacing effect. This formulation is simplified for metallic and dielectric surfaces into relatively simple closed-form proximity functions. Regimes are developed that delineate the dependence of the net radiative flux on the surface separation to outline the applicability of the proximity-function formulation. Chapter 4 defines a set of microscale radiative transfer regimes for two thermally radiating bodies, thereby illustrating the problems inherent in comparing

the measurements and the predictions. The regimes provides a tool for use in designing a new set of experiments.

The remaining chapters concentrate on the analysis of a new class of energy conversion devices. Chapter 5 reviews thermophotovoltaic energy conversion devices and offers a concept that exploits microscale thermal radiation to enhance the performance of such devices. Performance parameters and the modifications to the existing theory that are necessary to apply the fluctuational electrodynamics approach to thermophotovoltaic materials are discussed. Chapter 6 presents the models used for the device materials, discusses the results of the analysis of the proposed devices, and explores the next phase of the development of such devices.

Chapter 2

Predictions and Measurements of Microscale Radiative Transfer

2.1 The Basis of the Spacing Effect

Thermal radiation emitted by a solid surface is the fluctuation of an electromagnetic field produced by the random thermal motion of electrons associated with the atoms that make up the solid. The random thermal motion of such charged particles produces radiation that covers a broad spectrum of frequencies. This radiation field can be modeled as a collection of quantized dipole oscillators with frequencies distributed according to the Boltzmann distribution at equilibrium (Rytov et al., 1987). The field of each oscillator is comprised of two components, a near field and a far field. The solution of Maxwell's equations for the field far from an electric dipole yields a propagating electromagnetic field with real and imaginary terms.

$$\begin{aligned} \mathbf{E} &= \hat{\theta}\frac{i\eta_0 k I_e d_e}{4\pi r} e^{-ikr}\sin\theta \\ \mathbf{H} &= \hat{\phi}\frac{ikI_e d_e}{4\pi r} e^{-ikr}\sin\theta \end{aligned} \tag{1}$$

where η_0 is the impedance of free space, I_e is the current flowing between charge reservoirs d_e apart, k is 2π times the wave number, and r, θ the coordinates of the point of observation. These traveling waves constitute the classical equilibrium thermal radiation first postulated by Planck (1959). The power transmitted by an oscillating electromagnetic field is characterized by the real part of the Poynting vector, the cross

product of the electric and magnetic fields. Therefore, the far field of the dipole transmits power by virtue of its non-zero real component of the Poynting vector. Thermal energy is exchanged when the traveling waves emitted by the oscillators in one body are absorbed by corresponding oscillators in the other body. As the distance of separation of the bodies becomes small, these waves experience multiple reflections that result in classical wave interference.

When considering radiative transfer of thermal energy between closely-spaced bodies, a second mode of radiative transfer must be taken into account. Near the axis of a dipole, the characterization of the wave field is more complex due to the presence of a rapidly decaying quasi-stationary field that extends only over a distance of the order of the wavelength of the radiation. The solution of Maxwell's equations in this neighborhood, the near field, yields an electromagnetic field consisting of a purely imaginary electric field and a purely real magnetic field.

$$\begin{aligned} \mathbf{E} &= \frac{-i\eta_0 I_e d_e}{4\pi k r^3}\left(\hat{r}2\cos\theta + \hat{\theta}\sin\theta\right) \\ \mathbf{H} &= \hat{\phi}\frac{I_e d_e}{4\pi r^2}\sin\theta \end{aligned} \tag{2}$$

The Poynting vector for this near field becomes complex and is dominated by purely imaginary terms. As a consequence, there is no net power flow out of this region when radiating into a vacuum, since the real part of the Poynting vector is zero. This field is often referred to as an *evanescent field*, because it is mathematically similar to the field associated with an internally reflected electromagnetic wave at the surface of a body. In this case, power flows parallel to the surface.

Consider the situation shown in Fig. 1; i.e. two semi-infinite materials separated by a vacuum gap of size *d*. When the distance of separation between the surfaces is small, the second surface lies within the spatially decaying quasi-stationary field of the first surface. The magnitude of the electric field at the surface of the second body is

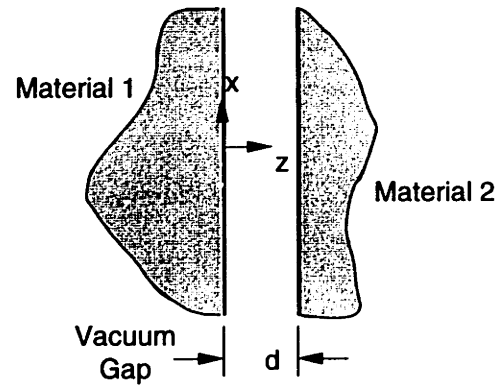

Figure 1: The system of two materials separated by a vacuum gap showing the coordinate system used in the theoretical formulation.

sufficiently large to affect the motion of the charges in this second body. The resulting electronic motion dissipates the energy of the near field and produces Joule heat. This mode of energy transfer has been called *radiation tunneling* (Born and Wolf, 1965). Since this near-field behavior is absent from the classical theory of thermal radiation, the classical theory cannot describe the electromagnetic fields in a cavity whose dimensions are of the order of, or smaller than, the wavelength of the radiation.

2.2 The Existing Theories of Microscale Radiative Transfer

There have been several attempts to predict the net radiative transfer between bodies that are closely-spaced by including the effects of both the near- and far-electromagnetic fields. For the case of absorbing media separated by a non-absorbing medium or vacuum, the theoretical predictions fall in one of two approaches. The intensity approach, which uses Planck's distribution for equilibrium black body radiation, is based on the energy balance for radiation across an interface. The fluctuational electrodynamics approach is based on stochastic Maxwell's equations and the thermal fluctuation of charges in a dissipative medium.

2.2.1 Intensity Approach

In this approach, developed by Boehm and Tien (1970), the source of the thermal radiation is not well specified. Instead, the intensity of radiation emitted by a particular medium is assumed to be related to the radiation intensity emitted by a black body in thermal equilibrium by a relation given by Fragstein (1950).

$$I(\omega,T)=\frac{n^4}{n^2+\kappa^2}e_b(\omega,T) \tag{3}$$

where n is the refractive index, κ is the extinction coefficient of the material and e_b is the black body emissive power. This expression is derived from the energy balance for normal incidence at an interface between a dissipative medium and vacuum assuming the vacuum to be filled with equilibrium black body radiation, and thus, the statistical nature of the source radiation is provided by Planck's distribution.

The electromagnetic waves propagate according to Maxwell's equations, and the presence of the dissipative media is introduced through the constitutive relations for the materials. By solving these equations subject to the boundary conditions of the medium-dielectric-medium system, the amplitude of the transmitted electric and magnetic fields can be found in terms of the incident fields on a particular interface. The solution of these equations automatically includes the effect of multiple reflections resulting in wave-interference and the radiation tunneling due to the quasi-stationary waves by integration over all frequencies through which the wave vector, **k**, assumes both real and imaginary values. The calculation of the energy flux is completed by combining the source statistics with the solution of the electric and magnetic fields for the system via the complex Poynting vector. The net radiative transfer is the difference between the amount of energy flux from the first medium to the second and the amount from the second to the first.

One problem with this is approach is the validity of the Fragstein relation. Rytov (1953) showed that this relation is inadequate for describing the intensity of radiation in an absorbing medium. Fragstein derived the equation under the assumption that the energy is transferred as a bundle of plane, non-extinguishable waves. The strong absorption of metals makes it impossible to represent the thermal radiation in an absorbing medium as a combination of such waves since the waves decay rapidly due to the absorption. Rytov (1953) showed that it is impossible, using Fresnel's formulas for plane waves, to derive Kirchoff's law for an isotropic material employing Eq. 3. For an anisotropic material, the relation given by Fragstein is valid for normal incidence only. Furthermore, the energy balance at each surface is strictly valid for normal incidence yet the transmission factors explicitly require a change in the critical angle of incidence in order to account for the quasi-stationary field.

2.2.2 Fluctuational Electrodynamics Approach

After Rytov (1953) pointed out that the thermal agitation of free and bound charges results in macroscopic, randomly fluctuating volume densities of charge and current which constitute the source of the thermal radiation, all subsequent theoretical predictions used a form of the fluctuation-dissipation theorem to model the source of the field. Polder and Van Hove (1971), Caren (1974), Levin et al (1980), and Loomis and Maris (1994) all use such an approach. There are several ways of accounting for these random currents depending upon the nature of the surface materials. Rytov et al. (1987) provide a particularly thorough explanation of this procedure and maintain a completely general approach that is suitable for gyrotropic and anisotropic materials. For the specific case of isotropic non-magnetic materials, Polder and Van Hove (1971) and Loomis and Maris (1994) present more detailed derivations. The approach of Rytov et al. (1987) is outlined here, since it illustrates the technique without being restricted to particular choices of material. This approach leads to the generally applicable result, which was reported but

not derived in Levin et al. (1980), and has yet to appear in the traditional heat transfer literature.

By introducing the random fluctuation sources, as macroscopic volume densities of the electric ($\mathbf{j}_e$) and magnetic currents ($\mathbf{j}_m$), into Maxwell's equations, the equations become stochastic in nature. Taking the Fourier transforms of Maxwell's equations and including these extraneous sources yields:

$$\operatorname{curl}\mathbf{H} = \frac{i\omega}{c}\mathbf{E} + \frac{4\pi}{c}\mathbf{j} + \frac{4\pi}{c}\mathbf{j}_e, \quad \operatorname{curl}\mathbf{E} = -\frac{i\omega}{c}\mathbf{H} - \frac{4\pi}{c}\mathbf{j}_m \tag{4}$$

These macroscopic currents, caused by the random thermal motion of microscopic charged particles (electrons), represent the source of the fluctuational field which constitutes radiation from the body. The random sources can be modeled using the fluctuation-dissipation theorem (Kubo, 1966). If the form of the random sources is known, the stochastic Maxwell's equations can be solved subject to the boundary conditions of the particular system to obtain expressions of the fluctuational fields due to the postulated sources. The solution of the stochastic Maxwell's equations automatically accounts for the traveling and quasi-stationary electric and magnetic fields in the space between the bodies since they are subject to the boundary conditions and material properties of the system and are valid for all values of the wave number.

It is less tedious, however, to use Maxwell's equations in the general integral form and write the solutions in terms of Green's functions. Green's functions have the same role for spatial problems that impulse-response functions have in temporal problems; they are the solutions to boundary-value problems with point field sources. A set of point electric and magnetic dipoles ($\mathbf{j}_{0e}$ and $\mathbf{j}_{0m}$) is postulated as an imaginary and deterministic source "causing" the observed charge and current fluctuations. The field formed by these extraneous sources is called a diffractional field ($\mathbf{E}_{0e}$, $\mathbf{H}_{0e}$ and $\mathbf{E}_{0m}$, $\mathbf{H}_{0m}$) in the literature and should be differentiated from the desired fluctuational field (Rytov et al., 1987). The

extraneous sources are completely arbitrary and are chosen carefully in order to obtain the necessary components of the source field in order to calculate the Poynting vector. The sources, $\mathbf{j}_{0e}$ and $\mathbf{j}_{0m}$, are chosen as point electric and magnetic dipoles so that the solution of Maxwell's equations yields the diffractional fields $\mathbf{E}_{0e}$ and $\mathbf{H}_{0e}$ (for $\mathbf{j}_e$) that are Green's functions (solutions of a boundary-value problem with point field sources).

The actual fluctuational field can be expressed in terms of the diffractional field by use of the electrodynamic reciprocity theorem, which relates the strengths and sources of two different fields for the same system of bodies and media (Rytov et al., 1987). This theorem, derived from two sets of Maxwell's equations, is valid for reciprocal media: those whose permittivity and permeability tensors are symmetric. By choosing the source currents of the diffractional fields as point sources in a particular direction, expressions for the desired components of the electric and magnetic fluctuational fields can be found in terms of the diffractional electric and magnetic fields and the correlation of the random currents.

$$\begin{aligned} E_{l_1} &= \int_V \{\mathbf{E}_{0e} \cdot \mathbf{j}_e - \mathbf{H}_{0e} \cdot \mathbf{j}_m\} d^3r \\ H_{l_2} &= -\int_V \{\mathbf{E}_{0m} \cdot \mathbf{j}_e - \mathbf{H}_{0m} \cdot \mathbf{j}_m\} d^3r \end{aligned} \tag{5}$$

where (l_1, l_2=x, y, z). The electric field in the x-direction is obtained by choosing $\mathbf{j}_{0e}$ as a unit vector in the x-direction while setting $\mathbf{j}_{0m}$ to zero. Thus, any component of the electromagnetic field can be obtained simply by choosing a new extraneous source in a particular direction.

Multiplying the components of the actual fluctuational fields by their complex conjugates and averaging over the equilibrium ensemble of $\mathbf{j}_e$ and $\mathbf{j}_m$ yields the products of the components of $\mathbf{E}$ and $\mathbf{H}$ that define the Poynting vector. The thermal radiation, in turn, can be calculated from the Poynting vector from the following expression.

$$\left\langle E_{l_1}(\mathbf{r}_1) H^*_{l_2}(\mathbf{r}_2) \right\rangle = -\iint E_{0e\alpha}(\mathbf{r}) E^*_{0m\beta}(\mathbf{r}') \left\langle j_{e\alpha}(\mathbf{r}) j^*_{e\beta}(\mathbf{r}') \right\rangle + H_{0e\alpha}(\mathbf{r}) H^*_{0m\beta}(\mathbf{r}') \left\langle j_{m\alpha}(\mathbf{r}) j^*_{m\beta}(\mathbf{r}') \right\rangle d^3\mathbf{r}\, d^3\mathbf{r}' \tag{6}$$

where ($\alpha,\beta = x, y, z$). The particular expressions for E_0 and H_0 come from the solution of Maxwell's equations with the boundary conditions for the particular system of bodies being considered (Grinberg, 1948). Equation 6 gives directly any desired moment of the electromagnetic field provided Maxwell's equations are solved and the correlation of the random extraneous currents is modeled.

The fluctuation-dissipation theorem for continuous systems provides the statistical correlation of the random currents. This theorem is a generalization of the approach derived by Nyquist (1928) to relate the voltage fluctuation in electrical systems to the electrical resistance. The fluctuation-dissipation theorem successfully describes irreversible processes (such as dissipation of energy in a resistor) in terms of the thermal equilibrium properties (voltage fluctuations) of the system. Kubo (1966) provides a general derivation of the fluctuation-dissipation theorem, which, when applied to Maxwell's equations, yields an expression for the covariance of extraneous currents for the radiating system.

$$\begin{aligned} \left\langle j_{e\alpha}(\mathbf{r}) j^*_{e\beta}(\mathbf{r}') \right\rangle &= -\frac{i\omega\Theta(\omega,T)}{2\pi}\left(\varepsilon_{\alpha\beta} - \varepsilon^*_{\beta\alpha}\right)\delta(\mathbf{r}-\mathbf{r}') \\ \left\langle j_{m\alpha}(\mathbf{r}) j^*_{m\beta}(\mathbf{r}') \right\rangle &= -\frac{i\omega\Theta(\omega,T)}{2\pi}\left(\mu_{\alpha\beta} - \mu^*_{\beta\alpha}\right)\delta(\mathbf{r}-\mathbf{r}') \end{aligned} \tag{7}$$

where $\varepsilon_{\alpha\beta}$ is an element in the permittivity tensor for a particular medium, $\mu_{\alpha\beta}$ is an element of the permeability tensor, and $\langle\ \rangle$ is the ensemble average. This expression shows that the electric and magnetic sources are not spatially correlated; the radius of the spatial correlation is zero as indicated by the delta function. The function Θ is the mean energy of a quantum oscillator.

$$\Theta(\omega,T)=\frac{h\omega/2\pi}{\exp\left(h\omega/2\pi k_b T\right)-1} \tag{8}$$

(Note: The mean energy of such an oscillator should include the additional term $h\omega/4\pi$. Since this "zero" oscillation will cancel out with the sources in the second material when considering the radiation from the second body to the first, it can be omitted.)

The fluctuation-dissipation theorem is valid for any frequency, the quantum region included, and is applicable to macroscopic systems of any physical form in thermal equilibrium. Such an equilibrium law can be used for non-equilibrium situations provided that the transport phenomena required to maintain steady-state conditions are insignificant when compared with the irreversible process of interest. (In the present case, the energy input required to maintain the temperature of the high-temperature surface must be insignificant compared to the energy emitted by that surface into the gap.)

All the necessary information is available to permit a calculation of the radiative transfer as a function of spacing. Substituting Eq. 7 in Eq. 6 and integrating yields,

$$\left\langle E_{l_1}(\mathbf{r}_1)H^*_{l_2}(\mathbf{r}_2)\right\rangle=-\frac{i\omega\Theta(\omega,T)}{2\pi}\times \int\left\{E_{0e\alpha}E^*_{0m\beta}\left(\varepsilon_{\alpha\beta}-\varepsilon^*_{\beta\alpha}\right)-H_{0e\alpha}H^*_{0m\beta}\left(\mu_{\alpha\beta}-\mu^*_{\beta\alpha}\right)\right\}d^3r \tag{9}$$

Consider two semi-infinite plane parallel bodies separated by a vacuum gap of size $z=d$, as depicted in Fig. 1. The z-component of the Poynting vector for energy flux in the electromagnetic field can be calculated for each medium radiating to the other.

$$P=\int_0^\infty P(\omega)d\omega=\int_0^\infty P_{12}(\omega)+P_{21}(\omega)d\omega \tag{10}$$

For steady-state conditions, the sources of the fluctuation in each medium are statistically independent, thus, both fields are incoherent. The net heat flux, therefore, is the sum of the heat flow from each surface to the other. This sum is evaluated by considering the

thermal field produced by the first medium while the second is present passively. The permittivity of the second medium, however, is calculated at the temperature of the second medium.

Because the electromagnetic field is incoherent, it is assumed that half the flux comes from the parallel polarization and half from the perpendicular polarization. The real part of the Poynting vector is:

$$P_{12}(\omega)=\frac{1}{2}\left\{\left\langle E_x H_y^*\right\rangle-\left\langle E_y H_x^*\right\rangle+\left\langle E_x^* H_y\right\rangle-\left\langle E_y^* H_x\right\rangle\right\} \tag{11}$$

By choosing the appropriate extraneous point sources, using Eq. 9 for each term in Eq. 11 determines the net radiative heat flux from material 1 to material 2.

For the case of isotropic materials which may have both complex permeability and permittivity, the solution of the boundary-value problem is of a simpler form, since the tensors reduce to single functions. For two semi-infinite plane parallel surfaces separated by a vacuum of size d, Levin et al. (1980), using the results of Grinberg (1948), report the following formulation.

$$\begin{aligned}
P_{12}(\omega) &= \frac{\Theta}{\pi^2}\left\{M_{\|}+M_{\perp}\right\}=\frac{\Theta M}{\pi^2} \\
M_{\|} &= \int_0^{\infty}\left\{\frac{1}{|\Delta_{\|}|^2}\left(\frac{k_{z1}}{\varepsilon_1}-\frac{k_{z1}^*}{\varepsilon_1^*}\right)\left(\frac{k_{z2}}{\varepsilon_2}-\frac{k_{z2}^*}{\varepsilon_2^*}\right)\right\}\left|k_{z_v}\right|^2 k_x dk_x \\
M_{\perp} &= \int_0^{\infty}\left\{\frac{1}{|\Delta_{\perp}|^2}\left(\frac{k_{z1}}{\mu_1}-\frac{k_{z1}^*}{\mu_1^*}\right)\left(\frac{k_{z2}}{\mu_2}-\frac{k_{z2}^*}{\mu_2^*}\right)\right\}\left|k_{z_v}\right|^2 k_x dk_x
\end{aligned} \tag{12}$$

where for the vacuum: $k_x^2+k_{z_v}^2=k^2$, for each material: $k_x^2+k_{z_j}^2=k^2\varepsilon_j\mu_j\,(j=1,2)$, $k=\omega/c$, and:

$$\begin{aligned}
\Delta_{\|} &= \left(\frac{k_{z1}}{\varepsilon_1}+k_{z_v}\right)\left(\frac{k_{z2}}{\varepsilon_2}+k_{z_v}\right)e^{k_{z_v}d}-\left(\frac{k_{z1}}{\varepsilon_1}-k_{z_v}\right)\left(\frac{k_{z2}}{\varepsilon_2}-k_{z_v}\right)e^{-k_{z_v}d} \\
\Delta_{\perp} &= \left(\frac{k_{z1}}{\mu_1}+k_{z_v}\right)\left(\frac{k_{z2}}{\mu_2}+k_{z_v}\right)e^{k_{z_v}d}-\left(\frac{k_{z1}}{\mu_1}-k_{z_v}\right)\left(\frac{k_{z2}}{\mu_2}-k_{z_v}\right)e^{-k_{z_v}d}
\end{aligned} \tag{13}$$

Wave Vector	Polder and Van Hove (1971) Eq. (19)	Levin et al. (1980) Eq. (5)	Loomis and Maris (1994) Eq. (21)
z- comp. in vacuum	k_{zv}	$-ip$	pk
z- comp. in material 1	k_z	$-ip_1$	$s_1 k$
z- comp. in material 2	k_z	$-ip_2$	$s_2 k$
x- component	k_x	χ	q
	d	l	l

Table 1: The equivalent notation for several fluctuational electrodynamics approaches for the prediction of the spacing effect.

This expression provides the starting point from which to derive the proximity functions that form the basis of the work in the next chapter. These expressions are equivalent to the general results presented in Polder and Van Hove (1971), Levin et al. (1980), and Loomis and Maris (1994), and can be converted to the particular notation of the other investigations by using Table 1. (It should be noted that Polder and Van Hove assumed that the two materials are characterized by the same material properties and that μ=1.) This table shows the wave vectors of the radiation field within each material and the vacuum space that separates them. Figure 2 shows the wave vectors on the complex plane for both low and high conductivity. This depiction will prove useful in the examination of the approximations made in each of these investigations (see Chapter 3). For $0<k_x<k$, the field in the vacuum is the familiar traveling-wave field (far field). When $k<k_x$, the field decays exponentially, thus accounting for the near-field effects.

In order to make a prediction, it is necessary to determine the material properties of the media and model their variation with temperature and frequency. Levin et al. (1980) made an impedance approximation and simplified the equations to examine the first order effects in surface impedance only. In this way the material properties of a particular medium were eliminated by assuming that either the anomalous skin effect or normal skin effect theory was sufficient to characterize the surface impedance (and in so doing it

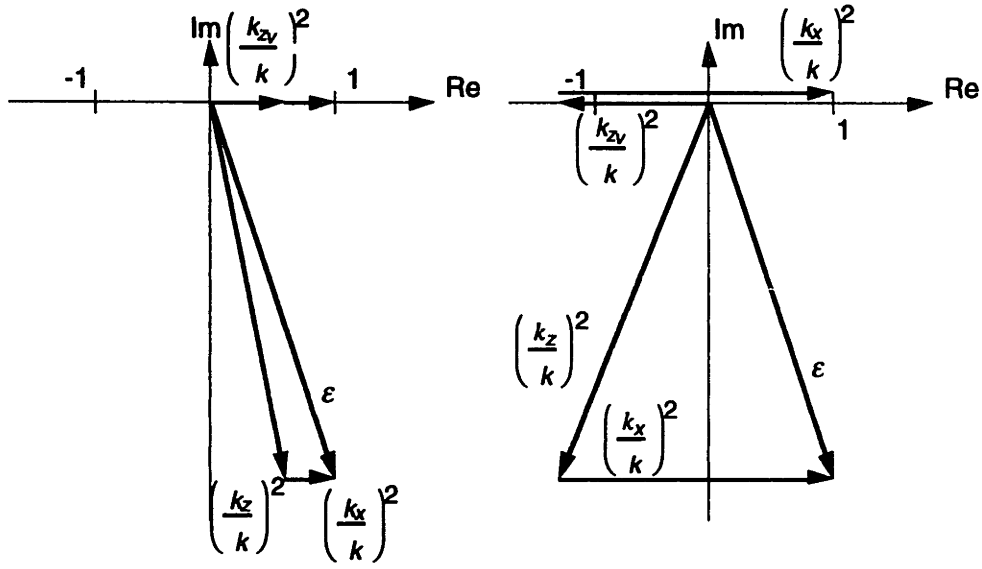

(a) a metal: $|\varepsilon|>>1$ so that $k_z \approx \sqrt{\varepsilon}k$

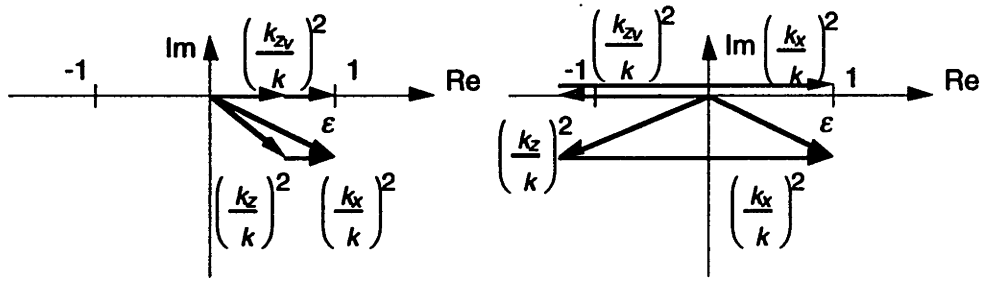

(b) a dielectric $|\varepsilon| \approx 1$ so that $k_z \approx k_{z_v}$

Figure 2: Wave vectors of the thermal radiation fields: (a) a metal (b) a dielectric.

was assumed that both media are in the same electronic transport region). By dividing the expression for the radiative transfer as a function of spacing by the expression at large spacing, the material-dependent properties cancel out leaving an expression which only depends on the first order power between surface impedance and frequency. The importance of these assumptions are discussed in the next chapter.

For the purpose of introducing the spacing effect, Figure 3 presents the results of the two approaches. Both theories indicate the same general trend in the spacing effect. Namely, a large increase in radiative transfer at small spacing and a region where the

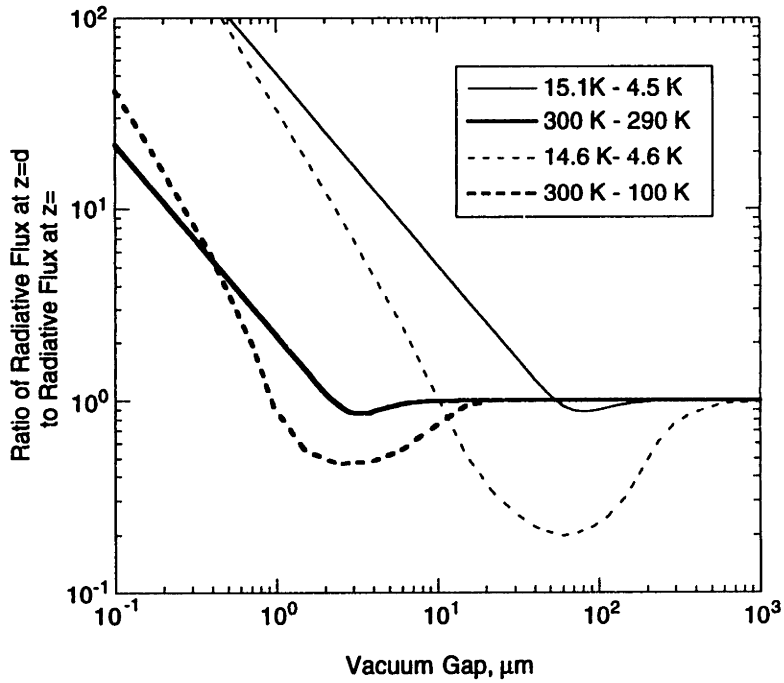

Figure 3: Predictions of the spacing effect on radiative transfer. Levin et al. (1980), solid line; Boehm and Tien (1970), broken line..

radiative transfer is less than that at large spacing marked by a clear minimum. The exact details, however, differ. At small spacing, the result of Boehm and Tien (1970) varies inversely with the fourth power of the spacing whereas the result of Levin et al. (1980) is inversely proportional to the first power. The spacing over which the heat flux is less than at large spacing is greater in the prediction of Boehm and Tien (1970), and the minimum is an order of magnitude greater. A more detailed examination of the theoretical predictions is given in Chapter 3, but first the experimental evidence of the spacing effect is presented.

2.3 Experimental Measurements of Microscale Radiative Transfer

All the reported experimental investigations of the spacing effect examined the radiative transfer between plane parallel metallic surfaces but used different techniques to measure the magnitude of the effect. Domoto et al. (1970) and Kutateladze et al. (1979) performed experiments on bulk copper disks using a calorimetric technique, which

utilized the calibration of a thermal link of low thermal conductance to make the measurements of the net radiative transfer. Hargreaves (1973) devised an electrical input method which utilizes a guard enclosure maintained at a temperature very close to the temperature of the emitter. Hargreaves reports the results of eight experiments using chromium films near room-temperature with a small temperature difference between the surfaces. Xu et al. (1994) measured the effect of spacing on the net flux between a planar thermocouple and the flattened tip of a needle mounted on a piezoelectric tube.

An understanding of the specific details of each of these investigations is important in order to assess the validity of comparisons made to the theory presented in the previous section. These details provide the framework for the regimes of microscale radiative transfer formed in Chapter 4.

First, consider the calorimetric technique used by Cravalho et al. (1968) and Domoto et al. (1970). From a common base plate hangs an emitter surface (high temperature) and a thermal link of low thermal conductance. This link supports the receiver surface (low temperature) opposite the emitter. Prior to making a particular measurement, the thermal link is calibrated: the receiver surface is maintained at an elevated temperature by dissipating a known amount of energy in a heater, and the temperature difference across the thermal link is measured. The calibration curve, thus obtained, gives the energy flux transferred to the receiver in terms of the temperature difference across the thermal link. To measure the radiative flux as a function of the gap size, the emitter is maintained at a particular temperature and the temperature difference across the thermal link is measured as the gap dimension is varied. The calibration curve converts this temperature difference to a quantitative measure of the energy transferred from the emitter to the receiver.

Domoto et al. (1970) and Cravalho et al. (1968) used this apparatus to measure the net radiative heat flux between two copper surfaces at 4.5 K and 10 K by submerging the

evacuated apparatus in a liquid helium bath. Kutateladze et al. (1979) used a similar technique, but did not provide a detailed description of the apparatus. The large uncertainty in the results was due to a number of limitations of the apparatus. A single mechanical feedthrough for positioning the samples was inadequate to determine or maintain surface parallelism. While a micrometer at the end of this feedthrough provided some measure of the surface spacing, there was no provision for a direct precise measurement of the surface separation. The calibration process may not have ensured that the conditions during the experiments were the same as during the calibration. The calibration procedure, however, provides a means to incorporate all the extraneous losses within the calibration. The heating of the plates was provided by lumped resistors rather than a more uniformly distributed heater wire; therefore, the temperature distribution across each surface may not have been uniform. The low-conductance of the thermal link resulted in long time constants, which reduced the amount of data that could be taken, increased helium consumption, and raised uncertainty as to whether sufficiently steady-state operation had been reached.

Hargreaves (1973) measured the net heat flux with less uncertainty by devising an apparatus that used an electrical-input method. This type of apparatus works well for closely-spaced bodies at room temperature. A guard enclosure completely surrounds the hot surface except where it faces the cold one. By maintaining a very small temperature difference between the guard and the hot surface, all the electrical power dissipated in the heater on the back of the hot surface radiates to the cold surface. The heater power required to maintain the temperature of the hot surface as it is moved relative to the cold surface becomes a measure of the heat flux. Hargreaves (1973) measured the separation of the surfaces in a more nearly direct manner by measuring the capacitance between the chromium surfaces. Three piezoelectric stacks, which could be precisely regulated to give accurate and repeatable control of the surface spacing to 1 μm, positioned the

samples. This technique requires more sophisticated equipment than the calorimetric technique, and therefore, is expensive and complex. Windows used for examination of interference fringes reduced the accuracy at lower temperatures. Conduction losses through the supports between the hot surfaces and the guard enclosure limited the precision at low temperatures. The technique does reduce the time constant dramatically, provides accurate spacing control, and directly measures the energy being supplied to the hot plate.

Xu et al. (1994) measured the net heat flux between two-metallic surfaces separated by less than 1 μm. In this apparatus, the flattened tip of an indium needle and the upper surface of a planar thermocouple comprised the two parallel surfaces between which the flux was measured. A resistance wire around the needle provided electrical heating, while a thermoelectric junction (Ag90/Cu10-Cr) mounted on a glass plate produced a temperature-dependent voltage in response to the thermal energy exchange between the needle and the junction. A piezoelectric transducer provided movement of the needle. The system was installed in a high-vacuum chamber with vibration isolation and electric shielding. Xu et al. (1994) measured both ac and dc thermoelectric voltages and lowered (by a factor of 100) the detection noise level from the results of Hargreaves (1973). The results were less sensitive, however, because the surfaces were much smaller in area (by a factor of 10^5). Xu et al. (1994) present measurements about two mean gap sizes, which indicate a much lower variation with gap size than indicated by the theoretical prediction. Xu et al. (1994) do not give absolute temperatures for each surface, and their analysis yields only the temperature difference. While this technique is promising, independent control and monitoring of the temperature of each surface would allow better comparison with the earlier measurements.

Figure 4 presents all the published data of the spacing effect on radiative transfer available in the literature. (The results of Xu et al. (1994) are not included, since they

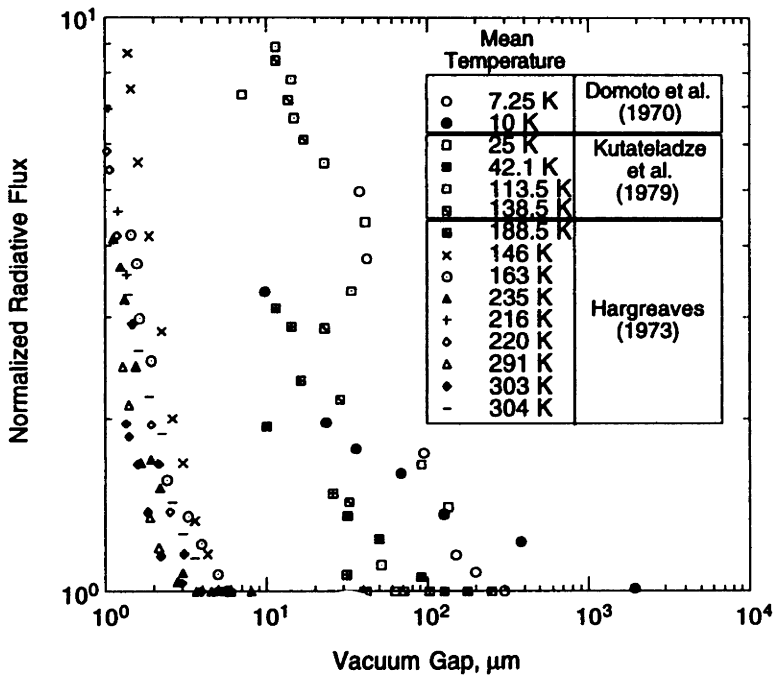

Figure 4: Measurements of the normalized net radiative flux versus gap size for metallic surfaces.

report only two values without the corresponding absolute temperature.) To normalize the data, the net radiative flux at a particular gap was divided by the net radiative flux at large spacing. As the spacing between the surfaces diminishes, there is an obvious and substantial increase in the net radiative flux. While the data do not demonstrate a clear trend, a number of features are evident. As the mean temperature decreases, the enhanced radiative heat flux begins at longer gap sizes, as expected since the energy is transferred by increasingly longer wavelengths at lower temperatures. As a result, the traveling waves are cut-off and the near-field of one surface begins to transfer energy to the opposite surface at a larger gap than for a higher mean temperature.

Several more distinct features become clear when the data are presented in terms of a dimensionless gap. Levin et al. (1980) simplified their expressions for the theoretical prediction by using a dimensionless gap, defined as the ratio of the surface spacing to one half the characteristic wavelength, λ, which is approximately 5 times Wien's wavelength.

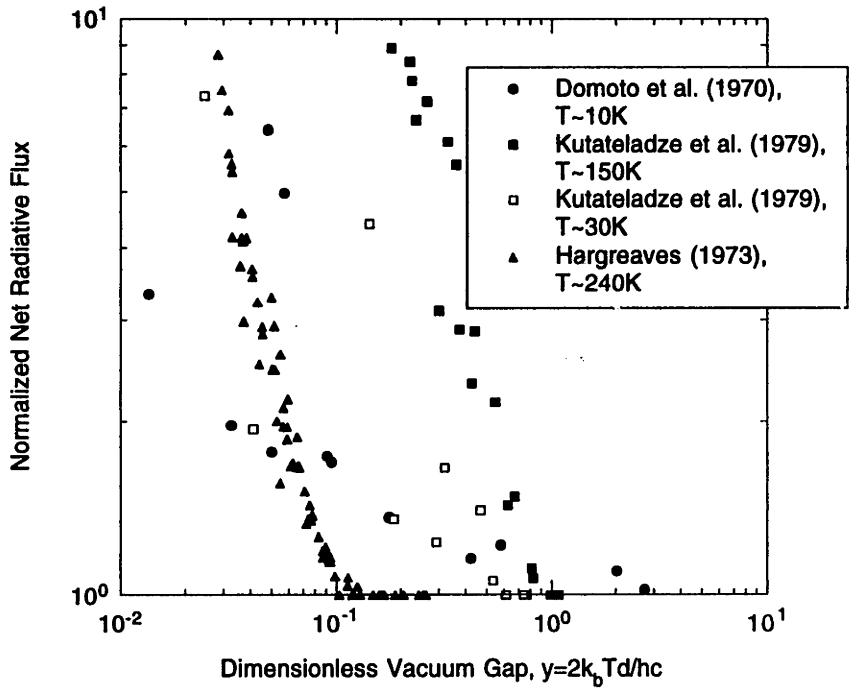

Figure 5: Measurements of the normalized net radiative flux versus dimensionless gap size.

Figure 5 shows all the experimental measurements versus the dimensionless gap. The measurements made by Hargreaves (1973) show very little spread, reducing to nearly a single line that shows the flux varies with the inverse fourth power of the gap. The high temperature measurements of Kutateladze et al. (1979) (those for a cold medium at 77 K) follow a similar trend, but display a spacing effect at a dimensionless gap approximately an order of magnitude higher. Such a shift is unexpected since the spacing effect should become evident when the Wien's wavelength is approximately the gap size; i.e. y=0.4. If not an experimental artifact, this shift must be due to a longer range effect of the near field. Similar to Hargreaves (1973) measurements, the data reported by Kutateladze et al. (1979) show no minimum at intermediate spacing, and at small spacing the dependence is to the inverse fourth power.

$$y = \frac{2d}{\lambda} = \frac{2k_b Td}{hc} \qquad \lambda = \frac{hc}{k_b T} \approx 5\lambda_W \tag{14}$$

where T is the mean temperature of the two media separated by a gap d. This approximation becomes invalid at low temperatures where the temperature difference is an appreciable fraction of the mean temperature, and therefore, a single dimensionless spacing cannot be defined.

As the temperature is decreased even further, more anomalies are evident. For the low-temperature measurements of Kutateladze et al. (1979), the spacing effect begins at the same magnitude of non-dimensional spacing as the higher temperature experiments. The spacing effect, however, is less dramatic and increases more slowly with decreasing gap. As the temperature difference increases (from ΔT~25 K to ΔT~42.1 K, the spacing resembles more closely the trend seen in the higher temperature experiments. The measurements of Domoto et al. (1970) were performed at still lower mean temperatures, and the results are similar to the colder experiments of Kutateladze et al. (1979): a low initial slope followed by an increase at intermediate gaps.

The theories and measurements also differ in the magnitude of the energy flux at large spacing. Figure 6 shows the ratio of the radiative transfer calculated from Levin's theory to that measured as a function of mean temperature. At low temperature the prediction under-estimates the radiative transfer. As the temperature is increased, the prediction over-estimates the radiative transfer by an order of magnitude. This comparison suggests that the experiments of Domoto et al. (1970) may not have reached steady state. If it was necessary to heat the system up to reach steady state, the measurements under-estimate the radiative transfer and the ratio would be greater than one.

This analysis indicates that there are substantial differences between the predictions and measurements. The data do not all collapse on a single line when plotted versus dimensionless spacing, as predicted by the theory. There is no clear evidence to support the small spacing trend. The uncertainty in the measurements is too high to reveal a clear

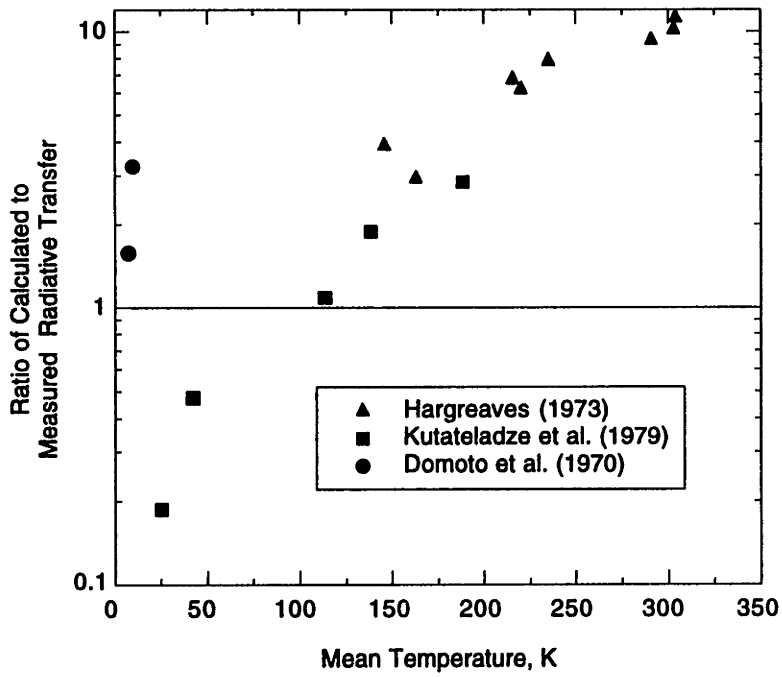

Figure 6: Comparison of the measured radiative transfer and the prediction of Levin et al. (1980) at large gap.

minimum. At very low temperatures, the measured trend at intermediate separations is not predicted by the theory. The theories do not predict the same magnitude of radiative transfer at large spacing. Although Levin et al. (1980) dismiss the results of Domoto et al. (1970) and Kutateladze et al. (1979) as erroneous due to their lack of agreement with their predictions, the substantial differences that exist with even Hargreaves (1973) results warrant a closer look at the possible root of the deviations.

Chapter 3

Approximate Predictions for Microscale Radiative Transfer

3.1 Introduction

In their most general form, the fluctuational electrodynamics approaches to accounts for the effects of wave interference and radiation tunneling yield formulations, which are in agreement. However, the practical application to particular materials has required various simplifications to render the results more tractable. These simplifications are not generally applicable and cannot be compared directly, because of an inconsistent set of assumptions used to reduce the expressions. This chapter explores the basis of the assumptions used to make these approximations, clarify their limitations, and offer a set of regimes delineating their applicability. Proximity functions (in the strongly-absorbing and weakly-absorbing limits) that incorporate all the transport-enhancing effects of the general formalism are derived. These functions show the details of the spacing effect across all frequency and spacing regimes. Furthermore, while in agreement with the previous work, they provide a simple and elegant means to account for the far- and near-field effects of thermal radiation.

In the past several decades, there have been numerous attempts to develop a general formalism that accounts for the aforementioned effects on the net radiative transfer. As outlined in the previous chapter, early attempts by Boehm and Tien (1970) and Caren (1972a; 1972b) suffer from an inadequate specification of the source of the thermal field (Fragstein, 1950). Subsequent treatments use an approach first suggested by Rytov

(1953) that uses the fluctuation-dissipation theorem to model the source of the radiation field. These fluctuational electrodynamic treatments and approximations to them form the subject of this chapter.

The nature of the results of these approximations has been sufficiently complex that a complete understanding of the spacing phenomenon that would lead to a meaningful exploitation of the spacing effect has proven elusive. Furthermore, attempts by Levin et al. (1980) and by Loomis and Maris (1994) to simplify the theory introduce limitations of applicability that have not been reported. In the course of this examination, a proximity function is derived, which provides a simple and convenient closed-form function to account for the effects of both wave interference (far field) and radiation tunneling (near field).

Unlike previous work, which only presents the results of a numerical integration leading to the net heat flux, the present formulation of a proximity function illustrates the frequency-dependence of the spacing effect. With the more detailed structure revealed, ambiguities within and differences between earlier approaches are clarified. This function is a useful tool for including the spacing effect for the purposes of analysis, presenting no more difficulty than a frequency-dependent emissivity. This approach facilitates the design and analysis of systems whose dimensions are on the order of or less than the wavelengths of the thermal radiation.

3.2 Comparison of Previous Approximations

In order to determine the net radiative transport between two infinite parallel plates, it is necessary to determine the material properties of the media and model their variation with temperature and frequency. There are two distinct limits that represent the behavior of materials with respect to radiative transport, namely the strongly-absorbing limit (metals) in which the propagation of the electromagnetic fields is highly attenuated or the

weakly-absorbing limit (dielectrics) in which the fields propagate with little attenuation. For these two models the formalism outlined in Chapter 2 simplifies considerably.

3.2.1 Strongly-Absorbing Limit (Metals)

The earliest attempts to use the fluctuational electrodynamics approach (Polder and Van Hove, 1971; Levin et al., 1980) simplified the formalism by assuming a purely imaginary permittivity of the form: $\varepsilon=-(4\pi\sigma/ck)i$ where the dc conductivity, σ, is so large that the magnitude of the permittivity is much greater than unity over all relevant frequencies.

Levin et al. (1980) made an impedance approximation for highly-conducting metals and simplified the equations to examine the first order effects in surface impedance only. This simplification eliminated the material properties of a particular medium by assuming that either the anomalous skin effect or normal skin effect theory was sufficient to characterize the surface impedance (and in so doing it was assumed that the electronic transport mechanisms in both media are identical). By dividing the expression for the radiative transfer as a function of spacing by the expression at large spacing, the material-dependent properties cancel out leaving an expression which depends only on the first order power between surface impedance and frequency.

Levin et al. (1980) assumed that for all relevant frequencies, the metal is strongly-absorbing, and so the wave vector in the material reduces to:

$$k_{z_j} = \sqrt{k^2 \varepsilon_j \mu_j - k_x^2} \approx k\sqrt{\varepsilon_j \mu_j} \tag{15}$$

This approximation is illustrated in Fig. 2(a), which shows that for a highly-conductive material, the wave vector in the surface closely follows the relative permittivity. Using this approximation, Levin et al. (1980) examined only singularities in the integrals for M in Eq. 12. As a result, the approximate equations are valid only for a very small gap between surfaces whose permittivity is very high and purely imaginary. Their subsequent

analysis does not make any mention of this limitation in spite of their apparent knowledge of the work of Polder and Van Hove (1971). By carefully accounting for the individual traveling waves that meet the boundary conditions as the gap gets larger, Levin et al. (1980) found for metals:

$$M = M_{\parallel} + M_{\perp} = k^2 \frac{\mathrm{Re}\left(\sqrt{\mu_1/\varepsilon_1}\right)\mathrm{Re}\left(\sqrt{\mu_2/\varepsilon_2}\right)}{\mathrm{Re}\left(\sqrt{\mu_1/\varepsilon_1}\right)+\mathrm{Re}\left(\sqrt{\mu_2/\varepsilon_2}\right)} f\left(\frac{kd}{\pi}\right)$$
$$f(y) = \frac{1}{2y} + \frac{m}{y} + \frac{m(m+1)(2m+1)}{6y^3}, \quad m = \mathrm{int}(y) \tag{16}$$

When the materials are the same, non-magnetic (μ=1), and the permittivity is purely imaginary, the function M will reduce to:

$$M = \frac{k^2}{2\sqrt{2}|\varepsilon|^{1/2}} f\left(\frac{kd}{\pi}\right), \text{ where } \quad |\varepsilon| = \frac{2\sigma}{ck} \tag{17}$$

where $k=2\pi\omega/c$. After examining the approach used by Polder and Van Hove (1971), a quantitative assessment of the limitation of the approach of Levin et al. (1980) is presented.

Polder and Van Hove (1971) present a much more convincing and justified approximation for the integrals in Eq. 12, although they examine only the near-field effect for systems in which both materials have the same relative permittivity and a permeability of μ=1. Without making the simplification in Eq. 15, they proceed by grouping the wave vector in the materials and the permittivity together, so that: $\rho_{\parallel} = \arg(k_z/\varepsilon), \rho_{\perp} = \arg(k_z)$. Depending on the size of the gap, the integrands take on a form that yields simple expressions for each regime when integrated analytically. For the parallel-polarized field:

$$M_{\parallel} \approx \frac{k\cos\rho_{\parallel}}{4|\varepsilon|^{1/2}d}\left(\pi/2 + \rho_{\parallel}\right) \quad d << \frac{1}{\left|k_z/\varepsilon\right|}$$
$$M_{\parallel} \approx \frac{7.212|\varepsilon|\cos^2\rho_{\parallel}}{4k^2d^4} \quad d >> \frac{1}{\left|k_z/\varepsilon\right|} \tag{18}$$

For the perpendicular-polarized field:

$$M_{\perp} \approx \frac{k^2|\varepsilon|\cos^2\rho_{\perp}}{8} \quad d << \frac{1}{|k_z|}$$
$$M_{\perp} \approx \frac{7.212\cos^2\rho_{\perp}}{4|\varepsilon|k^2d^4} \quad d >> \frac{1}{|k_z|} \tag{19}$$

Note that these results are completely consistent with the result of Levin et al. (1980) shown in Eq. 16, if one considers only a very small gap ($d<<1/|k_z/\varepsilon|$) with a purely imaginary permittivity. The difference of a factor of two arises from the far-field component which has a similar form at small gap sizes and thus adds to the near-field result. While Polder and Van Hove (1971) limit themselves to similar materials, their results cover a much broader range of spacing: specifically, any range where the near field dominates.

The regimes of validity of these approximations for highly-conductive materials are delineated by comparing the gap size to the dominant wavelength of the radiation. Wien's displacement law gives the wavelength of maximum emissive power for the Planck distribution. The near-field effects begin to appear when the gap is on the order of the wavelength of maximum emissive power. For a typical metal with a dc conductivity of about 10^{18} s^{-1} (cgs units), the gap sizes for which the various components become important can be estimated.

$$d_{near} \approx \lambda_W = \frac{2\pi}{k}, \quad \lambda_W T = 2898\mu\text{mK} \quad d_{near} \approx \frac{2898\mu\text{mK}}{T}$$
$$d_{\parallel} \approx \frac{1}{|k_z/\varepsilon|} = \frac{1}{|\sqrt{\varepsilon}k/\varepsilon|} = \sqrt{4\pi\sigma/ck^3} \qquad d_{\parallel} \approx \frac{45\mu\text{mK}^{3/2}}{T^{3/2}} \tag{20}$$
$$d_{\perp} \approx \frac{1}{|k_z|} = \frac{1}{|\sqrt{\varepsilon}k|} = \sqrt{c/4\pi\sigma k} \qquad d_{\perp} \approx \frac{0.1\mu\text{mK}^{1/2}}{T^{1/2}}$$

Figure 7 illustrates these regimes. The results of Levin et al. (1980) have a very limited range of applicability: only at very low temperatures is their result useful, and even then it is applicable only to gap sizes much less than 1 μm (hatched upward to the

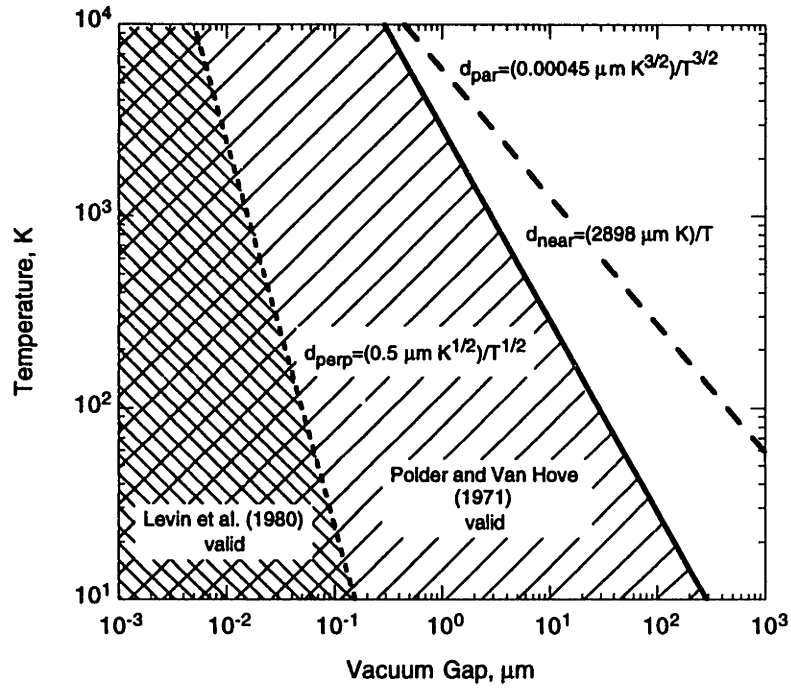

Figure 7: Temperature-gap regimes: the regions of validity for the approximations proposed by Levin et al. (1980) and Polder and Van Hove (1971).

left). The approximations made by Polder and Van Hove (1971) (hatched upward to the right), however, show a much wider range of applicability, extending up to the far-field regimes (solid line) and overlapping the more limited regime of Levin et al. (1980).

After several early attempts to formulate a theory for the enhanced heat transfer at small spacing (the results of which were not satisfactory), Caren (1974), with knowledge of the work of Polder and Van Hove (1971), offered a simplified result for the case of metals at low temperature. At such low temperatures, the extreme anomalous skin effect (EASE) predominates. Similar to the normal skin effect, a local relationship exists between the induced current and electromagnetic field for a material in the EASE region. The theory for the EASE is much more tractable than the anomalous skin effect, and as a result, Caren (1974) was able to use a simple expression for the surface impedance in his formulation. This simple formula permitted Caren (1974) to cast the spacing effect in powers of $y=2k_bTd/hc$, where T is the temperature of a particular material. This

formulation provides insight into the nature of the spacing effect. At small gaps sizes, the heat flux rises in a manner inversely proportional to the gap size, while at intermediate gaps, it rises more steeply: d^{-4}. Caren (1974) discusses only the unidirectional heat flux. For the net heat flux, the use of his expressions becomes problematic since at low temperatures where the EASE dominates, the dimensionless parameter y, defined by a single temperature, no longer accurately characterizes the temperature dependence of either material. Caren (1974) provides a comparison with several sets of data, demonstrating that the use of EASE theory may prove applicable to experiments made at particularly low temperatures.

3.2.2 Weakly-Absorbing Limit (Dielectrics)

Loomis and Maris (1994) were interested in the heat transfer associated with evanescent electromagnetic waves. While they based their approach on the early work of Polder, they were apparently unaware of any later work, including several experimental measurements of the spacing effect. Loomis and Maris present a theory which is in every way consistent with the theory outlined above. Owing to their interest in atomic force microscopy, however, they proceed to simplify the general formalism by assuming the wave vector in the material can be simplified so that it is equal to the wave vector in the vacuum. This assumption is equivalent to assuming that the materials are dielectrics in which the electrical conductivity is very weak, and the thermal radiation penetrates with little attenuation.

Figure 2(b) illustrates the wave vectors when the materials are not highly conductive. Due to the low conductivity, the wave vector, k_z can be approximated by k_{zv}. This assumption greatly reduces the complexity of the integral, so that a factor of d^{-2} comes out of the integral entirely.

Loomis and Maris (1994) give a condition for which their approximation is valid:

$$d << \frac{1}{2k\sqrt{|1-\varepsilon|}} = \frac{1}{2}\sqrt{\frac{c}{4\pi\sigma k}} = \frac{d_\perp}{2} \tag{21}$$

This condition is equivalent to the case of Levin et al. (1980). It cannot be expected, therefore, to use this approximation over a very wide range of gap sizes and will always be restricted to low-conductivity materials. This result for small spacing between dielectrics differs by a full power from the case of a metal. Note that as long as the conductivity is high enough, the previous results derived for metallic surfaces are correct, and the d^{-1} behavior is valid. The actual behavior is somewhere between the two extremes. Polder and Van Hove, themselves, found in their numerical integration, a substantial deviation from the d^{-2} dependence. Although they do not allude to a cause, performing the numerical integration over a frequency range where the conductivity is no longer large compared to one may account for this deviation. This effect occurs since the upper bound on the integral goes to infinity. As Loomis and Maris (1994) point out, a region where d^{-1} occurs will always be reached. Its effect, however, becomes important only at very small gap sizes – one for which any argument is purely academic given the available measurements.

3.3 Present Approach: Proximity Functions

A better understanding of the details of the spacing effect is obtained by determining the frequency-dependent nature of the spacing effect. To this end, in this section is derived a function which characterizes the wave-interference and radiation tunneling effects. This function is constructed in much the same manner as the previous investigations. Here, however, the form of this proximity function is examined in an attempt to deepen the understanding of the effect and the influence of temperature and frequency. This knowledge will prove useful in the design of devices to exploit the enhanced heat transfer, where the flux due to specific frequency intervals is important. Lastly, the product of this function and Planck's distribution is integrated to determine the

net radiative heat flux. This approach follows closely the procedure of Levin et al. (1980) for the far-field effect and Polder and Van Hove (1971) for the near-field effect.

3.3.1 Strongly-Absorbing Limit (Metals)

Consider a thermally interacting system as illustrated in Fig. 1, where both materials are identical highly-conducting metals, for which the permeability is unity (μ=1), and the permittivity has both real and imaginary components. For the near field, $k<k_x$, and therefore from Eq. 12, $k_{z_v} = \sqrt{k^2 - k_x^2} = -i\kappa$ so $\kappa = \sqrt{k_x^2 - k^2}$. Equation 12 reduces to:

$$
\begin{aligned}
M_{\parallel}^{near} &= \frac{1}{4}\int_0^{\infty} t_{\parallel}\, \kappa d\kappa \\
t_{\parallel} &= \frac{\cos^2\rho_{\parallel}}{\left(\frac{\sinh(\kappa d)}{2}\right)^2\left(\frac{|k_z/\varepsilon|}{\kappa}+\frac{\kappa}{|k_z/\varepsilon|}\right)^2 - \frac{\sinh(2\kappa d)}{2}\left(\frac{|k_z/\varepsilon|}{\kappa}+\frac{\kappa}{|k_z/\varepsilon|}\right)\sin\rho_{\parallel} + \sinh^2(\kappa d)\left(\frac{1}{2}+\sin^2\rho_{\parallel}\right)+1} \\
M_{\perp}^{near} &= \frac{1}{4}\int_0^{\infty} t_{\perp}\, \kappa d\kappa \\
t_{\perp} &= \frac{\cos^2\rho_{\perp}}{\left(\frac{\sinh(\kappa d)}{2}\right)^2\left(\frac{|k_z|}{\kappa}+\frac{\kappa}{|k_z|}\right)^2 - \frac{\sinh(2\kappa d)}{2}\left(\frac{|k_z|}{\kappa}+\frac{\kappa}{|k_z|}\right)\sin\rho_{\perp} + \sinh^2(\kappa d)\left(\frac{1}{2}+\sin^2\rho_{\perp}\right)+1}
\end{aligned}
\tag{22}
$$

By examining the regimes outlined by Polder and Van Hove (1971), Equation 22 simplifies without making any other assumptions except on the gap size. For $d<<1/|k_z/\varepsilon|$, over a wide range of κ, $\sinh(\kappa d)$ κd, and therefore:

$$
\begin{aligned}
t_{\parallel} &\approx \frac{\cos^2\rho_{\parallel}}{\frac{(\kappa d)^2}{4}\left(\frac{|k_z/\varepsilon|}{\kappa}+\frac{\kappa}{|k_z/\varepsilon|}\right)^2 - \kappa d\left(\frac{|k_z/\varepsilon|}{\kappa}+\frac{\kappa}{|k_z/\varepsilon|}\right)\sin\rho_{\parallel} + (\kappa d)^2\left(\frac{1}{2}+\sin^2\rho_{\parallel}\right)+1} \\
&= \frac{\cos^2\rho_{\parallel}}{\frac{1}{4}\left(|k_z/\varepsilon|d+\frac{\kappa^2 d}{|k_z/\varepsilon|}\right)^2 - \left(|k_z/\varepsilon|d+\frac{\kappa^2 d}{|k_z/\varepsilon|}\right)\sin\rho_{\parallel} + (\kappa d)^2\left(\frac{1}{2}+\sin^2\rho_{\parallel}\right)+1}
\end{aligned}
\tag{23}
$$

But $\left|\frac{k_z}{\varepsilon}\right|d << 1$, and so $(\kappa d)^2 << \kappa^2 d/\left|\frac{k_z}{\varepsilon}\right|$, therefore:

$$t_{\parallel} \approx \frac{\cos^2 \rho_{\parallel}}{\left(\frac{\kappa^2 d}{2|k_z/\varepsilon|}\right)^2 - \left(\frac{\kappa^2 d}{|k_z/\varepsilon|}\right)\sin \rho_{\parallel} + 1} = \frac{1}{\left[\frac{\kappa^2 d}{2|k_z/\varepsilon|\cos \rho_{\parallel}} - \tan \rho_{\parallel}\right]^2 + 1} \tag{24}$$

By recognizing that for a highly-conductive material, $|k_z/\varepsilon|$ is independent of κ (see Fig. 2(a)), and making the appropriate substitution, the near-field effect due to parallel-polarized waves reduces to:

$$M_{\parallel}^{near} \approx \frac{1}{4}\int_0^{\infty} \frac{\kappa d\kappa}{\left[\frac{\kappa^2 d}{2|k_z/\varepsilon|\cos \rho_{\parallel}} - \tan \rho_{\parallel}\right]^2 + 1} = \frac{1}{4}\int_{-\tan \rho_{\parallel}}^{\infty} \frac{|k_z/\varepsilon|\cos \rho_{\parallel}}{d} \frac{du}{u^2 + 1} = \frac{|k_z/\varepsilon|\cos \rho_{\parallel}}{4d}\left[\frac{\pi}{2} + \rho_{\parallel}\right] \tag{25}$$

Figure 7 shows that when the gap size is larger than $1/|k_z/\varepsilon|$, the far field dominates, and so one need not consider this component for the purposes of forming a proximity function. Note the equality of Eq. 25 and Eq. 18 (the result of Polder and Van Hove (1971)) when $k_z = \sqrt{\varepsilon}k$.

Now consider the perpendicularly-polarized contribution to the spacing effect. For $d<<1/|k_z|$, over a wide range of κ, κd is so small that $\sinh(\kappa d)$ 0 and the denominator in Eq. 22 becomes unity.

$$M_{\perp}^{near}\Big|_{d<<} \approx \frac{1}{4}\int_0^{\infty} \frac{\cos^2 \rho_{\perp}\, \kappa d\kappa}{(0)\left(\frac{|k_z|}{\kappa}\right)^2 - (0)\left(\frac{|k_z|}{\kappa}\right)\sin \rho_{\perp} + (0)\left(\frac{1}{2} + \sin^2 \rho_{\perp}\right) + 1} = \frac{1}{4}\int_0^{\kappa<<|k_z|} \cos^2 \rho_{\perp}\, \kappa d\kappa \approx \frac{\cos^2 \rho_{\perp}}{8}|k_z|^2 \tag{26}$$

For $d>>1/|k_z|$ the hyperbolic sine function dominates. By keeping the highest order terms and noting that for a permittivity of large magnitude, $\kappa<<|k_z|$, Eq. 22 becomes:

$$t_{\perp} \approx \frac{\cos^2\rho_{\perp}}{\frac{\sinh^2(\kappa d)}{4}\left(\frac{|k_z|}{\kappa}\right)^2 - \frac{\sinh(2\kappa d)}{2}\left(\frac{|k_z|}{\kappa}\right)\sin\rho_{\perp} + \sinh^2(\kappa d)\left(\frac{1}{2}+\sin^2\rho_{\parallel}\right)+1}$$
$$= \frac{\cos^2\rho_{\perp}}{\frac{\sinh^2(\kappa d)}{4}\left(\frac{|k_z|}{\kappa}\right)^2} = \left(\frac{2\cos\rho_{\perp}}{\sinh(\kappa d)|k_z|}\right)^2 \kappa^2 \tag{27}$$

So that the integral becomes:

$$M_{\perp}^{near}\Big|_{d>>} \approx \frac{1}{4}\int_0^{\infty}\left(\frac{2\cos\rho_{\perp}}{\sinh(\kappa d)|k_z|}\right)^2 \kappa^3 d\kappa = \frac{\cos^2\rho_{\perp}}{|k_z|^2 d^4}\int_0^{\infty}\frac{x^3 dx}{\sinh^2(x)} \approx \frac{1.803\cos^2\rho_{\perp}}{|k_z|^2 d^4} \tag{28}$$

Equations 25 through 28 provide the near-field approximations for two highly-conductive isotropic materials, which are consistent with the approach used by Polder and Van Hove (1971) (see Eq. 18 and Eq. 19, above). For the perpendicular polarization, it is necessary to combine Eq. 26 and Eq. 28 into a single function, which can be accomplished by adding the results together much like resistors in parallel.

$$M_{\perp}^{near} \approx \left[\frac{1}{M_{\perp}^{near}\Big|_{d<<}} + \frac{1}{M_{\perp}^{near}\Big|_{d>>}}\right]^{-1}$$
$$= \left[\frac{8}{|k_z|^2\cos^2\rho_{\perp}} + \frac{|k_z|^2 d^4}{1.803\cos^2\rho_{\perp}}\right]^{-1} = \frac{|k_z|^2\cos^2\rho_{\perp}}{8+0.5546(|k_z|d)^4} \tag{29}$$

This procedure provides a single function which covers smoothly the entire range of gap sizes below, through, and beyond the cut-off gap size where $d=1/|k_z|$,.

Now, consider the behavior of integrals in Eq. 12 when the far-field effects are dominant. For the far field, $0<k_x<k$ and therefore, the correct form of the integrals is obtained by making the substitution $i\kappa$ for κ, where $\sinh(i\kappa d)$ becomes $i\sin(\kappa d)$, Eq. 22 becomes:

$$M_{\parallel}^{far} = \frac{1}{4}\int_0^k t_{\parallel}\,\kappa d\kappa$$

$$t_{\parallel} = \frac{\cos^2\rho_{\parallel}}{\left(\frac{\sin(\kappa d)}{2}\right)^2\left(\frac{|k_z/\varepsilon|}{\kappa}-\frac{\kappa}{|k_z/\varepsilon|}\right)^2 - \frac{\sin(2\kappa d)}{2}\left(\frac{|k_z/\varepsilon|}{\kappa}-\frac{\kappa}{|k_z/\varepsilon|}\right)\sin\rho_{\parallel} + \sin^2(\kappa d)\left(\frac{1}{2}+\sin^2\rho_{\parallel}\right)+1} \tag{30a}$$

And for the perpendicular polarization:

$$M_{\perp}^{far} = \frac{1}{4}\int_0^k t_{\perp}\,\kappa d\kappa$$

$$t_{\perp} = \frac{\cos^2\rho_{\perp}}{\left(\frac{\sin(\kappa d)}{2}\right)^2\left(\frac{|k_z|}{\kappa}-\frac{\kappa}{|k_z|}\right)^2 - \frac{\sin(2\kappa d)}{2}\left(\frac{|k_z|}{\kappa}-\frac{\kappa}{|k_z|}\right)\sin\rho_{\perp} + \sin^2(\kappa d)\left(\frac{1}{2}+\sin^2\rho_{\perp}\right)+1} \tag{30b}$$

For very small κ, the perpendicular component contributes nothing to the heat transfer since there are no singularities in $M_{\perp}^{far}$, however, the parallel-polarized wave contributes to the heat flux. This contribution takes on the same form as shown in Eq. 24, except that the sign in front of the tangent is positive. As a result, the far-field contribution at small κ is:

$$\begin{aligned} M_{\parallel}^{far}\Big|_{\kappa\to 0} &\approx \frac{1}{4}\int_0^{} \frac{\kappa d\kappa}{\left[\frac{\kappa^2 d}{2|k_z/\varepsilon|\cos\rho_{\parallel}}+\tan\rho_{\parallel}\right]^2+1} \\ &= \frac{1}{4}\int_{\tan\rho_{\parallel}} \frac{|k_z/\varepsilon|\cos\rho_{\parallel}}{d}\frac{du}{u^2+1} \\ &= \frac{|k_z/\varepsilon|\cos\rho_{\parallel}}{4d}\left[\frac{\pi}{2}-\rho_{\parallel}\right] \end{aligned} \tag{31}$$

Because of the presence of sine functions in the denominator of Eq. 30, there will be singularities at all the zeros of $\sin(\kappa d)$. For $\kappa_n = n\pi/d < k$ (n being an integer), Levin et al. (1980) simplified their expression equivalent to Eq. 30, by using $\sin(\kappa d)\,(-1)^n\,\kappa' d$ where $\kappa = \kappa_n + \kappa'$. By using this approximation in Eq. 30, the contribution for each singularity is independent of n and equal to:

$$\frac{|k_z/\varepsilon|\cos\rho_{\|}}{2}\frac{\pi}{d} \tag{32}$$

The number of these contributions is the integer part of kd/π (m=int(kd/π)), so that the summary contribution of each of the peaks and that for which κ is small (Eq. 31) combine to give:

$$\begin{aligned} M_{\|}^{far} &\approx \frac{|k_z/\varepsilon|\cos\rho_{\|}}{2}\frac{3m\pi}{4d} + M_{\|}^{far}\Big|_{\kappa\to 0} \\ &= \frac{|k_z/\varepsilon|\cos\rho_{\|}}{4}\frac{3m\pi}{2d} + \frac{|k_z/\varepsilon|\cos\rho_{\|}}{4d}\left[\frac{\pi}{2}-\rho_{\|}\right] \\ &= \frac{|k_z/\varepsilon|\cos\rho_{\|}}{4d}\left[\frac{\pi}{2}(3m+1)-\rho_{\|}\right] \end{aligned} \tag{33}$$

This result is consistent with Levin et al. (1980) where they assume that $k_z = \sqrt{\varepsilon}k$ and $\rho_{\|} = \pi/4$. This substitution indicates that Eq. 33 has an additional factor of 3/4 preceding the expressions given by Levin et al. (1980). This factor assures that as the gap size grow to infinity, the gap-dependent portion of the proximity function will approach unity. Because the approximations made to these integrals are accurate to first order, this factor ensures a physically sound result in the limit, without sacrificing either the applicability or the accuracy of the function at smaller gap sizes.

For the perpendicularly-polarized waves, a similar simplification about each singularity provides the contribution about each point. The total contribution for all the singularities can be summed to yield:

$$M_{\perp}^{far} \approx \frac{3}{4}\frac{\pi^3\cos\rho_{\perp}}{2|k_z|d^3}\sum_{1}^{m} n^2 = \frac{\pi^3\cos\rho_{\perp}}{16|k_z|d^3}m(m+1)(2m+1) \tag{34}$$

Combining the results of these approximations provides the proximity function. Using Eq. 25, Eq. 29, Eq. 33, and Eq. 34, a closed-form function is obtained, which accounts for the effect of the gap on the net heat flux.

$$
\begin{aligned}
M &= M_{\|}^{near} + M_{\|}^{far} + M_{\perp}^{far} + M_{\perp}^{near} \\
&= \frac{|k_z/\varepsilon|\cos\rho_{\|}}{4d}\left[\frac{\pi}{2}+\rho_{\|}\right] + \frac{|k_z/\varepsilon|\cos\rho_{\|}}{4d}\left[\frac{\pi}{2}(3m+1)-\rho_{\|}\right] \\
&\qquad + \frac{\pi^3\cos\rho_{\perp}}{16|k_z|d^3}m(m+1)(2m+1) + \frac{|k_z|^2\cos^2\rho_{\perp}}{8+0.5546(|k_z|d)^4} \\
&= \frac{1}{2}\left[\pi|k_z/\varepsilon|\cos\rho_{\|}\left(\frac{1}{2d}+\frac{3m}{4d}\right) + \frac{\pi^3\cos\rho_{\perp}}{|k_z|}\frac{m(m+1)(2m+1)}{8d^3} + \frac{2|k_z|^2\cos^2\rho_{\perp}}{8+0.5546(|k_z|d)^4}\right]
\end{aligned}
\tag{35}
$$

A comparison of this result to that of Levin et al. (1980) is obtained by assuming that $k_z \approx \sqrt{\varepsilon}k$ and therefore $\cos\rho_{\perp} = \cos\rho_{\|} = \cos\rho$. Using $y=kd/\pi$, it is seen that the first three terms of this proximity function give the same result of Levin et al. (1980).

$$
M = \frac{k^2\cos\rho}{2|\varepsilon|^{1/2}}\left[\frac{1}{2y}+\frac{3m}{4y}+\frac{m(m+1)(2m+1)}{8y^3}+\frac{2\cos\rho|\varepsilon|^{3/2}}{8+0.5546|\varepsilon|^2\pi^4y^4}\right] \tag{36}
$$

At very small gap sizes, the proximity function is dominated by an inverse linear relationship with y. As y increases past unity, the two middle terms dominate the proximity function, and the far field becomes important. Between small and large gaps, is a region where the proximity function remains constant with the gap size, then steeply drops (by y^{-4}) before the far field dominates. This middle region was completely neglected by Levin et al. (1980), without explanation.

Because the permittivity varies with wave number (frequency), the proximity function cannot be formed into a function of one variable (e.g. $y=kd/\pi$). However, the form of the function can be examined by plotting it in three dimensions. For simplicity, consider the proximity function for a metal. Since the magnitude of the permittivity is much greater than unity for a metal, assume that $k_z \approx \sqrt{\varepsilon}k$ where $|\varepsilon| = 4\pi\sigma/ck$ and $\cos\rho=\cos\pi/4=1/\sqrt{2}$. The temperature dependence of the dc electrical conductivity is obtained from the Bloch-Grüneisen formula (Wilson, 1953), and the electrical resistivity is calculated using Matthiessen's rule (MacDonald, 1956). The proximity function for

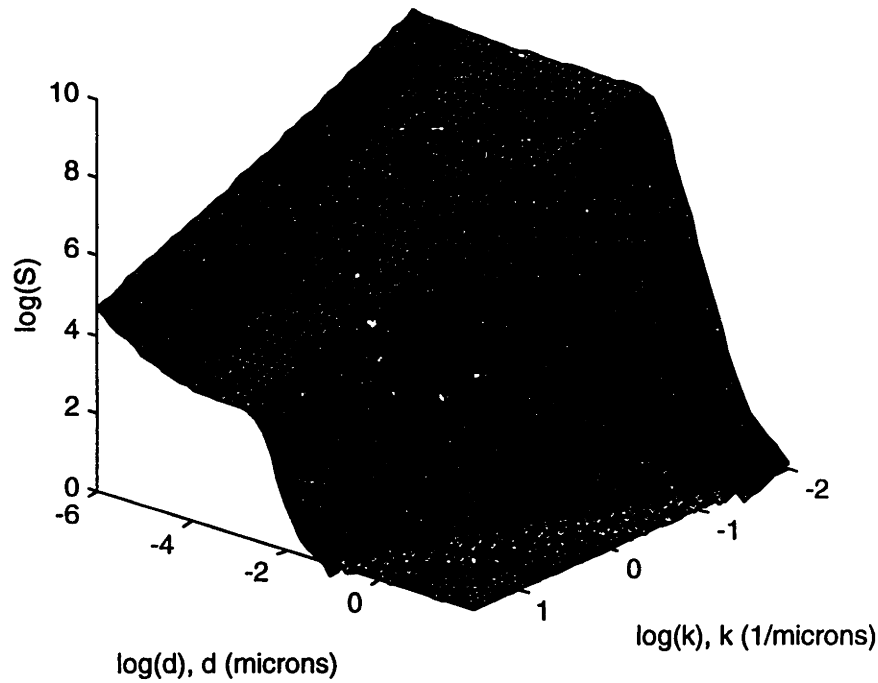

Figure 8: Gap-dependent part of the proximity function for a metal using material properties of gold at 300 K.

gold at a temperature of 300 K is shown in Fig. 8, where only the gap-dependent portion of the proximity function, S, such that $M = (k^2/2\sqrt{2}|\varepsilon|^{1/2})S$ is shown.

The proximity function augments the manner in which energy is distributed with frequency. Caren (1974) gave to the integral of the product of the proximity function and the mean energy of a quantum oscillator over all frequencies the term unidirectional heat flux; it can be considered as a modified Planck distribution due to the effect of spacing. For a metallic surface, the product of Eq. 8 and Eq. 36 yields:

$$P_{12}(k) = \frac{1}{\pi^2}\Theta(k,T)M(k,d)$$
$$= \frac{hc}{4\pi^3\sqrt{2}|\varepsilon|^{1/2}} \frac{k^3}{\exp(hkc/2\pi k_b T_1) - 1}\left[\frac{1}{2y} + \frac{3m}{4y} + \frac{m(m+1)(2m+1)}{8y^3} + \frac{\sqrt{2}|\varepsilon|^{3/2}}{8+0.5546|\varepsilon|^2\pi^4 y^4}\right] \quad (37)$$

The effect of the near field and wave-interference on Planck's distribution can be clearly seen in Fig. 9, where the unidirectional energy distribution is plotted for a gold

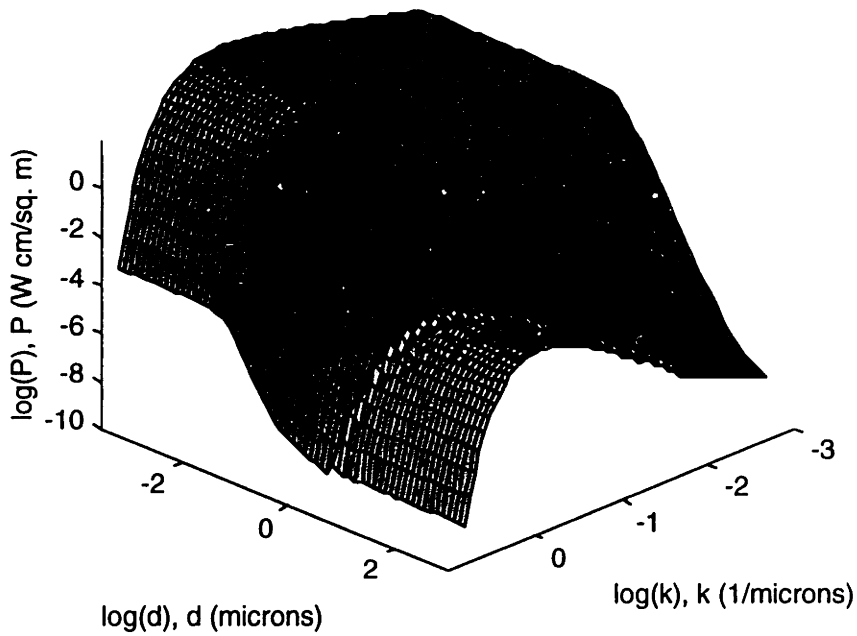

Figure 9: The integrand of the unidirectional heat flux, $P_{12}(k)$, for a metal using material properties of gold at 300 K.

surface at 300 K. At large gaps, our analysis gives the classical Planck's distribution and illustrates dramatically the transition through wave-interference to the near field.

3.3.2 Weakly-Absorbing Limit (Dielectrics)

To examine the details of the spacing effect on a material with low permittivity, consider the wave vector as illustrated in Fig. 2(b). For dielectric materials, an electromagnetic wave propagates with little attenuation (the imaginary part of the permittivity is low compared to unity). As a result, the wave vector in the material, k_z, is nearly equal to that in the vacuum, k_{zv}. Substituting $k_z \approx k_{z_v} = i\kappa$ in Eq. 22, provides an approximation to the integral for the case of a dielectric. Because the conductivity is low, the relative permittivity is almost purely real and near unity. The following substitutions into Eq. 22, $\cos\rho_{\parallel} = \cos\rho_{\perp} = 1$, $\sin\rho_{\parallel} = \sin\rho_{\perp} = 0$, and $|k_z| = \kappa$ result in the following simplifications:

$$M_{\|}^{near} = \frac{1}{4}\int_0^{\infty} \frac{\kappa d\kappa}{\frac{1}{4}(|\varepsilon|^2+2)\sinh^2(\kappa d)+1} = \frac{1}{4d^2}\int_0^{\infty} \frac{udu}{\frac{3}{4}\sinh^2(u)+1} = \frac{0.8151}{4d^2}$$

$$M_{\perp}^{near} \approx \frac{1}{4}\int_0^{\infty} \frac{\kappa d\kappa}{\frac{3}{2}\sinh^2(\kappa d)+1} = \frac{1}{4d^2}\int_0^{\infty} \frac{udu}{\frac{3}{2}\sinh^2(u)+1} = \frac{0.5461}{4d^2} \tag{38}$$

where $|\varepsilon|=1$ is used. By combining the two contributions, the near-field contribution to the proximity function is:

$$M^{near} = M_{\|}^{near} + M_{\perp}^{near} = \frac{0.8151}{4d^2} + \frac{0.5461}{4d^2} = \frac{1.3612}{4d^2} \tag{39}$$

For the far-field effects, a similar expression is obtained by making the same substitutions into Eq. 30. The periodic function in $\sin(\kappa d)$ can be approximated by the previously-introduced substitutions about the peaks:

$$M_{\|}^{far} = M_{\perp}^{far} \approx \frac{1}{4}\int_0^{k} \frac{\kappa d\kappa}{\frac{1}{2}\sin^2(\kappa d)+1}$$

$$M_{\|}^{far}\Big|_n \approx M_{\perp}^{far}\Big|_n \approx \frac{1}{2}\int_{-\infty}^{\infty} \frac{\kappa_n d\kappa'}{((-1)^n \kappa' d)^2+2} = \frac{\kappa_n}{2d}\int_{-\infty}^{\infty} \frac{du}{u^2+2} = \frac{n\pi}{2d^2}\left[\frac{1}{\sqrt{2}}\tan^{-1}\left(\frac{u}{\sqrt{2}}\right)\right]_{-\infty}^{\infty} = \frac{n\pi^2}{2\sqrt{2}d^2} \tag{40}$$

$$\text{so} \quad M^{far} = M_{\|}^{far} + M_{\perp}^{far} = 2\sum_1^m \frac{n\pi^2}{2\sqrt{2}d^2} = \frac{m(m+1)\pi^2}{2\sqrt{2}d^2}$$

Combining Eq. 39 and Eq. 40 yields the proximity function for a dielectric material.

$$M = M^{near} + M^{far} = \frac{1.3612}{4d^2} + \frac{m(m+1)\pi^2}{2\sqrt{2}d^2}\sqrt{2} = \frac{k^2}{2}\left[\frac{0.6806}{\pi^2 y^2} + \frac{m(m+1)}{y^2}\right] \tag{41}$$

As for the case of a metal, a factor has been incorporated (here $\sqrt{2}$) so that the gap-dependent portion of the proximity function will approach unity at large gap size.

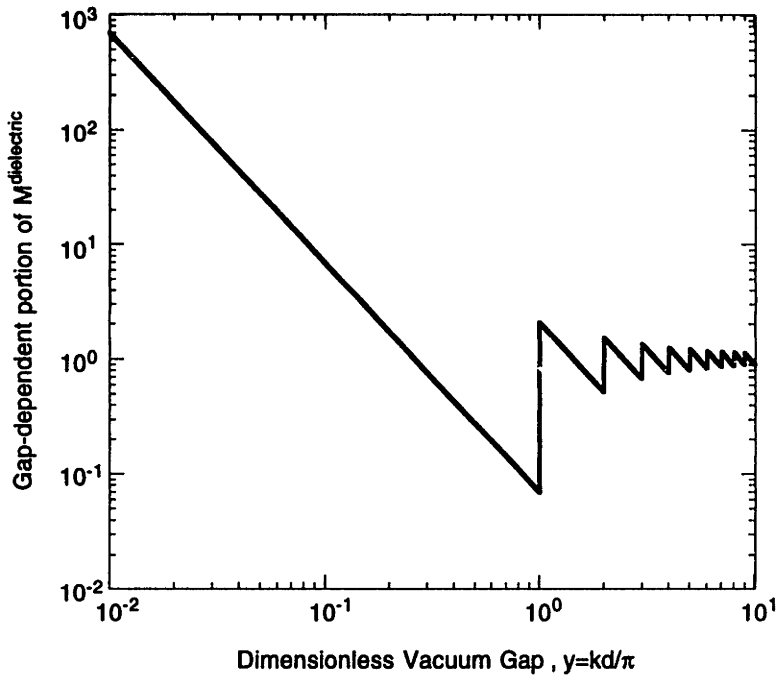

Figure 10: The gap-dependent portion of the proximity function for a system of two dielectric surfaces.

Because the approximations made to these integrals are accurate to first order, this factor ensures a physically sound result in the limit, without sacrificing the applicability or the accuracy of the function at smaller gap sizes.

The gap-dependent portion of the proximity function for a dielectric is shown in Fig. 10. The form of our proximity function permits the examination of the spacing effect on dielectric materials as a function of one variable, analogous to the form of Levin et al. (1980) for a metal. In agreement with the observations of Loomis and Maris (1994), the near-field effect to be inversely proportional to the second power of the gap size *d*. However, because the magnitude of the permittivity was assumed low (approaching unity), the proximity function is independent of the material properties, and the dependence on dc conductivity that Loomis and Maris (1994) show in their regime maps cannot be verified. This difference will be apparent when the regime maps based on this proximity function are presented.

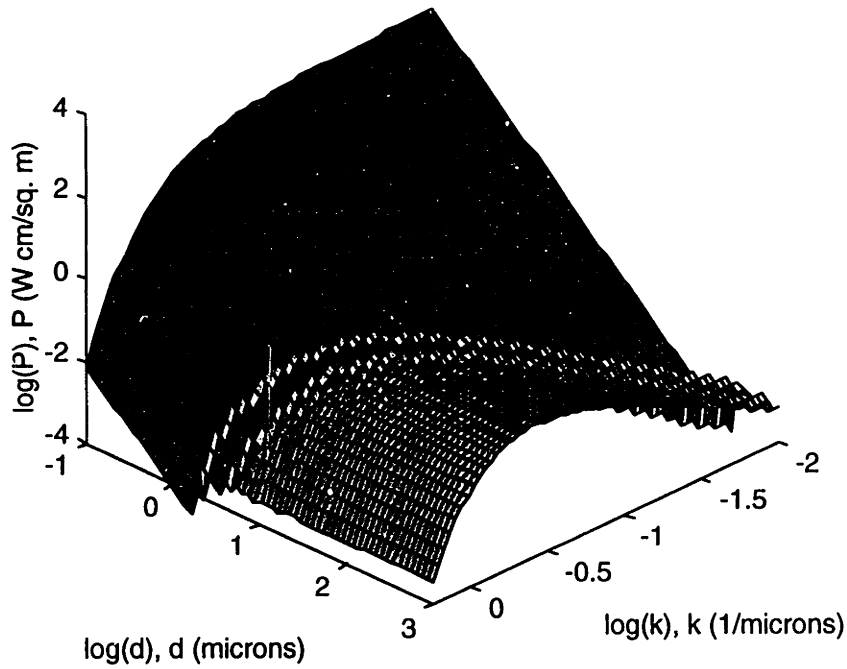

Figure 11: The integrand of the unidirectional heat flux, $P_{12}(k)$, for a dielectric at 300 K.

Figure 11 shows the product of the proximity function for a dielectric and the mean energy of a quantum oscillator at 300 K (Eq. 42).

$$P_{12}(k) = \frac{\Theta(k,T)M(k,d)}{\pi^2} = \frac{hc}{4\pi^3}\frac{k^3}{\exp(hkc/2\pi k_b T_1)-1}\left[\frac{0.6806}{\pi^2 y^2} + \frac{m(m+1)}{y^2}\right] \qquad (42)$$

This product is the integrand of the unidirectional heat flux for a dielectric. Similar to the case of a metal, Figure 11 illustrates the dramatic effect of the near field and the transition through the wave-interference to the classical result of Planck. The absence of strong absorption has decreased the magnitude of the spacing effect at intermediate gap sizes, but increased the spacing effect at small gaps. Note that the effect of the first peak, as the far field becomes important, is much greater for a dielectric than for a metal (compare with Fig. 10). It is expected that the magnitude of the permittivity will affect the net heat flux in this intermediate gap size.

3.3.3 Net Heat Flux Calculation and Permittivity-Gap Regimes

The expressions for the unidirectional heat flux from one surface (Eq. 37 for a metal; Eq. 42 for a dielectric) enable one to calculate the net heat flux between two surfaces at different temperatures. From Eq. 10, the net flux is found simply by reversing the indices, adding the result and integrating over all frequencies.

$$\begin{aligned} P &= \int_0^\infty P(\omega)d\omega = \int_0^\infty P_{12}(\omega) + P_{21}(\omega)d\omega \\ &= \frac{1}{\pi^2}\int_0^\infty \Theta_1(T_1,\omega)M_{12} + \Theta_2(T_2,\omega)M_{21}d\omega \end{aligned} \tag{43}$$

but M_{ij}=-M_{ji} from Eq. 9, therefore:

$$P = \frac{c}{\pi^2}\int_0^\infty \Theta_1(T_1,k)M(T_1,k,d) - \Theta_2(T_2,k)M(T_2,k,d)dk$$

Figure 12 shows the net radiative transfer as a function of the gap size for surfaces at 320 K and 300 K. The results are normalized using the net flux at large spacing, in order to compare the influence of weakly-absorbing materials (dielectrics) and strongly-absorbing materials on the spacing effect. (Metallic surfaces have a high reflectance, and therefore, the net flux is lower than that for dielectrics, as indicated by the presence of the magnitude of the permittivity in the denominator of Eq. 36.) For a metal, the intermediate regime, characterized by a steep increase (d^{-4}) followed by a region independent of gap size, is clearly apparent. The magnitude of this constant region is dependent on the magnitude of the permittivity (last term of Eq. 36). Strongly-absorbing materials exhibit a very steep increase to a large heat flux at intermediate gap sizes, while a decrease in the permittivity lessens the effect.

Also shown in Fig. 12 is the result of a numerical calculation made on the full expressions (Eq. 22 and Eq. 30) for gold surfaces. There is very good agreement between the proximity function over a wide range of gap sizes. This approximation does not

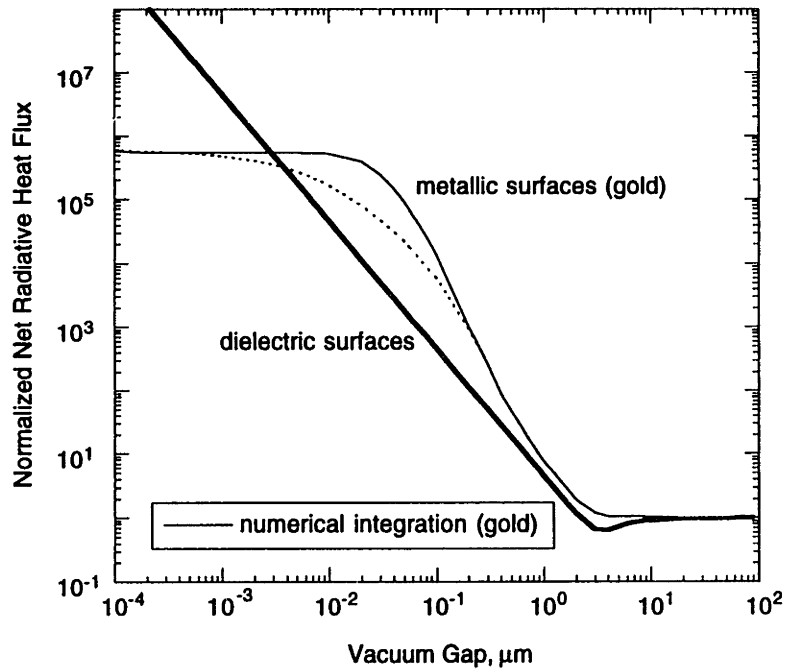

Figure 12: The normalized net radiative flux versus gap size between surfaces at 320 K and 300 K.

capture the decrease in the rise of net flux just before the constant region is reached, however, it does capture the magnitude of the constant region and the onset of the spacing effect very well. Polder and Van Hove (1971) found a very similar result when comparing their numerical and approximate predictions.

While the intermediate region is not present in the result for a dielectric, there is a minimum prior to the increase at small spacing. This minimum, not apparent for the metallic system, is a result of the substantial decrease in the proximity function due to the cut-off of the last traveling wave of the far-field at gap sizes on the order of the wavelength of maximum power in Planck's distribution. As shown by Fig. 11, the proximity function for a dielectric enhances the contribution of longer wavelengths more slowly than the proximity function of a metal (Fig. 8) where the k^4 dependence increases the contribution of lower frequencies to the net heat flux. As a result of this greater

compensation, the net heat flux for a metal does not pass through a minimum prior to increasing at small gaps.

This minimum was observed in the predictions of Boehm and Tien (1970), the approximations of Polder and Van Hove (1971) (but not in their numerical calculations), the predictions made by Cravalho et al. (1967) for a dielectric, and by Levin et al. (1980) where they neglected the intermediate regime. None of the experimental measurements of verify this feature. This is not surprising, since none of these measurement were performed on weakly-absorbing materials. The actual existence of the minimum has been the subject of some disagreement in the literature, and its cause had remained undetermined. Formulating a set of regimes that delineate the dependence of the net flux on the gap size and magnitude of the permittivity provides more insight into this phenomenon and summarizes the effect of spacing on the net radiative transfer.

The regimes are formed by comparing the relative size of the gap-dependent terms in the proximity functions of Eq. 36 and Eq. 41. For instance, the far-field terms (those with m in the numerator) dominate the proximity function when their sum (approximately unity at large spacing) is greater than $1/(2y)$, that is when $y > 1/2$. Similar boundaries are determined by comparing all the terms; the resultant regimes are shown in Fig. 13. Above the dotted line are the regimes for strongly-absorbing materials (i.e. the magnitude of the permittivity is much greater than unity). Below the dotted line are the regimes for weakly-absorbing materials. Within each regime at high permittivity, the functional dependency of the proximity function on the magnitude of the permittivity and the gap size is indicated. Because the proximity function for a dielectric is formed by assuming that the magnitude of the permittivity is unity, the regimes are independent of the permittivity, as is the boundary between the regimes.

For the metal shown in Fig. 12, the permittivity is large, and by traversing the permittivity-gap regime map across $|\varepsilon|=10^4$, the system can be traced through the various

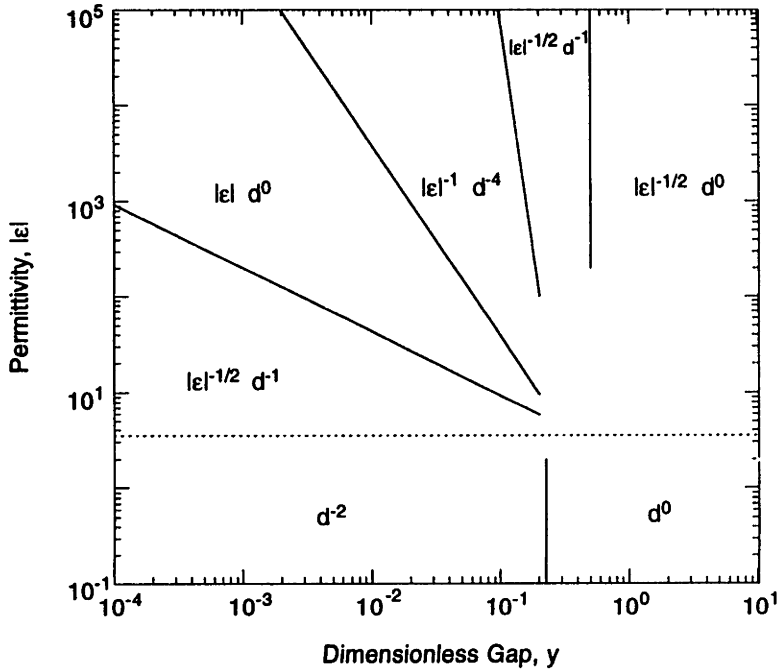

Figure 13: The permittivity-gap size regimes for the theory of microscale radiative transfer based on the proximity function.

regimes. For the dielectric, follow $|\varepsilon|=1$. These regimes are very similar to those determined by Loomis and Maris (1994), except for the absence of material dependency for materials of low permittivity and an intermediate regime at large permittivity between d^{-4} and the far field. The narrow size of this regime is responsible for the absence of a minimum in the net flux for two metallic surfaces. For a dielectric, the regime for small gaps, where the there is a relatively smaller spacing-effect at low frequency, covers a broad range of frequency, reducing the proximity function and creating the intermediate minimum in the net heat flux.

3.4 Conclusions

In this chapter, the theory behind the fluctuational electrodynamics approach to account for the near- and far-field effects on radiative transfer has been presented and the previous attempts to apply the theory to specific systems have been reviewed. By examining these attempts to approximate the theory, the limitations to the general

application of the approximations, which obscure the details of the spacing effect and render the use of the theory tenuous have been elucidated. The details of the spacing effect have been clarified by deriving a relatively simple proximity function that accounts for both the far- and near-field for two extremes: a metal (large permittivity) and a dielectric (low permittivity).

These proximity functions are in complete agreement, in these limits, with the earlier treatments in the literature and are valid across transitions between regimes in the limits of high or low permittivity. A set of regimes, which delineates the validity of the proximity functions, has been derived for the permittivity-gap plane. This map is a useful tool to predict the effect of spacing on the net radiative flux.

Loomis and Maris (1994), apparently unaware of existing measurements of the spacing effect, propose to perform experiments at room temperature using highly-doped semiconductors. In order to examine the spacing effect with such materials, it will be necessary to develop approximations which are valid across transitions from low to high permittivity. To exploit the spacing effect for other applications, it may be necessary to tailor the permittivity of the materials making up the surfaces. For instance, reducing or enhancing the radiative flux over a desired band of frequencies can be obtained by careful manipulation of the gap size, dc conductivity and temperature of the surfaces. In this manner, material specifications for a particular application can be determined, providing useful design criteria for material development . In order carry out such investigations, however, it is necessary to determine simple proximity functions which can be applied over the entire range of permittivity. In this manner, direct numerical integration will not be needed, allowing easier development of devices, without obscuring the physical mechanisms of importance.

Chapter 4

Regimes of Microscale Radiative Transfer Between Metallic Surfaces

4.1 Introduction

The preceding chapters illustrate the ample theoretical and experimental evidence to substantiate the enhanced transfer of energy by thermal radiation between two closely-spaced surfaces when the distance of separation is on the order of the characteristic wavelength of the radiation. These chapters have established that there is no clear agreement as to the magnitude of the effect of spacing on the thermal transport. In this chapter, the theoretical predictions and experimental measurements are consolidated for the first time. A set of microscale radiative transfer regimes that account for the different mechanisms of absorption that occur are derived. For the various experimental configurations, these regimes show that the disagreement among the experimental measurements performed thus far can be traced to the different microscale regimes that govern the absorption process. Furthermore, using these regimes the discrepancies between the analytical models and the experimental measurements are explained. At the very low cryogenic temperatures of some of the experimental configurations, the existing theories have limited applicability since the Boltzmann transport equation is not strictly valid at these temperatures.

4.2 Microscale Radiative Transfer Regimes

Although some of the measurements have been compared with the predictions in the literature (Hargreaves, 1973), careful attention was not paid to determine if the theory

meets the conditions under which the experiments were made. Comparisons should be made only between the predictions and measurements which meet the same restrictions. This chapter considers the hypothesis that the discrepancies between theory and experiment lie in the nature of the interaction between the incident photons and the electrons resident in the surface of the receiving body. Since the energy absorbed by the electrons must be given up ultimately to either the lattice or the surrounding electrons by collisions, the electronic transport phenomena in the bodies must be examined.

Such an examination begins by formulating a set of radiative transfer regimes for two thermally radiating bodies. The regimes are based on the relative sizes of the characteristic length scales which are important in the interaction of light and matter. Recently, Tien and Chen (1992) have discussed the importance of length scale on radiative transfer by delineating a number of microscale regimes for the interaction of electromagnetic radiation of a particular wavelength with a solid whose dimension in the direction of propagation is relatively small. The three microscale regimes identified indicate when wave-interference effects, classical size-effects, and quantum-size effects become important. A similar approach is presented here for the case of two bodies interacting by means of thermal radiation. This formulation uses the spacing between the surfaces as the characteristic size of the system rather than the size of the material layer; i.e. consider the two bodies to be semi-infinite. As a result, wave interference and radiation tunneling become important when the separation of the bodies is of the order of the Wien's wavelength.

Unlike the case considered by Tien and Chen (1992), regimes for a system of two radiatively interacting bodies are derived. The nature of the absorption process in one surface is coupled to the other surface, since, while each body absorbs energy, it is also a thermal source for the other body. Energy is emitted over a spectrum of wavelengths; hence, there is not a single characteristic wavelength that describes the incident radiation

completely. Wien's wavelength is used as a characteristic wavelength to represent this spectrum. The length scales, some of which depend on the frequency of the incident radiation, are coupled through the wavelength of maximum emissive power. Because the source radiation is not monochromatic, each body may in fact be in several different electronic transport regions at any one instant of time depending on its temperature and the frequency of the incoming radiation (Wooten, 1972).

The expressions for the important characteristic lengths are given below. Wien's wavelength is found by determining the maximum in the expression for Planck's distribution.

$$\lambda_W T = 2897.8\,\mu\text{m K} \approx \frac{hc}{4.83k_b} \tag{44}$$

The mean free path of the energy carrier is the product of the Fermi velocity and the scattering time, which in turn is a function of the electrical conductivity.

$$\Lambda = \tau v_F \tag{45}$$

When the electron mean free path is small relative to the penetration depth of the incident electromagnetic field, the electron experiences a constant electric field between collisions. This is known as the normal skin effect for which Ampere's Law gives the dispersion relation for an electromagnetic wave. From this result, an expression for the wave vector can be derived. The penetration depth is then the inverse of the imaginary part of this wave vector.

$$\delta_{NSE} = \left(2/\omega\mu_0\sigma\right)^{1/2} = \left(2897.8\times10^{-6}\,\text{mK}/\pi c\mu_0\sigma T\right)^{1/2} \tag{46}$$

where σ is the dc electrical conductivity. When the mean free path is large relative to the penetration depth of an electromagnetic wave, the electron experiences a spatially varying electric field between collisions, and Ohm's law is no longer valid. Then, the equation for

the penetration depth must be modified by replacing the electrical conductivity with an effective one.

$$\sigma_{\text{eff}} = \frac{\delta_{\text{NSE}}}{\Lambda}\sigma \tag{47}$$

$$\begin{aligned}\delta_{\text{ASE}} &= \left(2/\omega\mu_0\sigma_{\text{eff}}\right)^{1/2} = \left(\frac{2}{\omega\mu_0}\frac{m\upsilon_{\text{F}}}{Ne^2}\right)^{1/3} \\ &= \left(\frac{2897.8\times10^{-6}\,\text{mK}}{\pi c\mu_0 T}\frac{m\upsilon_{\text{F}}}{Ne^2}\right)^{1/3}\end{aligned} \tag{48}$$

The thermal deBroglie wavelength of an electron is calculated by assuming that the electrons constitute an electron gas in collisional thermal equilibrium with a velocity distribution given by the Boltzmann distribution and a mean momentum characterized by a temperature T.

$$\lambda_{\text{th}} = h/\sqrt{2\pi m k_{\text{b}} T} \tag{49}$$

Also included is another characteristic length, the distance traveled by an electron in a time $1/2\pi$ of the period of the radiation, in addition to the length scales used by Tien and Chen (1992). It is referred to here as the tidal displacement.

$$d_{\text{t}} = \frac{\upsilon_{\text{F}}}{\omega} = \frac{\upsilon_{\text{F}}}{c}\frac{2897.8\times10^{-6}\,\text{mK}}{2\pi T} \tag{50}$$

Of the characteristic lengths pertaining to the material itself, the penetration depth, mean free path, and tidal displacement are a function of the frequency of radiation and/or the electrical resistance which is related to the scattering time by:

$$\sigma = \frac{Ne^2\tau}{m} \tag{51}$$

The calculation of these lengths requires values for the number density of free electrons, N, the effective electron mass, m, and the dc electrical conductivity, σ. The

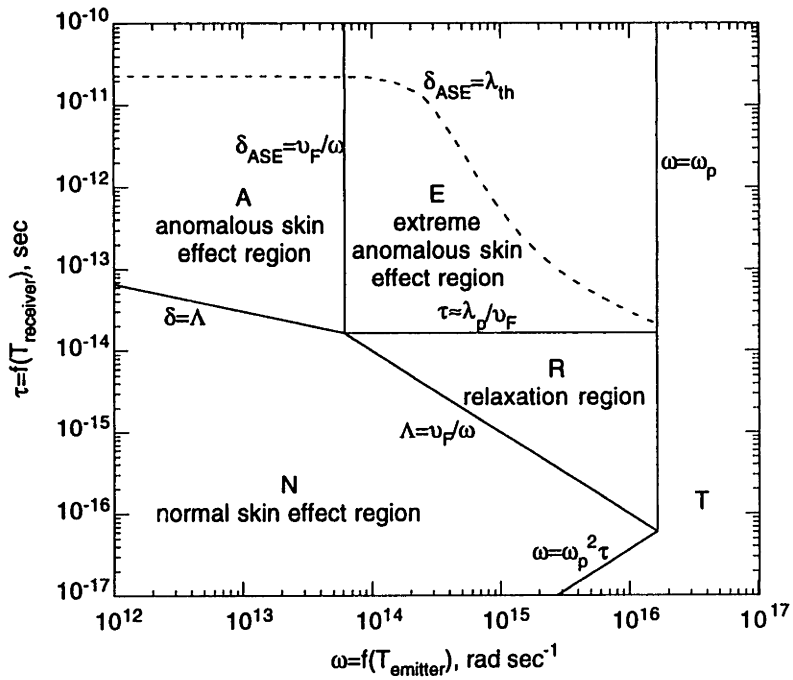

Figure 14: Scattering time versus frequency diagram showing electronic transport regions for copper.

number density and the effective electron mass were obtained from Dugdale (1977). The temperature dependence of the dc electrical conductivity was obtained from the Bloch-Grüneisen formula (Wilson, 1953), and the electrical resistivity was calculated using Matthiessen's rule (MacDonald, 1956), using the room-temperature resistivity data reported by Dyos and Farrell (1992). By equating the expressions for these characteristic lengths, a number of electronic transport regions can be delineated. As shown in Fig. 14, there are five regions. Each line represents the points where two particular characteristic lengths are equal. Wooten (1972) provides a more detailed discussion.

The regions in Fig. 14 indicate the different electronic transport phenomena that are encountered when a body absorbs electromagnetic radiation. When predicting the net radiative flux, the electronic transport phenomena must be correctly accounted for in the models used for the material properties and must be consistent with the theoretical framework. For instance, in the anomalous skin effect region, the model for the material

properties used in any theoretical prediction must account for the variation in electric field between electronic collisions. In the normal skin effect region, a constant electric field is sufficient. Included in Fig. 14 is a line which shows the frequencies for which the thermal deBroglie wavelength equals the penetration depth for the anomalous skin effect (dashed line), a regime not previously discussed in the literature. This region delineates the conditions under which the Boltzmann transport theorem is valid, and its importance will be discussed after considering the regimes.

In the classical skin effect region (region N) the electrons suffer many collisions while within the penetration depth, where there is a local, instantaneous relationship between induced current and the electric field. For higher frequencies, the inertia of the electrons becomes important. In the relaxation region (region R), the electrons suffer many collisions, but the radiation oscillates so quickly that the electrons respond as free electrons only occasionally undergoing a collision. At frequencies higher than the plasma frequency, the reflectance drops to zero, and transmission occurs (region T). Transmission may also occur below the plasma frequency if $\omega\tau>>1$, then the dielectric function approaches unity resulting in zero reflectance and absorptance.

Increasing the scattering time from the normal skin effect region causes an increase in mean free path. In this anomalous skin effect region, (region A) the electric field varies appreciably over the path length. The electron is affected by the electric field in a non-local fashion. The Boltzmann transport equation is employed to determine the electrical conductivity. This region is delineated by the boundary, $\Lambda=\delta$. When the frequency is increased, the electrons experience an increasing number of oscillations within a mean free path; the boundary is determined by $\delta=v_F/\omega$. This region, called the extreme anomalous skin effect region (region E), is similar to the relaxation region except that collisions are much less frequent and almost entirely at the surface. The condition

for surface collisions to be of equal importance to those with the lattice is $\Lambda=\delta$, where in these regions it is roughly equal to the plasma wavelength.

Note that the scattering time depends solely on the temperature of the material (Eq. 51). If it is assumed that the frequency of the radiation is characterized by the frequency where the emissive power of a black body is maximum (λ_{Wien}), then the frequency can be replaced by the temperature of the Planck distribution to which Wien's wavelength corresponds. The temperatures of the receiver and emitter, therefore, determine the appropriate electronic transport region. The temperatures, however, also govern the thermal exchange of energy, and therefore the temperature can be used to (i) form a set of regimes for microscale radiative transfer and (ii) group the experiments into these regimes.

To form a set of regimes for the case of two surfaces exchanging thermal radiation, a combination of the electronic transport in each of the two surfaces is chosen (e.g. both in the normal skin effect region). Next, the limits on the temperature of each surface for the particular transport phenomenon is determined by using Eq. 51 and the Bloch-Grüneisen formula for the temperature dependence of the dc electrical conductivity. This procedure is repeated for all the combinations of electronic transport phenomena to form a complete set of regimes. Graphically, this is achieved by plotting the electronic transport regions as $T_{receiver}$ versus $T_{emitter}$ for a given surface as in Fig. 15. Then, reverse the roles of the hot and cold surfaces and re-plot Fig. 15. Now, the vertical axis is the hot temperature, and the horizontal one is the cold temperature. By superimposing one set of regions on the other set, intersections of the electronic transport regions for each surface arise. These intersections define the regimes of microscale radiative transport for the exchange of thermal energy between metallic surfaces.

Figure 16 shows the regimes for chromium, and Figure 17 shows those for copper. Table 2 indicates the combinations of electronic transport phenomena that characterize

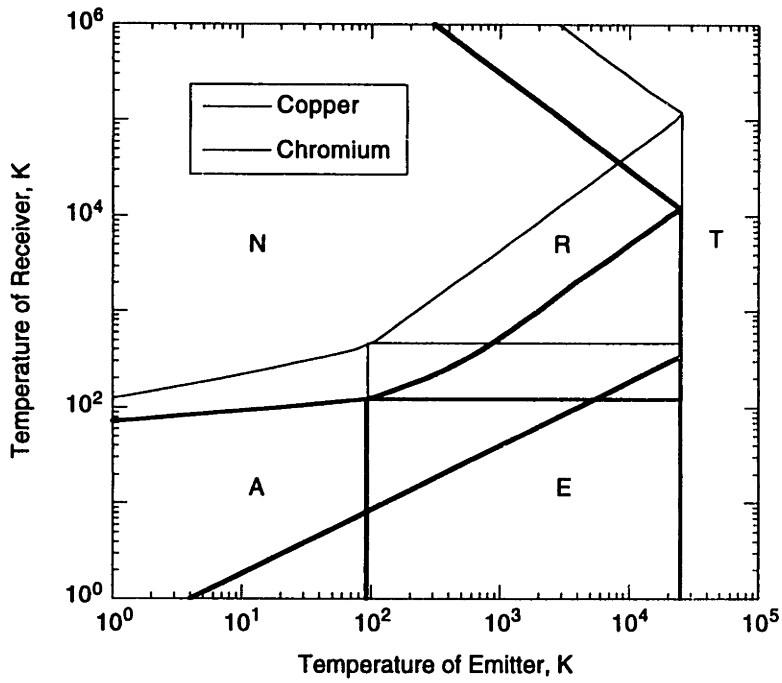

Figure 15: Electronic transport regions for copper surfaces (thin line) and chromium surfaces (thick line) as functions of temperature.

each regime. For instance, regime 1 shows the temperature range for which the hot surface and the cold surface are both in the anomalous skin effect region. The two dashed lines indicate the regions of the regimes for which the Boltzmann transport equation is valid and where the system is near thermodynamic equilibrium.

The regimes indicate that to ensure that both media are in the same electronic transport region, the temperature difference must be kept relatively small, and additionally, there are some temperatures for which it is very difficult to achieve this. (The temperature difference must approach zero.) For some materials (i.e. copper), there is no regime where the absorption in both surfaces is characterized by the normal skin effect. Due to the high electrical conductivity of such materials, the scattering time for which the electrons experience the normal skin effect is large, and thus the normal skin effect exists only at sufficiently low frequencies. The temperature of the emitter would have to be colder than the receiver, which is clearly impossible in a system of two

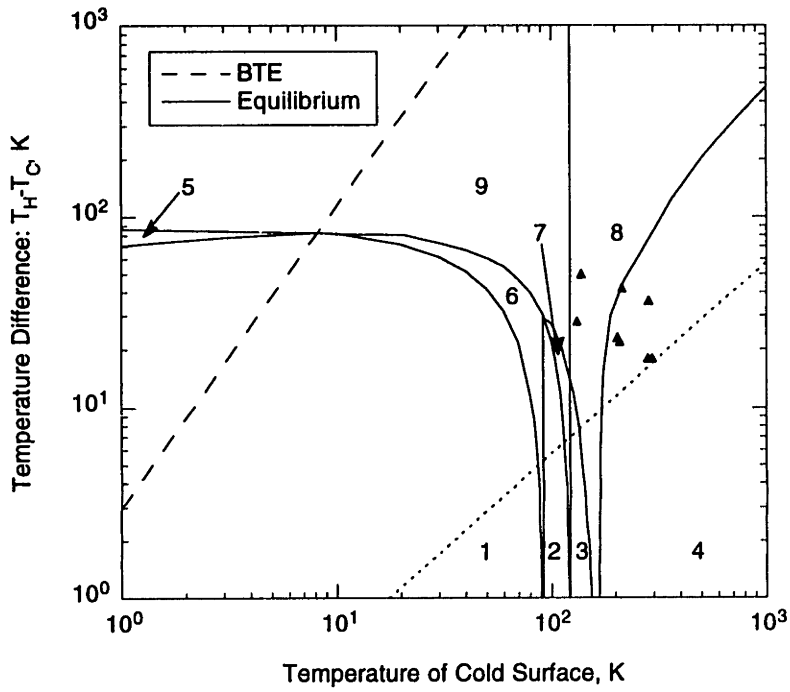

Figure 16: Microscale regimes for radiative transfer between surfaces of chromium. Hargreaves (1973), triangles.

surfaces. As a result, for some materials there are no frequencies of significant power for which both surfaces experience the normal skin effect.

Figures 16 and 17 indicate that the experimental measurements do not lie within the same regime. The measurements of Hargreaves (1973) lie within a regime for which the electronic transport in at least one surface is in the normal skin effect and the system is near equilibrium. All the other measurements lie in regions in which the anomalous skin effect determines the nature of the absorption process. Moreover, the measurements which display the most striking deviations from the results of Hargreaves (1973) are in regimes most different from those of Hargreaves (1973): i.e. far from equilibrium and where absorption in both surfaces is dominated by the anomalous skin effect. The high temperature results of Kutateladze et al. (1979) have a similar spacing trend as Hargreaves (1973) and lie in a regime in which one surface meets the conditions of the

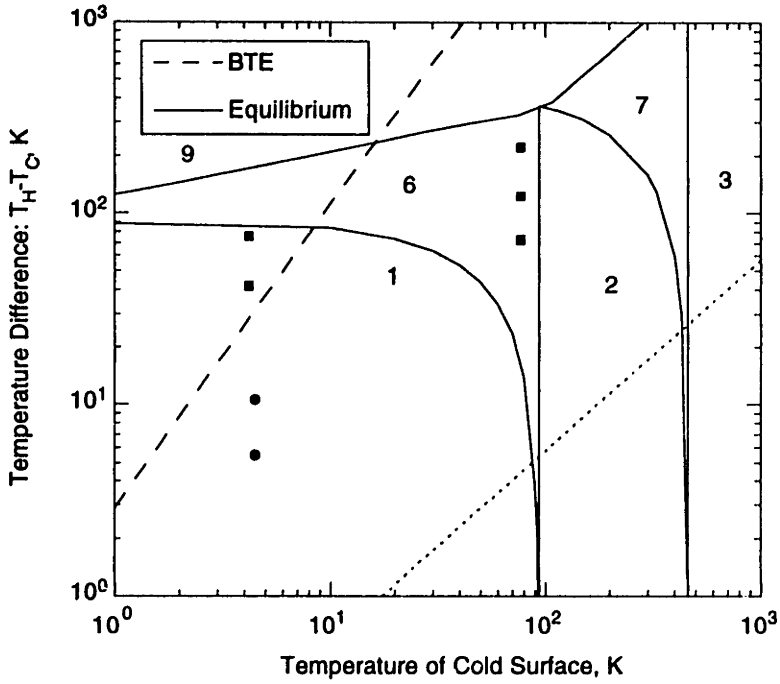

Figure 17: Microscale regimes for radiative transfer between surfaces of copper. Domoto et al. (1970), circles; Kutateladze et al. (1979), squares.

extreme anomalous skin effect. The extreme anomalous skin effect, like the normal skin effect is characterized by a local relationship between the current and electric field.

Moreover, the measurements which display the most striking deviations from the results of Hargreaves (1973) are in regimes most different from those of Hargreaves (1973): i.e. far from equilibrium and where absorption in both surfaces is dominated by the anomalous skin effect. The high temperature results of Kutateladze et al. (1979) have a similar spacing trend as Hargreaves (1973) and lie in a regime in which one surface

Regime Number	Hot Surface	Cold Surface
1	Anomalous Skin Effect	Anomalous Skin Effect
2	Extreme ASE	Extreme ASE
3	Relaxation Region	Relaxation Region
4	Normal Skin Effect	Normal Skin Effect
5	Anomalous Skin Effect	Extreme ASE
6	Extreme ASE	Anomalous Skin Effect
7	Anomalous Skin Effect	Relaxation Region
8	Relaxation Region	Normal Skin Effect
9	Extreme ASE	Normal Skin Effect

Table 2: The characteristics of the regimes for microscale radiative transfer of thermal energy between metallic surfaces.

meets the conditions of the extreme anomalous skin effect. The extreme anomalous skin effect, like the normal skin effect is characterized by a local relationship between the current and electric field.

4.3 Comparison of Measurements to Theoretical Predictions

Chapter 3 presented proximity functions, which account for the spacing effect of the net radiative transfer of thermal energy. Recall that the formulation of this proximity function rests on the use of a fluctuation-dissipation theorem that is valid strictly for macroscopic systems in thermal equilibrium. The use of such an equilibrium law is acceptable for non-equilibrium situations provided that the transport phenomena required to maintain steady-state conditions are insignificant when compared with the irreversible process of interest. (In the present case, the energy input required to maintain the temperature of the high-temperature surface must be insignificant compared to the energy emitted by that surface into the gap.) This prediction also relies on a model for the dielectric function which is valid only when the normal skin effect characterizes the absorption process. Given these limitations to this prediction, the theory can only be compared to the highest temperature measurements of Hargreaves (1973) (i.e. it is valid for only a single microscale regime.

Figure 18 illustrates the results of the prediction for a mean temperature 304 K, and Figure 19 illustrates the results of the prediction for a mean temperature 291 K. These figures show the results for which the dc conductivity was obtained from data for the resistivity of chromium and a prediction for which the dc conductivity was set to fit the measured flux at large spacing. The difference in dc conductivity is only about a factor of 1/3, a reasonable agreement considering that the complexity of the Fermi surface for chromium is not captured in these calculations, which use the Drude model of the dielectric function. Both the trend and the onset of the effect coincide in a reasonable fashion.

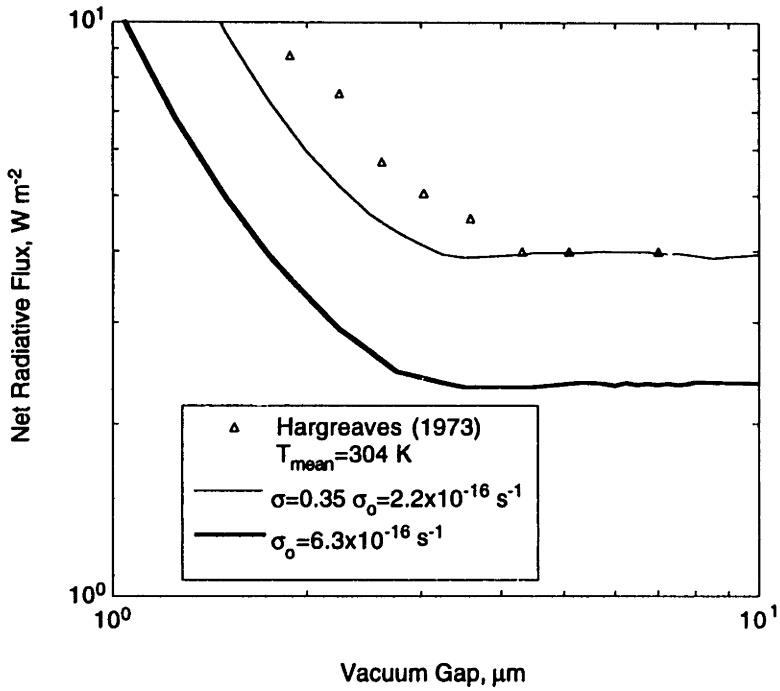

Figure 18: Comparison of the measurement and prediction of the net radiative flux versus gap size using the proximity function of Eq. 36 for T_{mean}=304 K.

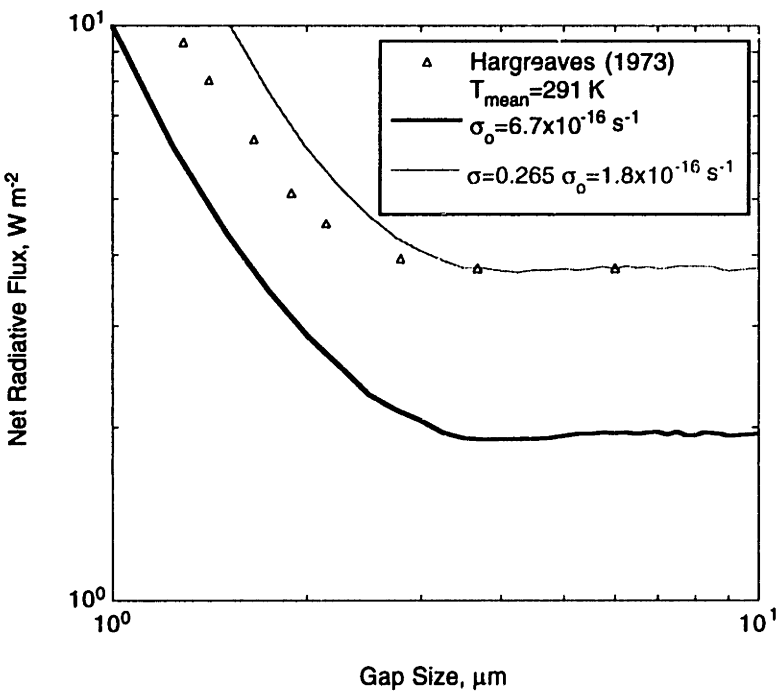

Figure 19: Comparison of the measurement and prediction of the net radiative flux versus gap size using the proximity function of Eq. 36 for T_{mean}=291 K.

There is a steep increase in the net radiative flux (d^{-4}) as the gap decreases. Contrary to Boehm and Tien (1971) and Levin et al. (1980), this prediction using the proximity function does not indicate a minimum in the radiative flux prior to the steep increase, as is born out by the measurements. This approximation does not account for the gradual decrease in the slope of the flux prior to the constant region shown in Fig. 12, but these expressions are still useful for comparison to experimental measurements, since the data do not extend down to this region.

Predictions for the measurements which lie in other regimes do not show any agreement with the experimental measurements. Predictions using properties of copper at low temperature indicate a slightly lower slope, but it is not as low as the measurements. This trend arises from the prominence of the long wavelength radiation at low temperature, where the parallel-polarized component of the near field tends to modify the energy distribution at larger gaps than the perpendicularly-polarized component. The large deviations are not surprising considering that the restrictions of the theory do not meet the conditions of the experiments.

4.4 Discussion

The regimes indicate the importance of matching the theoretical framework to the conditions inherent in the experimental measurements. The limitations in the applicability of the theory and thus the agreement between the predictions and measurements is due to the limits of the fluctuation-dissipation theorem and to inappropriate techniques used to model the material properties of the media.

These limitations make it impossible to clarify the outstanding differences between the predictions and measurements. Levin et al. (1980) dismiss the results of Domoto et al. (1970) and Kutateladze et al. (1979) as erroneous simply because the measurements do not agree with the predictions. Levin's predictions, however, did not account for the effect of the perpendicularly-polarized component of the near field and so should not

exhibit the steep rise to a region of constant flux. Xu et al. (1994) measured a normalized radiative flux of 125 for a gap of 0.05 μm in the ac limit and the same ratio at 0.15 μm in the dc limit. For these gap dimensions, the theory predicts a net radiative flux at least an order of magnitude greater than their results. Though Hargreaves's (1973) results agree reasonably well to the predictions, the remaining differences mandate a more detailed account of the interactions between the photons and the electrons in future theoretical formulations.

Improvements to the theory to expand its applicability to other regimes must focus on the implementation of the fluctuation-dissipation theorem. This theorem models the statistics of the source of the thermal radiation field by relating the statistical variation of the thermal source to the mean energy of a quantum oscillator and the permittivity tensor of the material (Rytov et al., 1987). The theorem, therefore, links the equilibrium thermal properties of the system to material properties of the surfaces. There are two distinct problems to solve in order to extend the theory: (i) how to model the material properties for the appropriate absorption process and (ii) how to model the statistics of the thermal sources for non-equilibrium or non-linear systems (i.e. where the anomalous skin effect is important).

First, consider modeling the material properties. Each element of the permittivity tensor is a dielectric function, which relates a component of the electric field to the electric displacement in a particular medium. For an isotropic, non-magnetic metal, the complex dielectric function consists of a constant real part and a frequency-dependent electrical conductivity in the imaginary part. The modeling of this frequency-dependent conductivity is crucial to account properly for the effects in each electronic transport region. For the normal skin effect case, where the electric field does not vary over the length of the mean free path, current and electric field are related locally by Ohm's law. The Drude expression predicts the conductivity reasonably well with a frequency-

independent scattering time. Predictions using the Drude expression should be applicable to most of Hargreaves (1973) measurements, being in regime 1 where both surfaces experience the normal skin effect. When the mean free path is large, the spatial and temporal variation of the electric field becomes important. Ohm's law is no longer valid, and there is a non-local relationship between the current and electric field. In this case, the Boltzmann transport equation must be solved. Reuter and Sondheimer (1948) solved the Boltzmann equation for the case of a varying electric field by assuming a single constant relaxation time and a normally incident electromagnetic field. Modeling the dielectric function with an expression from the Boltzmann transport equation may prove useful for comparison to the high-temperature results of Kutateladze et al. (1979), which are located in a regime where the anomalous skin effect and extreme anomalous skin effect dominate the electronic transport.

At low temperatures, the penetration depth becomes comparable to the thermal deBroglie wavelength. Polder and Van Hove (1971) correctly point out that their theory is valid only for the case where there is a local relationship between current and electric field. This restriction was made presumably because their implementation of the fluctuation-dissipation theory had a zero-radius correlation function. While Levin et al. (1980) attempted to derive results for the anomalous skin effect by using the Boltzmann transport equation, the approach is limited to relatively high temperatures. This region is included in Fig. 16 and Fig. 17 to indicate where the effect of variation in electric field over the extent of the electron is important (i.e. where the Boltzmann transport equation is not valid). The Boltzmann transport equation can be derived from the fluctuation-dissipation theorem (Chester, 1963a; Kubo, 1966), provided that (i) the thermal deBroglie wavelength is smaller than both the mean free path and the penetration depth and (ii) the interaction time for a collision is smaller than the inverse frequency of the radiation (Chester, 1963b). It is precisely in this region of the regimes where the low temperature

measurements have been performed and where the largest deviations from the theoretical predictions occur. Since the Boltzmann transport equation is not valid for a large temperature difference at a low mean temperature, the dc conductivity must be modeled by some other means.

The second problem with the fluctuation-dissipation theorem is its limitation to cases where the macroscopic system is in thermal equilibrium. Figure 17 and Figure 18 include lines which illustrate when an experiment is far from this condition. In the case of radiation between two surfaces, the system is near equilibrium when the energy removed from the low-temperature surface that is required to maintain its temperature is insignificant compared to the energy emitted by that surface into the gap. The energy removed that maintains the steady-state equals the net energy across the gap, and so the condition for near-equilibrium is:

$$\begin{aligned} &\frac{|P_{conducted}|}{P_{21}} << 1 \\ &\frac{|P_{12}-P_{21}|}{P_{21}} = \frac{|\sigma T_1^4 - \sigma T_2^4|}{\sigma T_2^4} = \frac{|T_1^4 - T_2^4|}{T_2^4} << 1 \end{aligned} \tag{52}$$

The ratio can be made with the high-temperature surface, but since regimes were formed in terms of the low-temperature surface, the ratio is formed with the low-temperature surface for comparison. This choice is more conservative, since this ratio will be larger than that for the high-temperature surface. Assuming that for comparison that near equilibrium exists when this ratio is less than 1/4:

$$\begin{aligned} &\frac{|T_1^4 - T_2^4|}{T_2^4} < \frac{1}{4} \\ &\frac{T_1}{T_2} < \left[\left(\frac{1}{4}\right)+1\right]^{1/4} = 0.057 \\ &(T_1 - T_2) < 0.057\, T_2 \end{aligned} \tag{53}$$

This ratio is a function of spacing. Because radiation begins to tunnel from the cold surface before the hot one due to the longer wavelength, this ratio decreases with spacing until such a gap size that the tunneling of the hot surfaces becomes significant. The "large gap" estimate yields a conservative limit for the temperatures at which equilibrium can be assumed. This temperature difference indicates the upper limit to ensure nearly equilibrium conditions and is represented by the short dashed line in Fig. 16 and Fig. 17. As the cold temperature diminishes, only a very small temperature difference can be tolerated to ensure equilibrium. All but two experiments of Hargreaves (1973) are far from the equilibrium line. Even if the material properties are modeled appropriately for each regime, comparisons to predictions cannot be made until the theory is formulated with a non-equilibrium form of the fluctuation-dissipation theorem. Future experimental measurements should be conducted with as small a temperature difference as possible to permit a comparison to a prediction similar to the one presented here, namely one based on an equilibrium expression for the statistical properties of the system.

This chapter has demonstrated that the experimental measurements are spread across a number of regimes and that these measurements in each regime show distinctly different characteristics. The microscale radiative transfer regimes indicate where the available theoretical predictions are valid and show under what conditions new experiments should be performed. Furthermore, the regimes are a useful tool for the design of experiments, which can verify the available theories by guiding the choice of materials and temperatures to investigate. These regimes have focused attention on several important issues that must be investigated in order to expand the applicability of the theory for the analysis and design of a broader set of heat transfer systems and experiments.

Chapter 5

Analysis of Microscale Thermophotovoltaic Devices

For the remainder of this thesis, attention is focused on a new class of energy conversion devices. These devices constitute the marriage of microscale radiative transfer of thermal energy and thermophotovoltaic energy conversion obtained by bringing the emitter and receiver into close proximity. The fluctuation electrodynamics approach to microscale radiative transfer detailed in the preceding chapters accounts for the spacing effect, which provides the net transfer of photons to the receiver. The receiver converts the photons into useful electrical energy by the photovoltaic effect. This chapter outlines the existing technology, presents a model for a microscale device, and outlines the necessary modifications to the fluctuational electrodynamics formulation for the particular operating conditions and materials.

5.1 Existing Thermophotovoltaic Technology

Thermophotovoltaic energy conversion devices produce electrical power by direct photovoltaic conversion of photons emitted by a heat source. These devices have few components, no moving parts, high power density (1.5-3 W/cm^2), rapid response times, and high potential energy conversion efficiencies (Coutts and Benner, 1995). These attributes make the range of potential applications diverse, including remote electricity supplies (Broman et al., 1996), transportation (Fraas et al., 1995), co-generation (Krist, 1995), electric-grid independent appliances, and space, aerospace, and military power supplies (Regan et al, 1995; Schock et al. 1995).

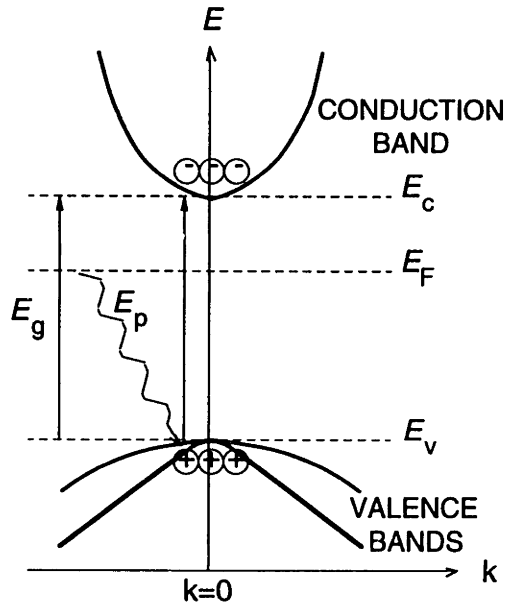

Figure 20: Schematic energy band diagram of a direct band-gap semiconductor.

Though suggested 30 years ago, only recently have efficient conversion materials been developed, raising interest in the potential of thermophotovoltaic energy conversion. While recent improvements in the design of silicon photovoltaic devices have created the prospect of highly efficient energy conversion, it is the ability to manufacture efficient devices from compound semiconductors, which makes thermophotovoltaic energy conversion attractive. By varying the alloy composition, compound semiconductors allow the device response to be tuned to the emission of a particular heat source.

To understand why the ability to tune the device response is important, consider the electronic structure of a semiconductor. Figure 20 depicts schematically the energy bands of a direct band-gap semiconducting material (Pierret, 1987). The energy bands are calculated from a quantum mechanical consideration of the behavior of electrons in the periodic potential formed by the positive lattice ions of the material. These bands describe the allowable energy states that an electron can obtain. The crystal momentum, *k*, accounts for the interaction of the lattice with the electron. A statistical consideration of the electrons reveals that these energy states are filled such that, depending on the

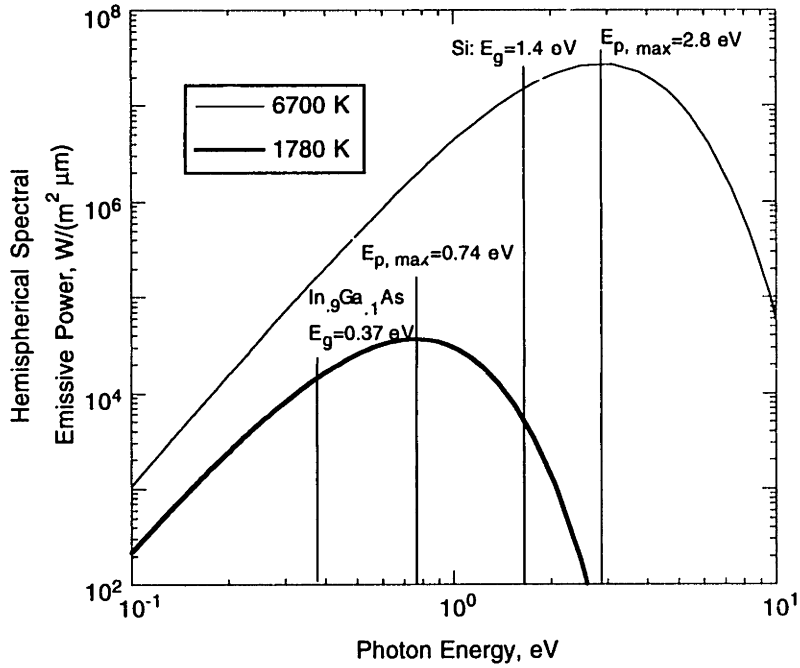

Figure 21: Comparison of band-gap energy and distribution of photon energy according to Planck's distribution of thermal energy.

temperature, the outer valence and conduction bands are only partially filled (Pierret, 1987). The electrons in these bands are free to move, providing conductor-like behavior.

When photons with energy greater than the band gap, E_g, are absorbed, an electron can be elevated to the conduction band leaving a hole in the valence band. The hole and electron are both free to move and contribute to the ability of the semiconductor to conduct a current. By lowering the band-gap energy, photons with less energy can induce a band-to-band electronic transition. Changing the alloy composition of ternary compound semiconductors, such as $In_{1-x}Ga_xAs$, directly affects the magnitude of the band gap (Wojtczuk, 1995). It is the ability to tune the band-gap energy provided by the compound semiconductor that expands the flexibility of thermophotovoltaic systems.

The size of the band gap determines the temperature limits of the emitter. Hot objects emit radiation according to Planck's distribution, as shown in Fig. 21 (Siegel and Howell, 1981). To utilize this energy most effectively, a majority of the photons should

have an energy greater then the band gap of the semiconductor. For an order of magnitude estimate of this relationship, suppose it is desirable to have an band gap low enough that all photons greater than one half the photon energy at the peak of Planck's distribution contribute to band-to-band electronic transitions.

$$\frac{E_{\mathrm{p,max}}}{2} = \frac{1}{2}\frac{hc}{\lambda_{\mathrm{m}}} > E_{\mathrm{g}} \tag{54}$$

This criteria ensures that the greatest number of photons impinging the device induce band-to-band transitions. Using Wien's wavelength for the maximum wavelength gives:

$$\frac{hcT}{2 \times 2897 \mu\mathrm{m}} > E_{\mathrm{g}} \qquad T(\mathrm{K}) > 4665\, E_{\mathrm{g}}(\mathrm{eV}) \tag{55}$$

This relation provides a rough estimate of the source-temperature limits based on the band-gap energy. Figure 21 shows the location of the band gap relative to the peak in Planck's distribution.

For materials such as gallium arsenide and silicon, which have band gaps of about 1.4 eV and 1.1 eV respectively, an appropriate source should be between 5100 K and 6500 K. Such high temperatures make these materials suitable for converting thermal radiation from the sun, which is nearly a black body at 6000 K. The ternary alloy, $In_{1-x}Ga_xAs$, has a band gap that varies between 0.36 eV and 1.4 eV depending on the relative amount of indium and gallium in the compound. For $Hg_{1-x}Cd_xTe$, the range of band gap is even larger, from 0 eV to 1.6 eV. At a band gap of 0.37 eV, a suitable source need be only 1680 K. Such low band gap materials are at the heart of thermophotovoltaic systems, since emitter temperatures in the range of 1000 K to 2000 K are widely attainable. For this reason, $In_{1-x}Ga_xAs$ has been used in many thermophotovoltaic devices. This thesis focuses on $In_{1-x}Ga_xAs$ and $Hg_{1-x}Cd_xTe$ to study the effect of alloy composition on the performance of microscale thermophotovoltaic devices.

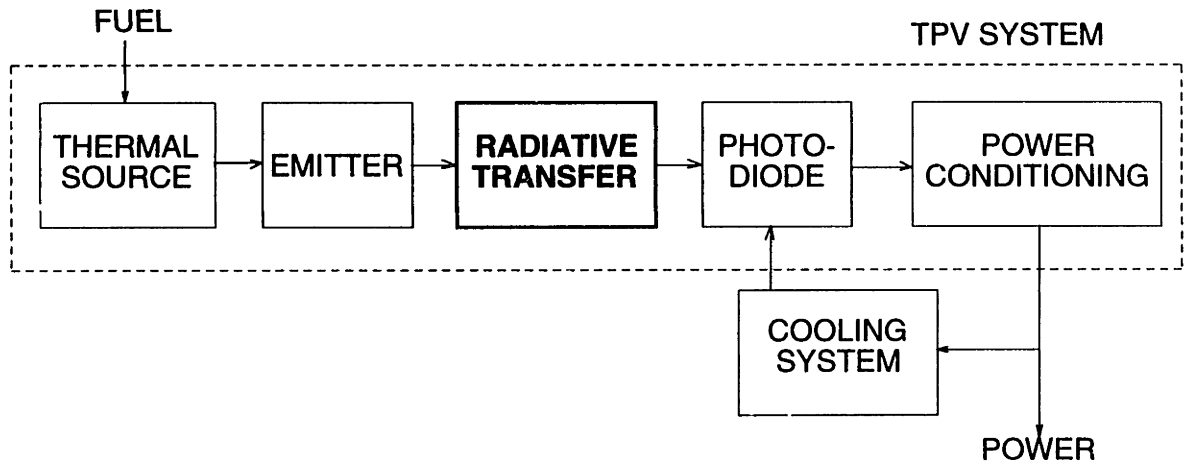

Figure 22: Schematic diagram of a thermophotovoltaic energy conversion system.

Figure 22 shows a schematic representation of a typical thermophotovoltaic system. Currently, a great deal of research is focused on optimizing each sub-system to improve overall performance. A sub-system that converts a fuel to heat drives the thermophotovoltaic system. The particular application of the system often determines the fuel source. Systems have been designed to use energy from fossil fuels, and nuclear, radio-isotope, renewable, and solar sources (Coutts and Benner, 1995). An emitter converts this heat energy to electromagnetic radiation. A photo-diode or pn-junction formed from the new ternary compound semiconductors converts the electromagnetic radiation to electricity. The final sub-system conditions the electric power for the particular application (White and Hottel, 1995).

The overall efficiency of a thermophotovoltaic system depends on the efficiency of each subsystem:

$$\eta^{TPV} = \eta_{comb.} \cdot \eta_{transf.} \cdot \eta_{diode} \cdot \eta_{pwr.\text{-}cond.} \tag{56}$$

White and Hottel (1995) examined the efficiency of each sub-system in order to estimate the upper limit of the overall thermophotovoltaic energy conversion efficiency. Their results indicate an upper limit of 13% and suggest that the most inefficient sub-system is

that involving the emitter and radiant transfer from the emitter to the diode. White and Hottel (1995) give typical values for the efficiency of each sub-system in Eq. 56.

$$\eta^{TPV} = (0.7)(0.35)(0.6)(0.9) = 0.13 \tag{57}$$

Improving the efficiency of the transfer of energy from the emitter to the receiver offers the greatest promise to increase the overall performance of thermophotovoltaic devices.

Net power density output is also a very important performance parameter. The primary cost of the thermophotovoltaic energy conversion system are the pn-junctions that form the receiver. Because the devices produce power from a source of energy *flux*, the systems are designed on a per unit area basis. By increasing the power density (the power per unit area facing the emitter) great savings may be achieved in initial costs, while providing weight and size reductions. The design goal would be to achieve this with little or no loss in efficiency.

5.2 Microscale Thermophotovoltaic Devices

The analysis of the spacing effect in Chapter 2 indicates that larger increases in the net heat flux result when the vacuum gap between the surfaces is small. Moreover, the spectral distribution of the electromagnetic radiation is substantially different from Planck's distribution. The remaining sections of this chapter investigate the possibility of exploiting the spacing effect on radiative transfer to enhance the performance of thermophotovoltaic devices. By bringing the emitter and receiver closely together, energy density will increase, but the effect on device performance is not obvious because of the complex and coupled influence of surface temperature, alloy composition, and gap size. Presented here is a model to investigate the influence of these parameters on the theoretical device performance.

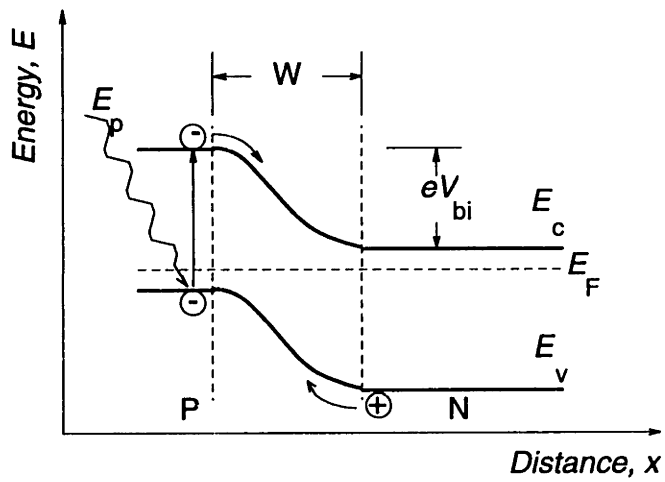

Figure 23: Schematic energy band diagram of a pn-junction.

5.2.1 Model for a Standard Thermophotovoltaic Device

In standard thermophotovoltaic devices, power from the absorbed photons is extracted by a diode junction fabricated with semiconductor materials. This diode is a metallurgical junction formed by bringing together semiconductors that have been doped with impurities so that the conduction and valence bands on each side of the junction have a different concentration of electrons and holes. Materials doped with donor impurities (n-type) have a greater concentration of electrons in the conduction band, whereas those doped with acceptor impurities (p-type) have few electrons in the valence band creating a higher concentration of holes. Asymmetry in the electronic structure results in a pn-junction when an n-type and p-type material are joined.

The energy band diagram of such a junction is shown in Fig. 23, where the spatial variation of the bands in the vicinity of the junction is illustrated. Because a system in thermal equilibrium may have only one Fermi level, the energy bands on the p-side are elevated above those of the n-side forming a potential barrier. Far enough away from the junction, conditions are similar to the unperturbed doped material.

The carrier concentrations corresponding to Fig. 23 are shown in Fig. 24. Note that for high doping, the impurity concentrations, N_A and N_D, are large, resulting in a great

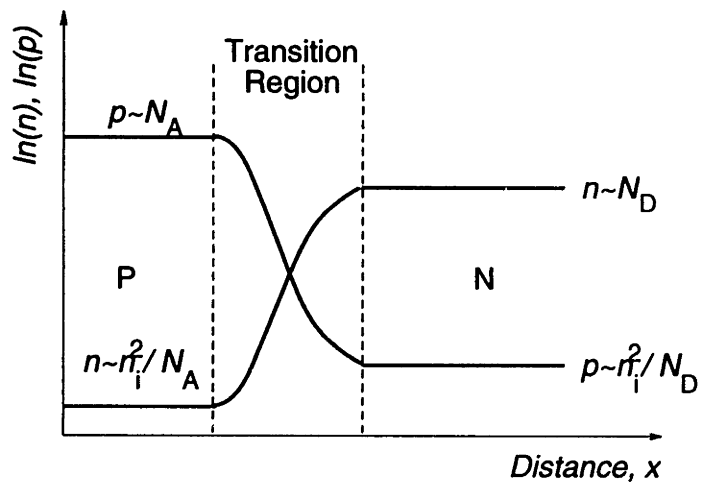

Figure 24: Majority and minority carrier concentrations near the depletion region of a pn-junction (Green, 1982).

difference between the concentration of majority and minority carriers on each side of the junction. The intrinsic carrier concentration, n_i, shown in Fig. 23, figures prominently in the quantitative calculation of carrier concentration. Its square equals the product of the concentration of majority and minority concentrations (Pierret, 1987).

$$n_i^2 = N_c N_v \exp\left(-E_g / k_b T\right) \tag{58}$$

where N_C and N_V are the effective density of conduction band and valence band states, respectively (Pierret, 1987).

The current voltage characteristics of such a junction can be determined by accounting for the drift and diffusion of electrons and holes across the junction. Due to the variation in carrier concentration, there is both a concentration gradient and a potential gradient in the diode. Accounting for the flux of holes and electrons under dark and illuminated conditions reveals the current-voltage characteristics of pn-junctions used for solar cell applications. Figure 25 shows that since the current-voltage curve crosses the 4th quadrant, power can be extracted from the device (Green, 1982).

In the dark, there is a small saturation or dark current, I_d, at zero voltage. This dark current plays an important role in determining the system performance and greatly

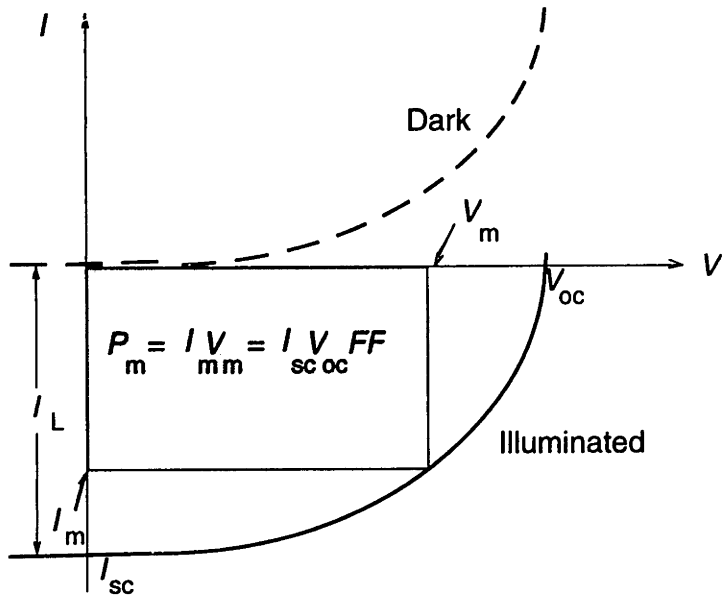

Figure 25: Current voltage characteristics of a solar cell (Green, 1982).

depends on the manner in which a particular junction is manufactured. Methods to estimate this parameter are discussed in the next chapter. When illuminated, the entire current-voltage curve shifts down into the fourth quadrant by an amount, I_L, the light-generated current. The maximum power from the device is obtained by maximizing the shaded area in Fig. 25. This maximum power is related to the open-circuit voltage and short-circuited current by a device parameter called the fill-factor (Schock et al., 1995).

$$\begin{aligned} P_m &= I_{sc} V_{oc} FF \\ V_{oc} &= \frac{k_b T}{e} \ln\left(\frac{I_{sc}}{I_d} - 1\right) \\ FF &= \left[1 - \frac{1}{\ln\left(I_{sc}/I_d\right)}\right]\left[1 - \frac{\ln\left(\ln\left(I_{sc}/I_d\right)\right)}{\ln\left(I_{sc}/I_d\right)}\right] \end{aligned} \tag{59}$$

where k_b is Boltzmann's constant, T, is the temperature of the device, and e is the charge of an electron. The light-generated current is given by the volumetric carrier generation rate, G, times the active volume of the cell, AL:

$$I_L = eGA(L_e + W + L_h) \tag{60}$$

or per unit area:

$$I_L = eG(L_e + W + L_h) \tag{61}$$

where W is the size of the depletion region in the vicinity of the metallurgical junction, which is much less than the diffusion lengths of electrons, L_e, and holes, L_h. These diffusion lengths are characteristic decay lengths of the current density in the diode and are related to the carrier diffusion coefficient, D, and carrier lifetime, τ, by (Green, 1982):

$$L_e = \sqrt{D_e \tau_e} \text{ and } L_h = \sqrt{D_h \tau_h} \tag{62}$$

To estimate the efficiency of the thermophotovoltaic device, the maximum power is compared to the net radiative power incident on the diode.

$$\eta^{TPV} = \frac{P_m}{P_{inc}} = \frac{I_{sc} V_{oc} FF}{P_{inc}} \tag{63}$$

where P_{inc} is the total incident energy flux integrated over all frequencies and I_{sc} is assumed to be equal to the light-generated current, I_L. This current is calculated by taking the product of the spectral flux of photons with energy greater than the band-gap energy, $\Phi_{p\lambda}$, and the charge of an electron.

$$I_L = e \int_{E_g}^{\infty} \left[\Phi_{p\lambda} Q_e \right] dE \tag{64}$$

The factor Q_e is the quantum efficiency, which accounts for the fraction of photons at a particular energy above the band gap that recombine without contributing to the current. The photon flux is simply the total energy flux at a particular frequency divided by the energy of a photon at that frequency. In this manner, the flux of photons incident on the

diode of a standard thermophotovoltaic device is given by Planck's distribution divided by the photon energy (Iles, 1995).

Comparison of Eq. 61 and Eq. 64 indicates that for standard thermophotovoltaic devices, it is assumed that the total flux of photons is absorbed uniformly over the active region (L_e+W+L_h). The quantum efficiency, therefore, accounts for the variation of this active region with frequency, since very short or long wavelength radiation will be absorbed far from the junction and the electron-hole pair will recombine without contributing to the current. In actual fact, the active region is larger than a typical device thickness, but it provides a measure of the recombination occurring in the diode. It serves as a convenient indicator of the recombination by examining its change with photon flux– an important aspect of microscale thermophotovoltaic devices.

5.2.2 Model for a Microscale Thermophotovoltaic Device

The microscale fluctuational electrodynamic field indicates that there will be a great increase in photon flux at a particular frequency as the vacuum gap decreases. This increased flux will increase the injected carrier concentration. There is, however, a limit to the current generated by the increased photon flux. The carrier lifetime and the active region depend, by Eq. 62, on the magnitude of the recombination effects.

Radiative recombination, Auger recombination, and recombination by traps all contribute to decreasing the lifetime (Pierret, 1987; Green, 1982). Recombination by traps involves the two-step process whereby electrons relax from the conduction band to an energy level between the conduction and valence bands introduced by doping impurities. As a result, this form of recombination is determined by the dopant level. Radiative recombination and Auger recombination depend on the concentration of the carriers themselves, since these recombination mechanisms arise from interactions between the carriers. The increased photon flux will act to decrease the carrier lifetime and therefore, since the minority carriers exist for a shorter period of time, less make it

across the depletion width and to the contacts: i.e. the effective active region of the diode decreases as the vacuum gap between the emitter and receiver decreases.

To account for recombination effects, it cannot be assumed that the active region is a constant as implied by Eq. 64. To model the variation of carrier lifetime with generation rate, combine Eq. 61 and Eq. 62, neglecting the depletion width, W, which is much smaller than the diffusion lengths. Assuming the mean lifetime for holes and electrons is approximately equal yields an expression for the light-generated current.

$$I_L = e\left(\sqrt{D_e} + \sqrt{D_h}\right)\sqrt{\tau}\, G \tag{65}$$

The effect of the recombination mechanisms can be combined to form an effective carrier lifetime (Green, 1982).

$$\frac{1}{\tau} = \frac{1}{\tau_T} + \frac{1}{\tau_A} \text{ where } \tau = \frac{C}{n^2} \tag{66}$$

The subscript T refers to recombination by traps and A refers to Auger recombination. The carrier lifetime is inversely proportional to the square of the carrier concentration (Pierret, 1987) as shown in Eq. 66. For a standard device, the total concentration of the majority carriers is simply the doping level, but for the microscale device the total carrier concentration, n, is the sum of the carrier concentration when dark and when illuminated.

$$n = N_D + G\tau_A \tag{67}$$

where N_D is the impurity dopant concentration. Note that the lifetime due to Auger recombination is used in Eq. 67, since at high generation rates, the carrier concentration will be large enough that Auger recombination dominates. For the p-side of the junction, N_A replaces N_D.

Consider the light-generated current when the gap size is large enough that the generation rate is close to that for the standard thermophotovoltaic devices. The lifetime can be estimated by simplifying Eq. 67 with the assumption that:

$$G\tau_A << N_D \tag{68}$$

Since trap recombination dominates:

$$\frac{1}{\tau} \approx \frac{(N_D)^2}{C} = \frac{1}{\tau_T} \tag{69}$$

and the light-generated current at large vacuum gap size is:

$$\begin{aligned} I_L &\approx e\left(\sqrt{D_e} + \sqrt{D_h}\right)\sqrt{\tau_T}\, G \\ &= eL_0\, G \\ &= e\int_{E_g}^{\infty}\left[\Phi_{p\lambda} Q_e\right] dE \end{aligned} \tag{70}$$

Here, L_0, is the diffusion length at large spacing. The light-generated current is proportional to the injected volumetric carrier generation rate, G.

When the emitter and receiver are brought close together, the carrier injection rate increases. In this limit, Auger recombination dominates:

$$n \approx G\tau_A \tag{71}$$

The carrier lifetime becomes:

$$\begin{aligned} \frac{1}{\tau} &\approx \frac{C}{G^2\tau_A^2} = \frac{1}{\tau_A} \\ \tau_A &\approx \left(\frac{C}{G^2}\right)^{1/3} \end{aligned} \tag{72}$$

and the light-generated current at small vacuum gap size is:

$$I_L \approx e\left(\sqrt{D_e} + \sqrt{D_h}\right) C^{1/6} G^{2/3} \tag{73}$$

As the carrier generation becomes larger, recombination reduces the rate by which the current is generated; the light-generated current is proportional to the 2/3 power of the generation rate. The current still increases with generation rate as the photons tunnel with decreasing vacuum gap size. The light generated current will not increase as quickly as the incident power and, therefore, by Eq. 63, the efficiency will decrease.

The model developed here uses the large spacing result of Eq. 70 as a reference to explore the effect of vacuum gap size on the performance of microscale thermophotovoltaic devices. The carrier generation rate is defined in reference to the active region at large spacing from Eq. 70:

$$G = \frac{1}{L_0} \int_{E_g}^{\infty} \left[\Phi_{p\lambda} Q_e \right] dE = \frac{\Phi_p}{L_0} \tag{74}$$

where Φ_p is the total photon flux. The light-generated current from Eq. 65 becomes:

$$\begin{aligned} I_L &= e\left(\sqrt{D_e} + \sqrt{D_h}\right) \sqrt{\tau} G = eLG \\ &= e \frac{L}{L_0} \Phi_p \end{aligned} \tag{75}$$

where using Eq. 69, the ratio of active regions is given by:

$$\begin{aligned} \frac{L}{L_0} &= \sqrt{\frac{\tau}{\tau_T}} = \left(\frac{C}{n^2 \tau_T} \right)^{1/2} \\ &= \left[1 + \left(\frac{\Phi_p \tau_T / L_0}{N_D} \right)^{2/3} \right]^{-1/2} \end{aligned} \tag{76}$$

To summarize, the microscale thermophotovoltaic device performance is characterized by an efficiency, which compares the maximum output of the diode junction to the incident power:

$$\eta = \frac{P_m}{P_{inc}} = \frac{I_{sc} V_{oc} FF}{P_{inc}} \tag{77}$$

where the open-circuit voltage and fill-factor are given by Eq. 59 and the short-circuit current is:

$$I_{sc} = I_L = \frac{e\Phi_p}{1 + \left(\frac{\Phi_p \tau_T / L_0}{N_D} \right)^{1/3}} \tag{78}$$

where $\Phi_p = \int_{E_g}^{\infty} \left[\Phi_{p\lambda} Q_e \right] dE$

This device model requires as inputs the quantum efficiency, dark saturation current, dopant concentration, and device temperature. Modeling these parameters for particular materials is discussed in the next chapter. In addition, the diffusion coefficients and optical constants of the materials that make the pn-junction must be modeled.

5.3 Modifications to the Fluctuational Electrodynamic Approach

The performance of microscale thermophotovoltaic devices can be evaluated using the fluctuational electrodynamic analysis presented in Chapter 2 to predict the increase in the flux of photons due to the small vacuum gap size. In order to avoid the erroneous application of the theory to microscale thermophotovoltaic energy conversion, it must be ascertained that the present formulation meets the operating conditions associated with thermophotovoltaic devices. This section examines the ability of the theory to account for the large temperature difference between the emitter and receiver and presents a formulation applicable to thermophotovoltaic devices.

5.3.1 Consideration of the Equilibrium Fluctuation-Dissipation Theorem

The fluctuational electrodynamic approach to radiative transfer uses the fluctuation-dissipation theorem to characterize the statistics of the random currents, which give rise to the thermal radiation. As discussed in Chapter 4, the fluctuation-dissipation theorem is

strictly valid for thermodynamic equilibrium. When conditions of local thermodynamic equilibrium exist, however, the theorem still provides accurate modeling of the statistical behavior of the system. Local thermodynamic equilibrium exists when the population of energy states that take part in the absorption and emission process are given, to a very close approximation, by their equilibrium distributions (Siegel and Howell, 1981).

When the radiation flux becomes large, the population of high energy states occurs so strongly that the collisional processes cannot re-populate the lower states adequately enough to maintain the equilibrium distribution. Such conditions exist when very fast or very energetic radiative transfer takes place (i.e. shock phenomena, nuclear explosions, short-pulse laser). An order of magnitude calculation shows that local thermodynamic equilibrium exists for the moderate temperature conditions of interest for thermophotovoltaic systems.

From the derivation of Planck's distribution, the flux of photons in a black-body cavity at a temperature, T, in the frequency range $d\omega$ that impinge a cavity wall is:

$$c\,\phi_b = c\frac{\omega^2 d\omega}{\pi^2 c^3\left(\exp\left(\frac{h\omega}{2\pi k_b T}\right)-1\right)}\frac{\text{photons}}{\text{m}^3} \tag{79}$$

So that the total photon flux over all frequencies is:

$$\begin{aligned}\Phi_p &= \int_0^\infty c\phi_b d\omega \\ &\approx \pi\left(\frac{2k_b T}{hc}\right)^2 \int_0^\infty \frac{u^2 du}{\exp(u)-1} d\omega \\ &\approx 2.5\times 10^{15} T^3 \frac{\text{photons}}{\text{m}^2\text{K}^3\text{s}}\end{aligned} \tag{80}$$

For a metal such as gold, the number of free electrons within the penetration depth, δ, near the surface is:

$$
\begin{aligned}
N_e &\approx \frac{\rho N_{Av}}{M_W} \times \delta \\
&\approx \frac{(19300)6.02 \times 10^{26}}{197} \\
&\approx 6 \times 10^{20} \frac{\text{electrons}}{\text{m}^2}
\end{aligned}
\tag{81}
$$

where ρ is the material density, N_{Av} is Avogadro's number, and M_W is the molecular weight. For local thermodynamic equilibrium, there must be many more electrons than photons:

$$
N_e >> \Phi_p \tau \tag{82}
$$

where τ is the electron-phonon interaction time, which characterizes the relaxation time required for an electron to return to its equilibrium state. For a Drude material, the relaxation time is related to the dc electrical conductivity.

$$
\sigma = \frac{Ne^2 \tau}{m} \tag{83}
$$

where N is the number density of free electrons and m is their effective mass. Table 3 shows the estimate of the electrons within a penetration depth of the surface of gold compared to the number of photons from a heat source at 2000 K that penetrate the surface within a relaxation time. The temperature dependence of the dc electrical conductivity was obtained from the Bloch-Grüneisen formula (Wilson, 1953), and the electrical resistivity was calculated using Matthiessen's rule (MacDonald, 1956), using the room-temperature resistivity data reported by Dyos and Farrell (1992).

Table 3 indicates that local thermodynamic equilibrium conditions exist for thermophotovoltaic systems since the electron-phonon interaction is suitably rapid and the flux of photons is not large within the short interaction period. The equilibrium

surface temperature s	dc conductivity 1/(Ωm)	relaxation time s	Φ_p photons/(m^2 s)	$\Phi_p \tau$ photons/m^2	N_e electrons/m^2
77	223×10^6	1×10^{-13}	2×10^{25}	2×10^{12}	6×10^{20}
300	44×10^6	3×10^{-14}	2×10^{25}	6×10^{11}	6×10^{20}
2000	7×10^6	4×10^{-15}	2×10^{25}	8×10^{10}	6×10^{20}

Table 3: Estimates of the electron and photon number density for local thermodynamic equilibrium considerations.

fluctuation-dissipation theorem, therefore, is valid for analysis of thermophotovoltaic systems.

The particular form of the fluctuation-dissipation theorem used in the formulation presented in this thesis is based on a linear relationship between the current and the electric field in the surface of interest. As discussed in Chapter 4, when such a linear relationship such as Ohm's law is valid, the fluctuational electrodynamic analysis yields a linear set of differential equations. For the case of the normal skin effect, such a linear relationship is valid and a linear form of the fluctuation-dissipation theorem can be used.

Careful attention must be paid to the electronic transport in the receiver. If Ohm's law is not valid, a fluctuation-dissipation theorem that can account for the spatially varying electromagnetic field must be developed. Like the problem of applying the present theory to the low temperature measurements of heat flux examined in Chapter 4, limitations of the theory may be encountered when examining the performance of thermophotovoltaic devices at low temperature.

5.3.2 Fluctuational Electrodynamic Formulation for Large Temperature Differences

In order to calculate the flux of photons and the net incident heat flux, a formulation similar to Chapter 3 is derived for the case of two plane parallel surfaces of different

permittivity and a large temperature difference. Consider the isotropic formulation presented by Eq. 12 and Eq. 13. The denominator of the proximity integrals is:

$$\Delta_{\|} = \left(\frac{k_{z1}}{\varepsilon_1} + k_{zv}\right)\left(\frac{k_{z2}}{\varepsilon_2} + k_{zv}\right)e^{k_{zv}d} - \left(\frac{k_{z1}}{\varepsilon_1} - k_{zv}\right)\left(\frac{k_{z2}}{\varepsilon_2} - k_{zv}\right)e^{-k_{zv}d} \tag{84}$$

Rearranging:

$$\begin{aligned}\Delta_{\|} &= k_{zv}\left(\frac{k_{z1}}{\varepsilon_1} + \frac{k_{z2}}{\varepsilon_2}\right)\left(e^{k_{zv}d} + e^{-k_{zv}d}\right) + \left(k_{z_v}^2 - \frac{k_{z1}}{\varepsilon_1}\frac{k_{z2}}{\varepsilon_2}\right)\left(e^{k_{zv}d} - e^{-k_{zv}d}\right) \\ &= 2k_{zv}\left(\frac{k_{z1}}{\varepsilon_1} + \frac{k_{z2}}{\varepsilon_2}\right)\left(\cosh\left(k_{zv}d\right) + \frac{\left(k_{zv} - \frac{1}{k_{zv}}\frac{k_{z1}}{\varepsilon_1}\frac{k_{z2}}{\varepsilon_2}\right)}{\left(\frac{k_{z1}}{\varepsilon_1} + \frac{k_{z2}}{\varepsilon_2}\right)}\sinh\left(k_{zv}d\right)\right)\end{aligned} \tag{85}$$

Let the sum and product vectors be defined as follows:

$$\begin{aligned} Z_s &\equiv \frac{k_{z1}}{\varepsilon_1} + \frac{k_{z2}}{\varepsilon_2} \\ Z_p &\equiv k_{zv} + \frac{1}{k_{zv}}\frac{k_{z1}}{\varepsilon_1}\frac{k_{z2}}{\varepsilon_2} \end{aligned} \tag{86}$$

And so the denominator of the proximity integral becomes:

$$\begin{aligned}|\Delta_{\|}|^2 &= 4|k_{zv}|^2|Z_s|^2\left[1 + \sinh^2\left(k_{zv}d\right)\left\{1 + \left|\frac{Z_p}{Z_s}\right|^2\right\} + \mathrm{Re}\left(\frac{Z_p}{Z_s}\right)\sinh\left(2k_{zv}d\right)\right] \quad \text{for } k_{zv} \text{ real} \\ &= 4|k_{zv}|^2|Z_s|^2\left[1 + \sinh^2\left(k_{zv}d\right)\left\{1 - \left|\frac{Z_p}{Z_s}\right|^2\right\} + i\,\mathrm{Im}\left(\frac{Z_p}{Z_s}\right)\sinh\left(2k_{zv}d\right)\right] \quad \text{for } k_{zv} \text{ imag.}\end{aligned} \tag{87}$$

With similar substitutions, the proximity integrals can be rearranged, making the wave vector explicitly purely real or imaginary. The following relations provide the effect of spacing for the radiative transfer of thermal energy between surfaces of isotropic materials with different complex permittivity and the permeability equal to unity.

$$M_{\parallel}^{\text{near}} = \int_0^{\infty} \frac{\text{Im}\left(k_{z_1}/\varepsilon_1\right)\text{Im}\left(k_{z_2}/\varepsilon_2\right)}{|Z_s|^2\left[1+\sinh^2(\kappa d)\left\{1+|Z_p/Z_s|^2\right\}+\text{Re}\left(Z_p/Z_s\right)\sinh(2\kappa d)\right]}\kappa\, d\kappa \tag{88}$$

where $Z_s \equiv \frac{k_{z1}}{\varepsilon_1}+\frac{k_{z2}}{\varepsilon_2}$, $Z_p \equiv k_{zv}+\frac{1}{k_{zv}}\frac{k_{z1}}{\varepsilon_1}\frac{k_{z2}}{\varepsilon_2}$, and $\kappa = \sqrt{k_x^2-k^2}$.

$$M_{\parallel}^{\text{far}} = \int_0^{k} \frac{\text{Im}\left(k_{z_1}/\varepsilon_1\right)\text{Im}\left(k_{z_2}/\varepsilon_2\right)}{|Z_s|^2\left[1-\sin^2(\kappa d)\left\{1-|Z_p/Z_s|^2\right\}-\text{Re}\left(Z_p/Z_s\right)\sin(2\kappa d)\right]}\kappa\, d\kappa \tag{89}$$

where $Z_s \equiv \frac{k_{z1}}{\varepsilon_1}+\frac{k_{z2}}{\varepsilon_2}$, $Z_p \equiv k_{zv}-\frac{1}{k_{zv}}\frac{k_{z1}}{\varepsilon_1}\frac{k_{z2}}{\varepsilon_2}$, and $\kappa = \sqrt{k^2-k_x^2}$.

$$M_{\perp}^{\text{near}} = \int_0^{\infty} \frac{\text{Im}\left(k_{z_1}\right)\text{Im}\left(k_{z_2}\right)}{|Z_s|^2\left[1+\sinh^2(\kappa d)\left\{1+|Z_p/Z_s|^2\right\}+\text{Re}\left(Z_p/Z_s\right)\sinh(2\kappa d)\right]}\kappa\, d\kappa \tag{90}$$

where $Z_s \equiv k_{z1}+k_{z2}$, $Z_p \equiv k_{zv}+\frac{k_{z1}k_{z2}}{k_{zv}}$, and $\kappa = \sqrt{k_x^2-k^2}$.

$$M_{\perp}^{\text{far}} = \int_0^{k} \frac{\text{Im}\left(k_{z_1}\right)\text{Im}\left(k_{z_2}\right)}{|Z_s|^2\left[1-\sin^2(\kappa d)\left\{1-|Z_p/Z_s|^2\right\}-\text{Re}\left(Z_p/Z_s\right)\sin(2\kappa d)\right]}\kappa\, d\kappa \tag{91}$$

where $Z_s \equiv k_{z1}+k_{z2}$, $Z_p \equiv k_{zv}-\frac{k_{z1}k_{z2}}{k_{zv}}$, and $\kappa = \sqrt{k^2-k_x^2}$.

The proximity functions are only functions of the vacuum gap size, d, and the permittivity of the surfaces, ε_1 and ε_2. With Eq. 88 through Eq 91 for the proximity function M, and the mean energy of a quantum oscillator, Θ, from the fluctuation-dissipation theorem (Eq. 8), the energy flux from material 1 to material 2 due to the fluctuational electrodynamic field is:

$$P_{12}(\omega) = \frac{\Theta}{\pi^2}\left\{M_{\parallel}+M_{\perp}\right\} = \frac{\Theta M}{\pi^2} \tag{92}$$

and the spectral photon flux is:

$$\Phi_{p\lambda} = \frac{P_{12}(\omega)}{E_p} = \frac{2\pi}{\hbar\omega} P_{12}(\omega) \tag{93}$$

With Eq. 93 and Eq. 78 for the efficiency, the power produced in the microscale thermophotovoltaic device and the efficiency can be determined as a function of gap size. Such an analysis requires the modeling of the permittivity of each surface as a function of temperature, alloy composition, and frequency. For the device characteristics, the quantum efficiency, dark current, and doping level of the pn-junction are also needed.

Chapter 6

Performance of Microscale Thermophotovoltaic Devices

This chapter presents the performance of the proposed microscale thermophotovoltaic devices modeled in the previous chapter. First, predictions for the optical constants of the materials, which constitute the emitter and receiver, are presented and compared to experimental measurements from literature. Next, expressions for the device parameters are developed. The results of the predicted performance are presented and the influence of temperature, alloy composition, and vacuum gap size are discussed. An analysis of the limitations to microscale thermophotovoltaic energy conversion in reference to the Second Law of thermodynamics is discussed. In the final section, important considerations for the future development of microscale thermophotovoltaic devices are presented. A parameter space is defined as a guide to potential developments of new materials for the future improvement of thermophotovoltaic energy conversion.

6.1 Modeling Material Properties

The permittivity over the entire frequency range is required for the calculation of the photon flux and net heat flux. The permittivity is related to the optical constants of the material (i.e. the refractive index, n, and the extinction coefficient, κ) by the following relation:

$$\varepsilon = (n+i\kappa)^2 \tag{94}$$

In this section, models for the optical constants for the emitter and receiver are presented.

6.1.1 Receiver: Optical Constants

The materials examined in this thesis are chosen to investigate the two main objectives of this evaluation of microscale thermophotovoltaic energy conversion: (i) to explore improvements to existing thermophotovoltaic technology, and (ii) to explore the best possible performance by optimizing the material properties and operating temperatures. To examine the improved performance of existing technology, the receiver is modeled as a pn-junction fabricated from $In_{1-x}Ga_xAs$, since this material is widely used to fabricate thermophotovoltaic devices (Coutts and Benner, 1995). To explore the best possible performance, the ternary alloy $Hg_{1-x}Cd_xTe$ is used to model the material of the device. This material has a high conversion efficiency at long wavelength, making it ideal for converting the near-field energy as the vacuum gap decreases. Its wide-spread use for far-infrared detectors provides a large body of experimental data from which to model a hypothetical pn-junction for thermophotovoltaic energy conversion (Kruse, 1981).

Note that for the relations in this section, the units of energy, E, frequency, ω, and wavelength, λ, are eV, cm^{-1}, μm, respectively.

$In_{1-x}Ga_xAs$

Indium gallium arsenide is a III-V ternary compound semiconductor with a direct band gap that can be varied from 0.35 eV (x=0) to 1.42 eV (x=1) (Wojtczuk et al., 1995). This alloy has a high electron mobility making it an ideal material for fast opto-electronic devices (Heime, 1989). While this material's electronic properties have been well-studied, it has only recently been used for photo-diode applications, and therefore, the data for permittivity are scarce. As $In_{1-x}Ga_xAs$ continues to be used for such devices, more data should become available. Since the standard thermophotovoltaic device fabricated from these alloys is operated at room-temperature to minimize the cooling load, only the room-temperature performance is investigated.

Wojtczuk et al. (1995) report the band-gap energy as a function of lattice constant. A curve fit to their data yields an expression for the band gap, E_g, in eV as a function of alloy composition, x, at 300 K.

$$E_g(x,T) = 0.35 + 0.5x + 0.59x^2 \tag{95}$$

For photons with an energy just below the band gap, there is no absorption. Not until the photon energy is far below the band gap does absorption increase, although at such low energy, new minority electrons or holes are not created. The optical behavior in this region is determined by the lattice oscillations, free-carrier absorption, and optical phonons. Because the thermal energy being radiated at such frequencies is small compared to that at the peak, a rough model for the absorption will suffice. The permittivity used here is based on the fitting parameters for p-type GaAs at room temperature (Hebb, 1993), excluding the contribution of intersubband transitions, since the error is very small. The permittivity in this region is:

$$\varepsilon(\omega) = \varepsilon_\infty + \varepsilon_\infty\left(\omega_L^2 - \omega_T^2\right)/\left(\omega_T^2 - \omega^2 - i\omega\Gamma\right) - \omega_p^2/\left(\omega^2 + i\,\omega/\tau\right) \tag{96}$$

where ω_L and ω_T are the longitudinal and transverse phonon frequencies and Γ is the damping coefficient. Palik (1985) gives ω_L=292.1 cm^{-1} and ω_T=268.7 cm^{-1} and Γ=2.4 cm^{-1}. The permittivity, ε_∞, is the value of $\varepsilon(\omega)$ at frequencies very much larger than the phonon oscillations in the absence of free carriers, which Hebb (1993) gives as 11. The last term describes the contribution of the free carriers, where ω_p is the plasma frequency, and τ is the scattering time. The plasma frequency and scattering time are related to the free carrier density , N, and the mobility, μ, through:

$$\omega_p^2 = \frac{Ne^2}{m^*\varepsilon_0}$$
$$\tau = \frac{\mu m^*}{e} \tag{97}$$

where m^* is the effective mass of the charge carrier. Hebb (1993) provides a rationale for using $m^*=0.5m_0$ and $\tau=2\text{x}10^{-14}$s.

Above the band gap, the dominant shape of the variation of the permittivity is determined by transitions between the various electronic bands. Yakovlev (1994) performed ellipsometric measurements in the near-ultraviolet, visible, and near-infrared for x=0, 0.7, 0.8, and 1.0. For this study, Yakovlev's data were tabulated and a linear interpolation between the values for x at any particular frequency was performed to calculate the optical constants.

The dispersion in the refractive index near the band gap is less than 1% and so for the range of energy 0.05 eV to 1.5 E_g an average result is obtained by interpolating between the low-energy values reported by Yakovlev (1994):

$$n \approx \sqrt{\varepsilon_\infty} = 3.32 \tag{98}$$

For the extinction coefficient near the band-gap energy, a simple relation from Amirtharaj (1991) is fit to the data of Jain et al. (1996).

$$\kappa = \frac{\lambda}{4\pi} \times \beta(1+x)\sqrt{E - E_g} \text{ where } \beta = 2.12 \times 10^4 \tag{99}$$

where λ is in cm, T in K, and E in eV.

Figure 26 shows the optical constants for indium gallium arsenide at 300 K as a function of energy of the photon. Notice that there is good agreement between the available data and the model used in this thesis. Increasing the relative amount of gallium in the alloy causes the band-gap energy to increase. As a result, the absorption edge appears at a higher frequency. This ability to alter the location of the absorption edge permits tuning of the diode to match the peak in the spectrum of energy from the emitter.

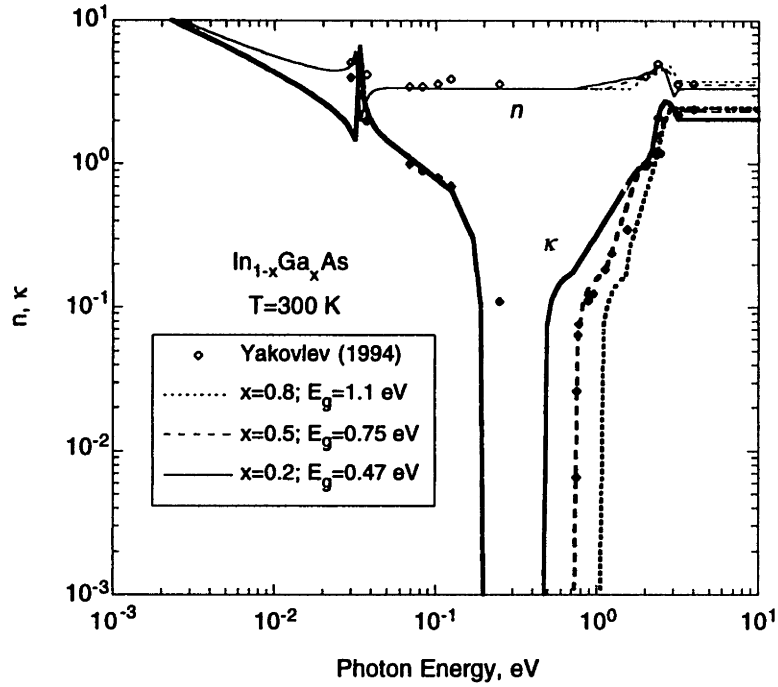

Figure 26: Comparison of the predictions and measurements of the optical constants of $In_{1-x}Ga_xAs$ at 300 K.

$Hg_{1-x}Cd_xTe$

Mercury cadmium telluride is a II-VI ternary compound semiconductor belonging to the zinc-blende family, and therefore, has much in common with well-known materials GaAs and InP. The shape of the permittivity is very similar for most materials in this family, but the precise energy positions of spectroscopic features vary from material to material. The direct gap can be varied from 0 eV (x=0) to 1.6 eV (x=1), which is below the lowest limit of the III-V family of materials. Such a low band-gap energy makes $Hg_{1-x}Cd_xTe$ ideal for infrared detection (Reine et al., 1981).

The distinct regions of absorption depend on the energy of the photon in relation to the band-gap energy. Hansen et al. (1982) derived the following expression for the band gap by analyzing the experimental data in the literature.

$$E_g(x,T) = -0.302 + 1.93x + 5.35\times10^{-4}T(1-2x) - 0.810x^2 + 0.832x^3 \qquad (100)$$

which is valid for $0< x <0.6$ (plus x=1) and 4.2 K$<T<$300 K.

Oscillator	ω_j cm^{-1}	S_j	Γ_j cm^{-1}
1	110	0.3	10
2	123	5.6	3
3	134	0.7	9
4	141	0.15	6
5	149	0.9	4
6	153	0.35	6
7	157	0.15	4

Table 4: Oscillator parameters for the dielectric function of $Hg_{1-x}Cd_xTe$ for photon energy below 0.05 eV.

At energy far below the band gap, the optical behavior is determined by the lattice oscillations, free-carrier properties, impurity transitions, and band-to-band transitions in the narrow-gap alloys. Amirtharaj (1991) reports parameters which fit the classical form of the permittivity for photon energy less than 0.05 eV:

$$\varepsilon(\omega) = \varepsilon_\infty + \sum_{j=1}^{7} S_j^2(\omega)/\left(\omega_j^2 - \omega^2 - i\omega\Gamma_j\right) - \omega_p^2/\left(\omega^2 + i\omega/\tau\right) \qquad (101)$$

where ω is the frequency and the lattice oscillations are treated as damped oscillators with strength, S_j, frequency ω_j, and damping Γ_j, and ε_∞ is the value of $\varepsilon(\omega)$ at frequencies very much larger than the lattice oscillations in the absence of free carriers (i.e. Amirtharaj (1991) gives a value of 16). The last term describes the contribution of the free carriers, where $\omega_p$is the plasma frequency, and τ is the scattering time. The plasma frequency and scattering time are related to the free carrier density, N, and the mobility, μ, through by Eq. 97. Table 4 shows the parameters for the seven oscillators.

Above the band gap, the dominant shape of the variation of the permittivity is determined by transitions between the various electronic bands. Aspnes and Arwin (1984) performed ellipsometric measurements in the near-ultraviolet, visible, and near-infrared for x=0, 0.2, 0.29, and 1.0. For this study, their data were tabulated and a linear

interpolation between the values for x at any particular frequency was performed to calculate the optical constants.

The feature of most studied is the increase in absorption in the vicinity of the band gap due to its importance in optic-electronic devices. The dispersion in the refractive index in this region is less than 1% and so for the range of energy 0.05 eV to 1.5 E_g the average result reported by Finkman and Nemirovsky (1979) is used.

$$n = 2.65 + 1.17(1 - x)^2 \tag{102}$$

For the extinction coefficient, a simple relation from Amirtharaj (1991) provides a reasonable model for the absorption near the band-gap energy.

$$\kappa = \frac{\lambda}{4\pi} \times 2.109 \times 10^5 [(1 + x)/(T + 81.9)] \sqrt{E - E_g} \tag{103}$$

where λ is in cm, T in K, and E in eV.

Figure 27 compares the prediction of the optical constants of $Hg_{.8}Cd_{.2}Te$ at 300 K using the relations reported above to actual measurements over the entire range of frequency needed for this study. The data are taken from a number of sources as compiled and reported by Amirtharaj (1991). There is very good agreement between the data and the prediction. Figure 28 indicates the effect of alloy composition for $Hg_{1-x}Cd_xTe$ at a temperature of 300 K. Note that as the amount of cadmium in the alloy composition increases, the absorption edge occurs at higher frequency and decreases in magnitude. For $Hg_{1-x}Cd_xTe$ at low temperatures, the absorption edge increases in magnitude as indicated in Figure 29.

Comparison of Fig. 26 and Fig. 27 reveals that the absorption edge of the mercury cadmium telluride alloy can be extended to lower energy than that of indium gallium arsenide. This feature makes the $Hg_{1-x}Cd_xTe$ alloy ideal for far-infrared applications.

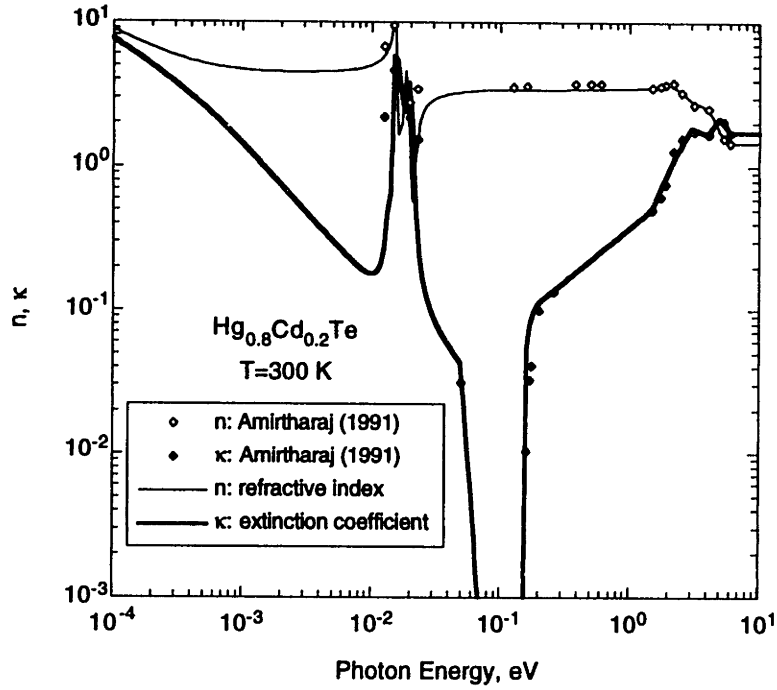

Figure 27: Comparison of model and measurements for the optical constants of $Hg_{.8}Cd_{.2}Te$ at 300 K; calculated from theory fitted to measurements from Amirtharaj (1991).

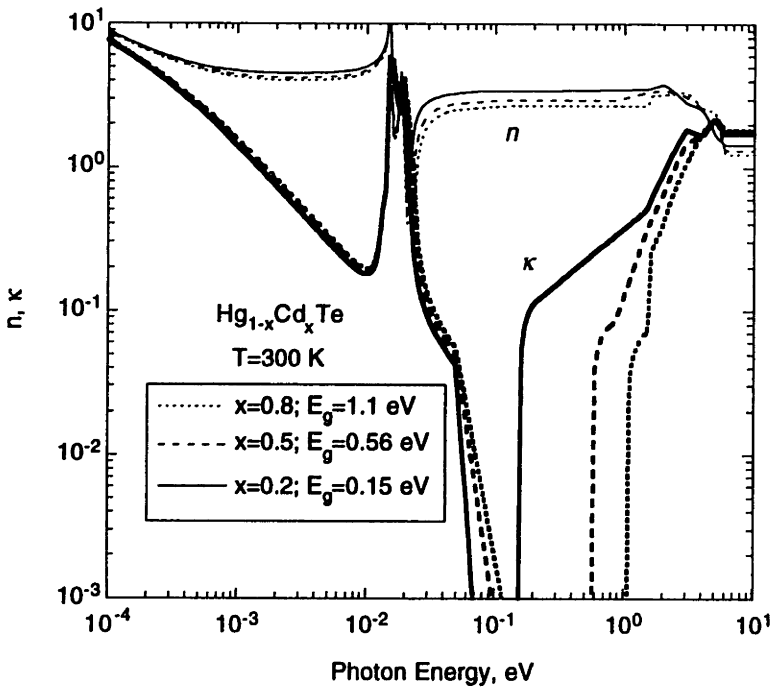

Figure 28: Effect of alloy composition on optical constants of $Hg_{1-x}Cd_xTe$ at 300 K; calculated from theory fitted to measurements from Amirtharaj (1991).

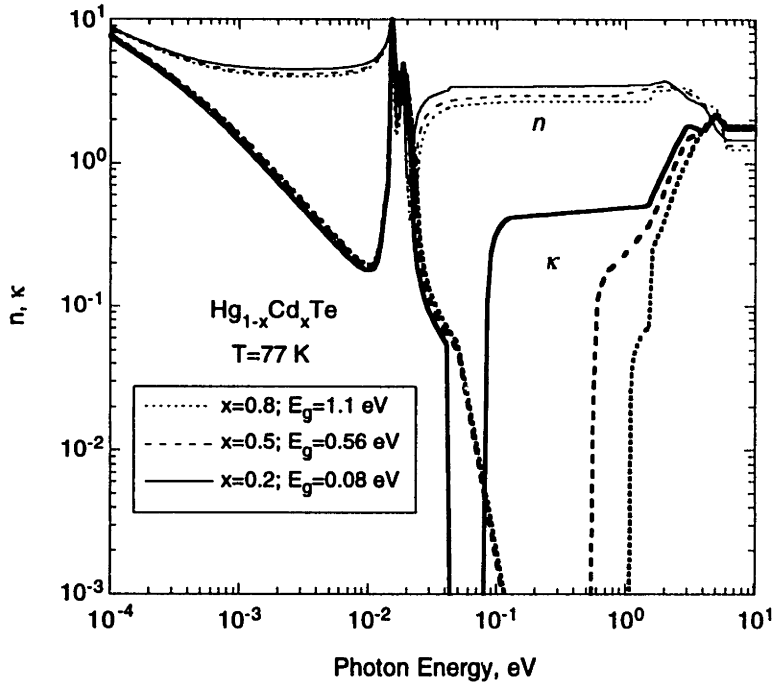

Figure 29: Effect of alloy composition on optical constants of $Hg_{1-x}Cd_xTe$ at 77 K; calculated from theory fitted to measurements from Amirtharaj (1991).

6.1.2 Receiver: Carrier Mobility and Lifetime

In order to account for the reduction of the active region as the generation rate increases due to the small vacuum gap, it is necessary to estimate the diffusion coefficient and carrier lifetime. The diffusion coefficient is related to the mobility by Einstein's relation (Pierret, 1987).

$$\frac{D}{\mu} = \frac{k_b T}{e} \tag{104}$$

The minority carrier lifetime can vary a great deal depending on the doping and dominant recombination mechanism (Pines and Stafsudd, 1980). For the microscale-device model presented in the previous chapter, an estimate only for the lifetime due to the doping (trap recombination) is needed, since Auger and radiative recombination is assumed to vary with the inverse second power of the minority carrier concentration

(Green, 1982). This model is an estimate, accurate for a feasibility analysis, that captures the most important results of more detailed studies of carrier lifetime (Anderson, 1977).

By setting the carrier lifetime due to trap recombination, the constant in the expression for the mean carrier lifetime is determined. From Eq. 69 and Eq. 72, the carrier lifetime is:

$$\begin{aligned}\frac{1}{\tau} &= \frac{1}{\tau_T} + \frac{1}{\tau_A} \\ &= \frac{1}{\tau_T} + \left(\frac{G^2}{\tau_T N^2}\right)^{1/3}\end{aligned} \tag{105}$$

To estimate the size of the active region, the intrinsic carrier concentration, mobility, and carrier lifetime due to traps are needed.

$In_{1-x}Ga_xAs$

Most applications using gallium arsenide-related compounds attempt to exploit the ability of these alloys to match the lattice constants of the substrate (often InP) to produce unstrained layered structures (Miller and Mullin, 1991). Lattice-matching occurs for x=0.47, so many of the material properties reported in the literature are limited to this composition. Here, this value of the mobility is assumed to represent the mobility at all alloy compositions. Olivia and Eastman (1980) studied the mobility of gallium arsenide as a function of dopant concentration and obtained the following relation valid at room temperature.

$$\begin{aligned}\mu_{GaAs} &= \frac{1}{1+\sqrt{\frac{N_D + N_A}{10^{23}}}} \ \frac{m^2}{V\,s} \\ \mu_{InGaAs} &= 1.5\mu_{GaAs}\end{aligned} \tag{106}$$

where dopant concentration, N_D and N_A, are in m^{-3}. The mobility of holes is assumed to be 0.01 times that of the electrons.

Ahrenkiel et al. (1995) present measurements for the recombination lifetime in $In_{1-x}Ga_xAs$. Their results show that the bulk recombination lifetime (Shockley-Read-Hall lifetime) is very high due to the high quality of their samples. They report an observed value of 2.9 μs, which is used herein for the trap recombination lifetime. This parameter is the most difficult to model since it depends on the dominant mechanism of recombination and the quality of the fabrication of the devices (Green, 1982; Pierret, 1987). Rather than try to estimate a parameter that may vary to such a great extent, a single lifetime is adopted so as to give a reasonable result without obscuring the influence of the other parameters. A closer examination of the influence of carrier lifetime on the overall efficiency is examined in the Section 6.3.

$Hg_{1-x}Cd_xTe$

Carrier mobility for $Hg_{1-x}Cd_xTe$ is evaluated by generating a relation to fit the available Hall mobility data. Rogalski (1988) gives an expression that approximates the data for $0.2<x<0.6$ is:

$$\mu = \frac{9\times10^4 b}{Z^{2a}} \quad \text{with} \quad \begin{aligned} b &= (0.2/x)^{7.5} \\ a &= (0.2/x)^{0.6} \end{aligned} \tag{107}$$

where mobility has units of $m^2\ V^{-1}\ s^{-1}$ and Z is defined as:

$$\begin{aligned} &\text{for } T > 50\text{ K} \quad Z = T \\ &\text{for } T \le 50\text{ K} \quad Z = 1.18\times10^5 \Big/ \left[2600 - (T-25)^{2.07}\right] \end{aligned} \tag{108}$$

The hole mobility may be estimated at 0.01 times the electron mobility. For p-type materials, the mobility is expected to be reduced by a factor of approximately three (Rogalski, 1988).

Rogalski (1987) reports a carrier lifetime due to trap recombination of 0.1 μs and herein is assumed constant with temperature. Like the $In_{1-x}Ga_xAs$ materials, this lifetime

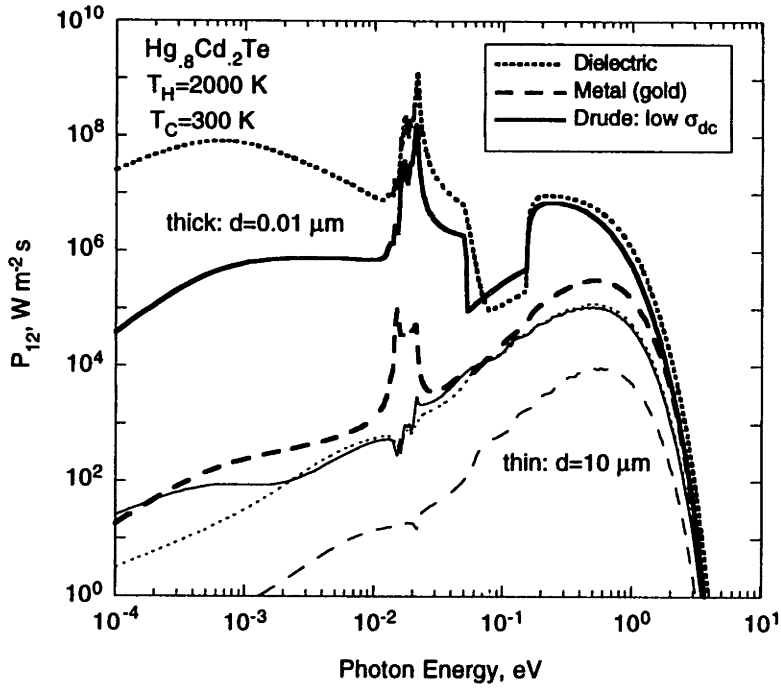

Figure 30: Comparison of the influence of dc conductivity on the spectrum of energy at small and large vacuum gap.

is used as an input parameter whose effect on the device performance is examined in Section 6.3.

6.1.3 Emitter Optical Constants

This study is focused on determining the effect of microscale radiative transfer on the performance of thermophotovoltaic devices. As a result, it is necessary to extract the effect of material properties of the emitter from those of the receiver. The emitters currently being examined in the literature vary in material from amorphous silicon carbide to the rare-earth oxides, which permit selective emission in particular frequency ranges.

An attempt was made in the present study to establish the effect of dc conductivity by modeling the emitter as a metal with the simplified form of the Drude model for the optical constants. The emitter conductivity can have a prominent effect on the spectral distribution of incident photon energy as shown in Fig. 30. For highly conductive

materials such as gold, the reflectivity is so high that the net flux at large spacing becomes low and then net power out of the device is lower than for a dielectric. For sufficient power output, a material with low conductivity is needed, i.e. a dielectric. Figure 30 shows that at small spacing, an emitter with a dielectric surface encourages an enhanced energy distribution at low energy, meaning that efficiency of the device will be low. Clearly a trade-off must be made between high conductivity for attenuation of low-energy photon flux at small vacuum gaps and low conductivity for sufficient power output.

The main focus of this study is the design of the device from the viewpoint of the receiver. To reduce the effect of the emitter optical constants, the emitter is modeled as a Drude material with a low conductivity. Figure 30 shows that such a model produces a spectrum of energy that approaches the dielectric results at both small and large vacuum gap, because, unlike the Hagen relation used for the metal optical constants, the full Drude expression produces a non-zero permittivity at photon energies near the band-gap. This model, with a low conductivity, ensures a black body-like behavior since it provides a weakly absorbing response to the incident radiation thereby keeping the reflectivity low and the magnitude of the permittivity is close to unity. This model will be used in all subsequent calculations for the emitter permittivity.

6.2 Modeling Receiver Device Parameters

The quantum efficiency and the dark saturation current of the thermophotovoltaic cells are the two device characteristics that are strongly dependent on the material properties introduced in the previous session (carrier mobility and lifetimes) (Borrego et al.; 1995). In turn, these properties influence the device performance. This section presents the models that can predict these parameters.

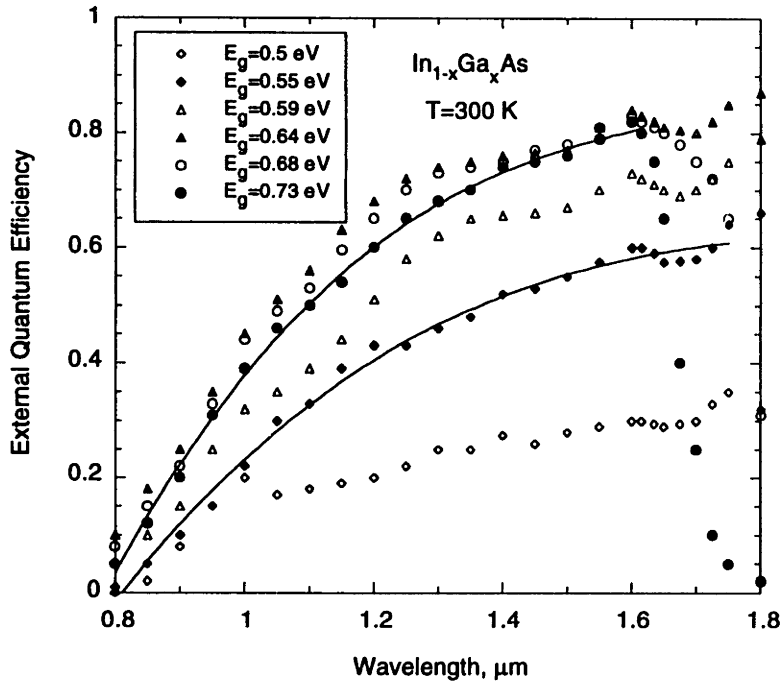

Figure 31: Quantum efficiency for $In_{1-x}Ga_xAs$ at 300 K; showing the curve fits for x=0.5 and x=0.7 for the measurements from Wojtczuk et al. (1995).

6.2.1 Quantum Efficiency

The quantum efficiency accounts for the fractional amount of minority carriers that, while generated by photon absorption, do not contribute to the light-generated current due to recombination or tunneling effects. This parameter depends greatly on the manner in which a particular cell is fabricated, but the general effect is demonstrated by the measurements of Wojtczuk et al. (1995). Figure 31 shows their data for $In_{1-x}Ga_xAs$ with the curve fit model used in this study. The curve fit is a third order polynomial:

$$Q_e = a_1 + a_2\lambda + a_3\lambda^2 + a_4\lambda^3 \tag{109}$$

where λ is in μm. The quantum efficiency is very low outside the wavelength range shown in Fig. 31; it is assumed to be zero outside the range: 0.8 μm < λ < λ_g. For the calculation of the photon flux, only the portion of the spectrum for which the quantum efficiency is greater than zero, is used.

Coefficient	A_i	B_i	C_i	D_i
a_1	198.9	-945.5	1454	-733.0
a_2	-533.3	2539	-3932	2004
a_3	421.1	-2007	3129	-1607
a_4	-103.4	492.6	-770.4	397.7

Table 5: Coefficients for the polynomial curve-fit of Eq. 110 to measurements of quantum efficiency in Fig. 31.

Another curve fit was used to express the empirical x-dependence of each coefficient:

$$a_i = A_i + B_i x + C_i x^2 + D_i x^3 \tag{110}$$

The values of A_i, B_i, C_i, and D_i determined by a computer fit are shown in Table 5.

For mercury cadmium telluride, a quantum efficiency of unity is assumed for photon energies above the band-gap energy and zero below. This assumption is made since thermophotovoltaic devices are not made from this material. In addition, $Hg_{1-x}Cd_xTe$ is used here to study ideal performance, and thus this model for quantum efficiency provides an upper bound to the performance characteristics.

6.2.2 Saturation Current

The saturation current is the reverse current that results when the photo-diode is dark and has no voltage bias; it is the pre-exponential factor for the expression of the dark current (Green, 1982). When in the dark, the minority carriers move by diffusion through the depletion region of the diode. Accounting for the current of electrons and holes produces the ideal diode law, and thus the saturation current (Green, 1982):

$$I_d = \frac{eD_e n_i^2}{L_e N_A} + \frac{eD_h n_i^2}{L_h N_D} = en_i^2 \left(\frac{\sqrt{D_e}}{N_A \sqrt{\tau_e}} + \frac{\sqrt{D_h}}{N_D \sqrt{\tau_h}} \right) \tag{111}$$

Using the parameters in the previous section and Eq. 62 for the diffusion length, the saturation current as a function of the material's band-gap energy can be determined.

To predict the saturation current, the intrinsic carrier concentration, n_i, is needed. For $In_{1-x}Ga_xAs$ the intrinsic carrier concentration can be calculated by using the scaling relation described by Jain et al. (1995). A curve fit to the data reported by Jain et al. (1996) yields the carrier concentration as a function of band gap energy for $In_{1-x}Ga_xAs$ at 300 K.

$$n_i = 1.86 \times 10^{24} \exp\left(-19.1\, E_g\right) \text{m}^{-3} \tag{112}$$

For $Hg_{1-x}Cd_xTe$, Hansen and Schmit (1983) model the intrinsic carrier concentration with a relation for the band gap using the most recently available fundamental parameters. Their approximate expression for the intrinsic carrier concentration (in units of m^{-3}) is:

$$n_i = \left(5.585 - 3.820x + 1.753 \times 10^{-3} T - 1.364 \times 10^{-3} xT\right) \times 10^{20} E_g^{3/4} T^{3/2} \exp\left(-E_g / 2k_b T\right) \tag{113}$$

The saturation current determined for a device made of $In_{1-x}Ga_xAs$ is shown in Fig. 32 along with measurements of actual dark current by Wilt et al. (1995) and Wojtczuk et al. (1995). The broken line indicates the prediction using Eq. 111 with the intrinsic carrier concentration from Eq. 112. The result under-estimates the dark current measured on actual devices by a factor of several orders of magnitude. To obtain realistic performance estimates, the saturation current is fitted to the measured data by adjusting the intrinsic carrier concentration by a factor of 11.32.

Choosing to adjust the carrier concentration is reasonable, since it depends of the quality of the actual diode. In addition, the dark current depends on the second power of the carrier concentration and only weakly on the carrier lifetime and diffusion coefficient. Because the intrinsic carrier concentration enters the model of the device performance

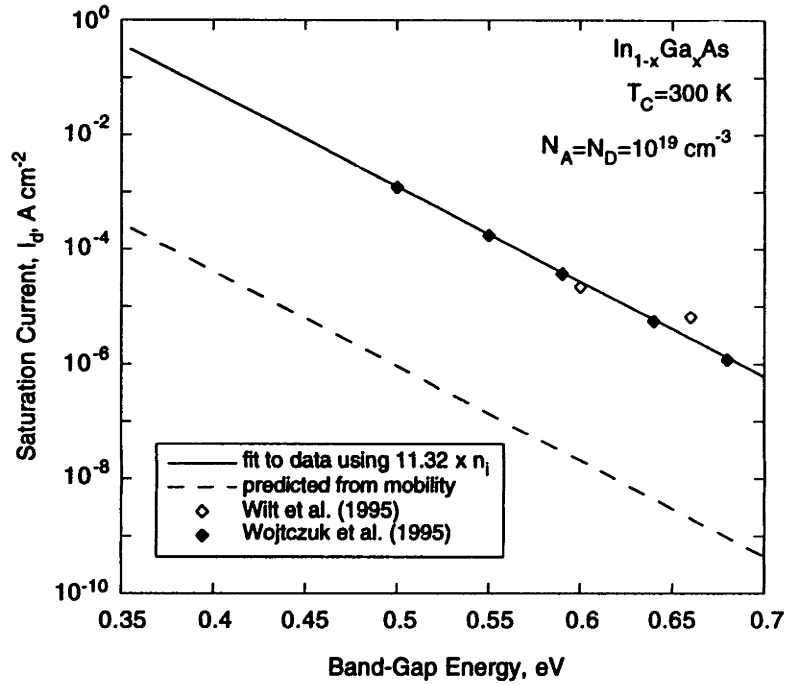

Figure 32: The saturation current for a pn-junction made from heavily-doped $In_{1-x}Ga_xAs$.

only through the dark current whereas the mobility and carrier lifetime affect the active region of the diode, its choice as an adjustable parameters is justified further. For this reason, the intrinsic carrier concentration is fixed to fit the dark current while the mobility and carrier lifetime become design parameters to examine the performance of the device.

The saturation current determined for a device made of $Hg_{1-x}Cd_xTe$ is shown in Fig. 33. Reine et al. (1981) report measurements of the R_0A product which accounts for all the current losses in a diode, including surface recombination, tunneling, and contact resistance. From this product, the overall current losses can be estimated:

$$R_0A = \frac{k_bT}{e^2}\frac{\tau}{nL} = \frac{k_bT}{e}\Big/ I_d \tag{114}$$

where n is the minority carrier concentration ($=n_i^2/N_D$). At low temperature, the prediction and measurements agree, but at higher temperature the intrinsic carrier concentration must be increased. For $Hg_{1-x}Cd_xTe$, the value is 36.5. Note that the

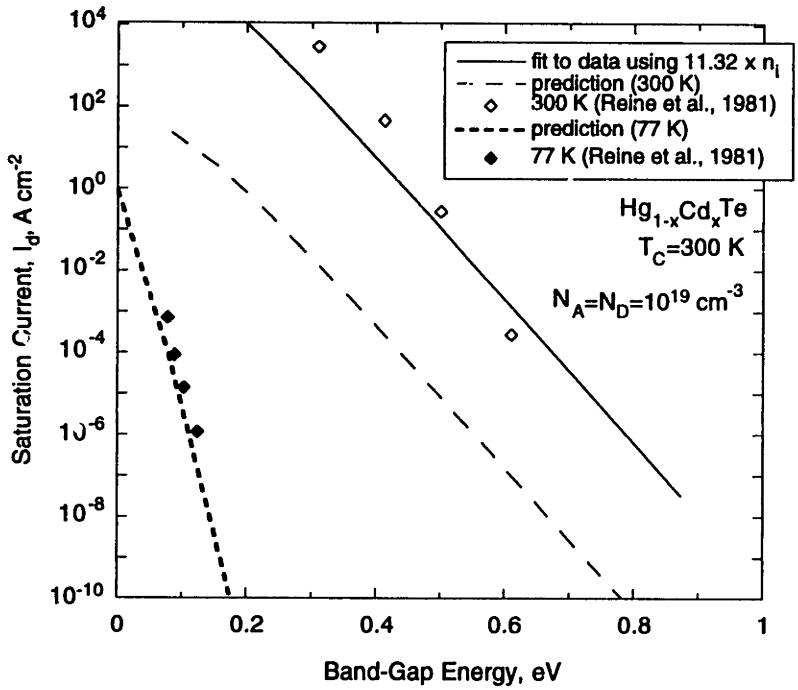

Figure 33: The saturation current for a pn-junction made from heavily-doped $Hg_{1-x}Cd_xTe$.

$Hg_{1-x}Cd_xTe$ has a higher dark current than $In_{1-x}Ga_xAs$ at 300 K. This will limit the performance of these devices, but it may be offset by their lower band-gap energy.

6.3 Enhanced Performance Due to the Spacing Effect

6.3.1 Performance at Large Vacuum Gap

The performance of the proposed thermophotovoltaic devices is determined from a numerical integration of the photon flux in the vacuum gap over all frequencies (Eq. 78). For details of the numerical integration, see Appendix A. The photon flux determines the magnitude of the short-circuit current generated in the device, which in turn determines the voltage and thus the power. Figure 34 shows the variation of the device output for a diode fabricated from $In_{1-x}Ga_xAs$ with various alloy compositions. The source has a temperature of 2000 K and the vacuum gap is large. Figure 35 shows the result for a $Hg_{1-x}Cd_xTe$ under the same conditions. The output power density is representative of

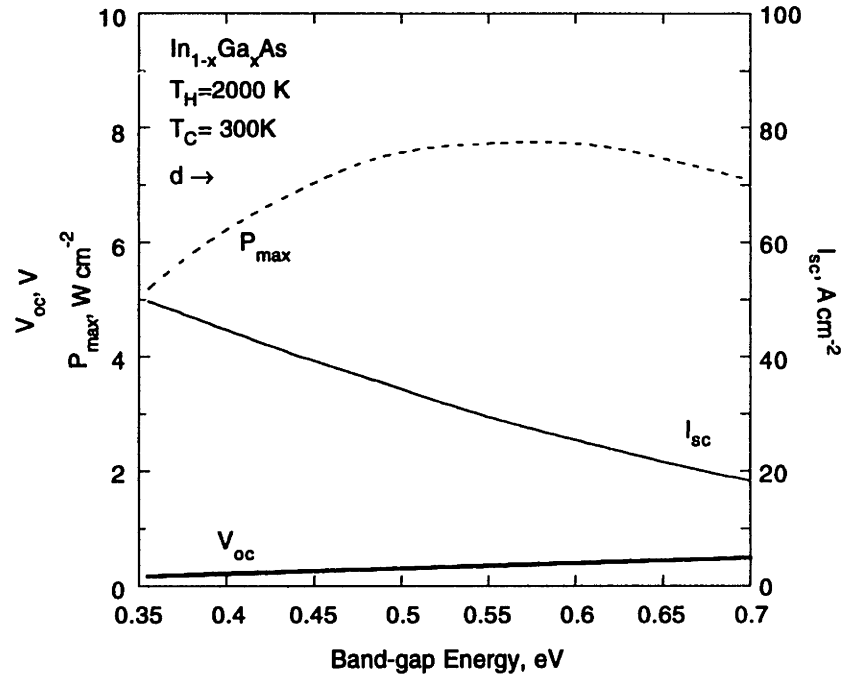

Figure 34: Current, voltage, and maximum power output at large vacuum gap of a pn-junction made from heavily-doped $In_{1-x}Ga_xAs$.

those actually achievable. Krist (1995) reports values of 1.5-3 W/cm^2 in their device, which operates with a source at 1700 K. Given the difference in emitter temperature, the prediction is quite close to actual system performance.

The results indicate that there is an alloy composition at which the power output reaches a maximum. This arises from the behavior of the saturation current, which decreases with band-gap energy as shown in Fig. 32 (Green, 1882). A decrease in saturation current causes the voltage to increase with band-gap energy. The short-circuit current, however, exhibits the opposite trend: it decreases with band gap, since less of the incident power can be absorbed owing to a shift in the absorption edge. This result is typical of the performance of solar cells, for which a maximum power output occurs at a band gap in the range of 1.4 to 1.6 eV (Green, 1982). Figures 34 and 35 indicate that the peak power occurs for a band-gap energy near 0.6 eV for $In_{1-x}Ga_xAs$ and about 0.64 eV for $Hg_{1-x}Cd_xTe$.

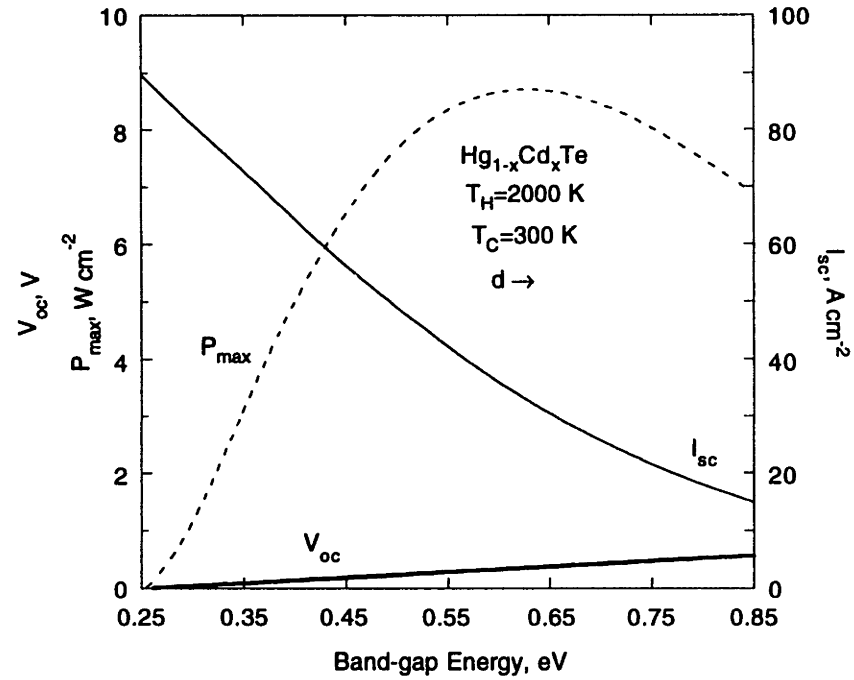

Figure 35: Current, voltage, and maximum power output at large vacuum gap of a pn-junction made from heavily-doped $Hg_{1-x}Cd_xTe$.

The net power is nearly the same for the two materials despite the higher dark current of $Hg_{1-x}Cd_xTe$. The results show that the short circuit current for $Hg_{1-x}Cd_xTe$ is about 1.2 times greater than that of $In_{1-x}Ga_xAs$. This arises from the difference in the magnitude of the permittivity at high photon energy. The magnitude of the permittivity of $In_{1-x}Ga_xAs$ remains constant at about 11 above the band gap (see Fig. 26), where as for $Hg_{1-x}Cd_xTe$ it is about 8, for a ratio of 1.4. At large spacing the fluctuational electrodynamics approach produces a net flux inversely proportional to the magnitude of the permittivity. For the device performance, this means that the $Hg_{1-x}Cd_xTe$ devices produce slightly more power.

6.3.2 Influence of Temperature

As the temperature of the emitter is increased, more current is generated producing more power output. Figure 36 indicates the effect of increasing the emitter temperature

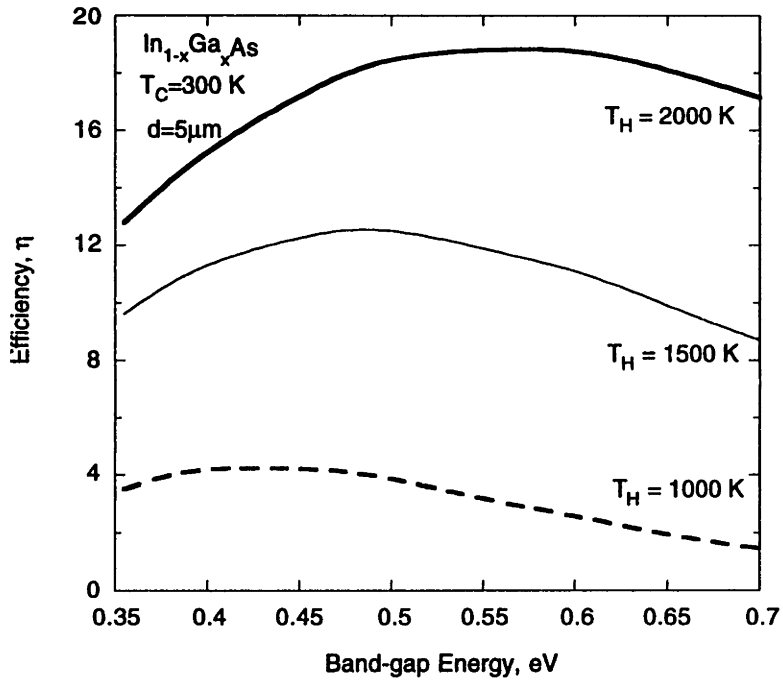

Figure 36: Variation in efficiency due to temperature of the emitter for an $In_{1-x}Ga_xAs$ device.

on the efficiency of the device. In the thermophotovoltaic literature, the efficiency is defined as the output power over the total incident power above the band-gap energy. Here, the efficiency is the power output over the total power of the entire spectrum, thus staying with the more traditional definition. An increase in emitter temperature to 2000 K from 1000 K produces an increase by a factor of almost 5. As indicated in Figure 21, the device becomes very inefficient at low emitter temperature where a substantial amount of the incident power is carried by photons of energy below the band-gap energy.

There is also a shift in the location of the maximum efficiency. As the temperature decreases, the net flux of photons also decreases, directly affecting the magnitude of the short-circuit current. The open-circuit voltage decreases more slowly with temperature, because it depends on the natural logarithm of the ratio of short-circuit current to dark current. Since the current decreases more quickly than the voltage, their relative

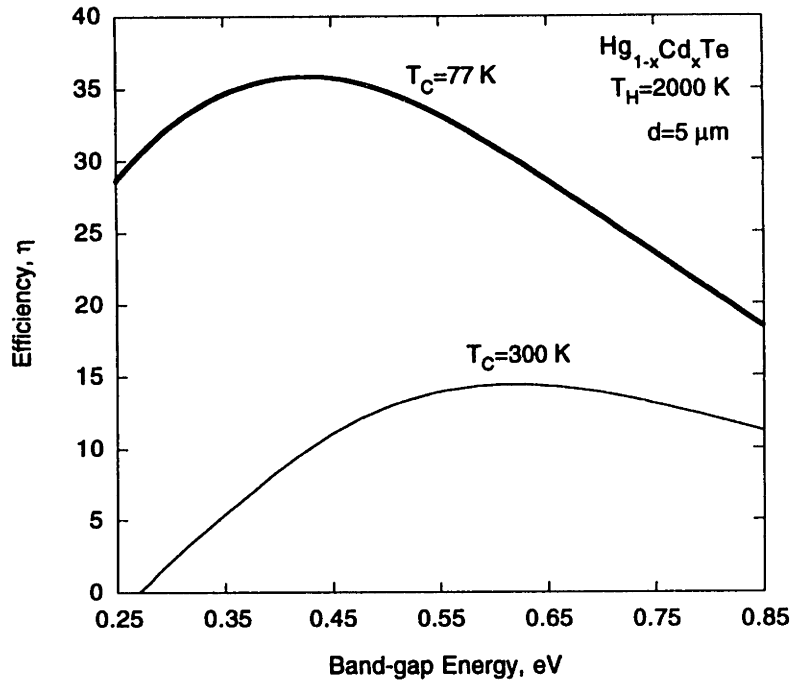

Figure 37: Variation in efficiency due to temperature of the receiver for a $Hg_{1-x}Cd_xTe$.

magnitude decreases, resulting in a shift of the maximum efficiency to lower energy at lower emitter temperatures.

It is worthwhile to determine the effect of lowering the temperature of the receiver, since the dark current can be substantially reduced. (Infrared detectors made from $Hg_{1-x}Cd_xTe$ normally operate at low temperature to decrease the noise for improved detector response (Reine et al., 1981).) Figure 37 shows the effect of alloy composition on the efficiency for a $Hg_{1-x}Cd_xTe$ diode cooled to 77 K with a source at 2000 K. The decreased dark current provides a substantial improvement in the performance by more than doubling the maximum efficiency. This increase occurs because of the large decrease of dark current despite a decrease in the thermal voltage, which tends to lower the voltage generated.

The maximum efficiency shifts to lower band gaps because a lower dark current increases the voltage relative to the current. The optical constants near band gap,

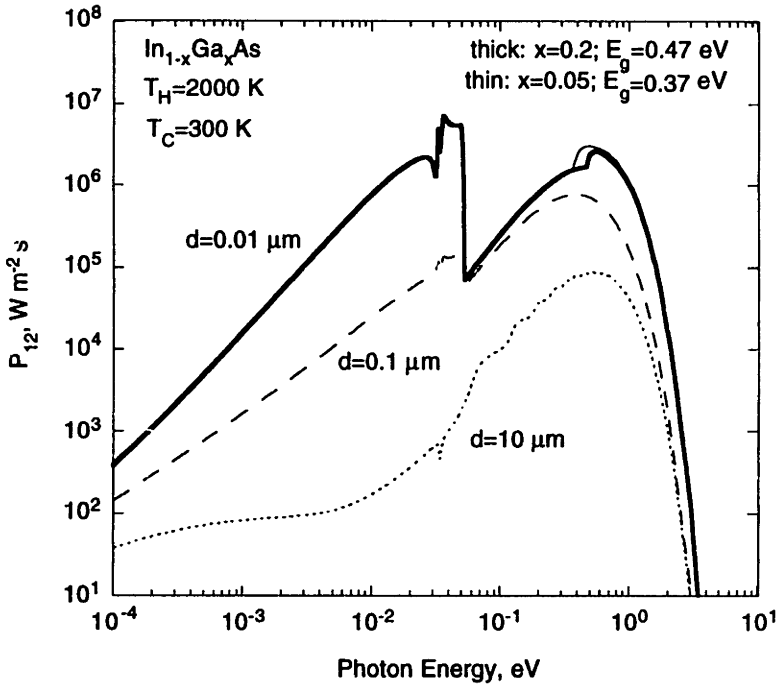

Figure 38: Spectrum of energy flux from the emitter to the receiver at various vacuum gaps for an $In_{1-x}Ga_xAs$ device.

however, are relatively insensitive to the temperature, meaning that the photons absorbed, and thus the current generated, remain approximately unaffected by the cooler receiver. For terrestrial systems, the cooling costs incurred for maintaining the receiver temperature may prove prohibitive. For space-borne applications, however, where cooling may not prove a problem, a lower receiver temperature may prove beneficial since the potential for improved efficiency is large.

6.3.3 Influence of Vacuum Gap on Energy Density

As the vacuum gap between the receiver and emitter becomes small, the effects of the near field become important for determining the photon flux. As discussed in Chapter 3, this enhanced flux varies significantly from the result of Planck's distribution for the energy density in a cavity at thermodynamic equilibrium. The results of a numerical prediction of the uni-directional energy flux (from the emitter to the $In_{1-x}Ga_xAs$ receiver) for a vacuum gap of 0.01 μm and 0.1 μm is shown in Fig. 38.

Figure 30 shows the results of a similar computation for $Hg_{1-x}Cd_xTe$. These figures also include the result for a large vacuum gap, where only the traveling waves contribute to the energy flux.

The flux of energy from the emitter to the receiver increases over the entire energy range at a sufficiently small vacuum gap. (The details of the energy spectrum at intermediate vacuum gaps is discussed in the last sub-section of Section 6.3.) Note the decrease in the energy distribution for photons of energy less than the band gap. This decrease is a result of the extinction coefficient being nearly zero over a significant range of energy below the band gap. The power density increases again as phonon- and free-carrier absorption begins to dominate at low energy. Such absorption decreases the efficiency since the energy is insufficient to create an minority carriers, and therefore, the energy is absorbed without contributing to the current.

It is instructive to examine the ratio of power in the spectrum above the band-gap, to the total incident power incident on the diode. Figure 39 shows this ratio as a function of vacuum gap for several alloy compositions. For the $In_{1-x}Ga_xAs$ device, the ratio of power above the gap decreases initially, before returning to its large spacing value. As the vacuum gap decreases, fewer traveling waves of the far field can fit within the space between the emitter and receiver. A decrease in power across the spectrum results, but the first part of the spectrum to tunnel across the vacuum gap is the low energy portion since the wavelength is longest in the region. As a result, the fraction of energy above the band gap will decrease initially until the far-field effect compensates. For $In_{1-x}Ga_xAs$, the ratio does not increase above its value at large gaps, because the band-gap energy is not sufficiently below the peak in the spectrum for an emitter at 2000 K (0.85 eV).

The $Hg_{1-x}Cd_xTe$ receivers have a much higher fraction of energy above the band gap, and exhibit a substantial increase with spacing. For band-gaps sufficiently below the peak in the spectrum, almost the entire incident power is at high photon energy. As the

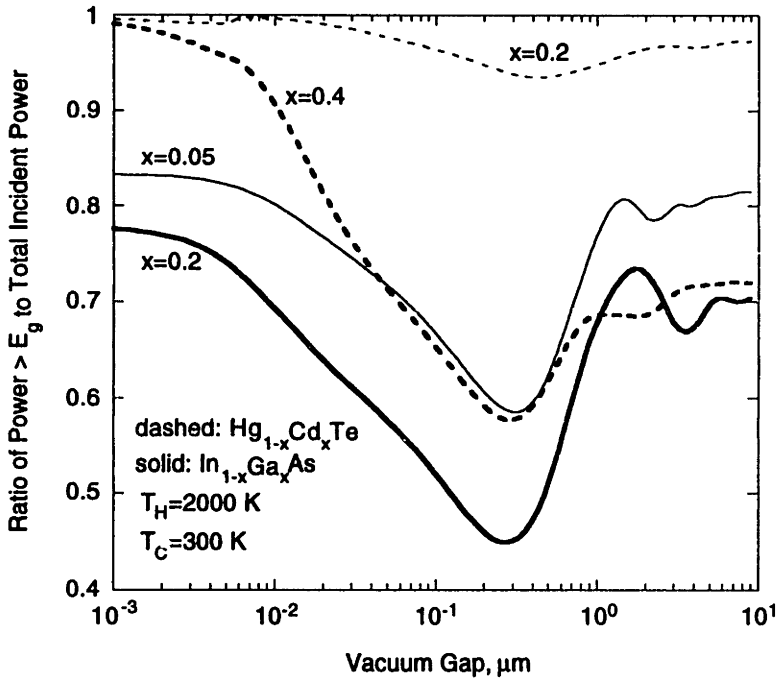

Figure 39: The fraction of the incident energy flux from the emitter that is above the band-gap of the receiver.

alloy composition changes toward higher x, the band gap increases, resulting in less energy flux above the band gap. At such alloy compositions, however, the greatest increase in the fraction of energy occurs, since as shown in Fig. 30, the near field increases the power over a significant energy range in the vicinity of the peak, while attenuating the low energy region of the spectrum.

Though the fraction of the power spectrum above the band gap is an important parameter for the determination of the device performance, it does not capture the details of the energy conversion process. Consider the power output of the device as calculated from Eq. 59. Figure 40 shows the incident flux of energy and the net power out of the device as a function of vacuum gap, with their ratio: the efficiency of the device.

Note the substantial increase in output as the vacuum gap diminishes. Over the first decade for which the near-field enhances the energy flux, there is an order of magnitude increase in the power incident on the device. The power output tracks the incident power

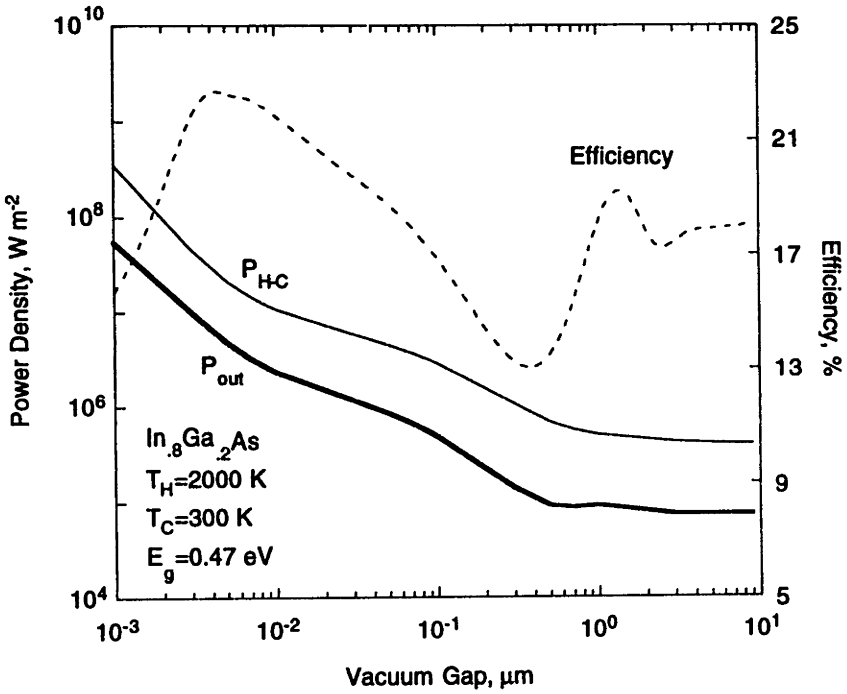

Figure 40: Output power and efficiency as a function of vacuum gap for $In_{1-x}Ga_xAs$ at low band gap.

as expected resulting in a higher power output from the device, but a lag occurs resulting in decreased efficiency in the sub-micron region. The microscale device is able to process a higher through-put of energy, from the emitter, but it does so at a slight decrease in efficiency, due to the initial near-field enhancement of the low energy portion of the spectrum. This is shown clearly in Fig 40, by the flat portion of P_{out} near 1 μm, whereas $P_{H\text{-}C}$ continues to increase. Similar results occur for the $Hg_{1-x}Cd_xTe$ devices, the results of which are shown in Fig. 41.

For gap sizes less than 0.3 μm, the power output tends to approach the incident power, and so the efficiency tends to increase greatly. This increase does not, and cannot, continue indefinitely. Below 10^{-2} μm, the increase in power output tends to slacken and the efficiency again drops. The enhanced photon absorption is responsible for the increase in recombination that occurs when the generation rate of electrons and holes is high. The increased recombination is discussed in 6.3.3 where the influence of carrier lifetime is examined.

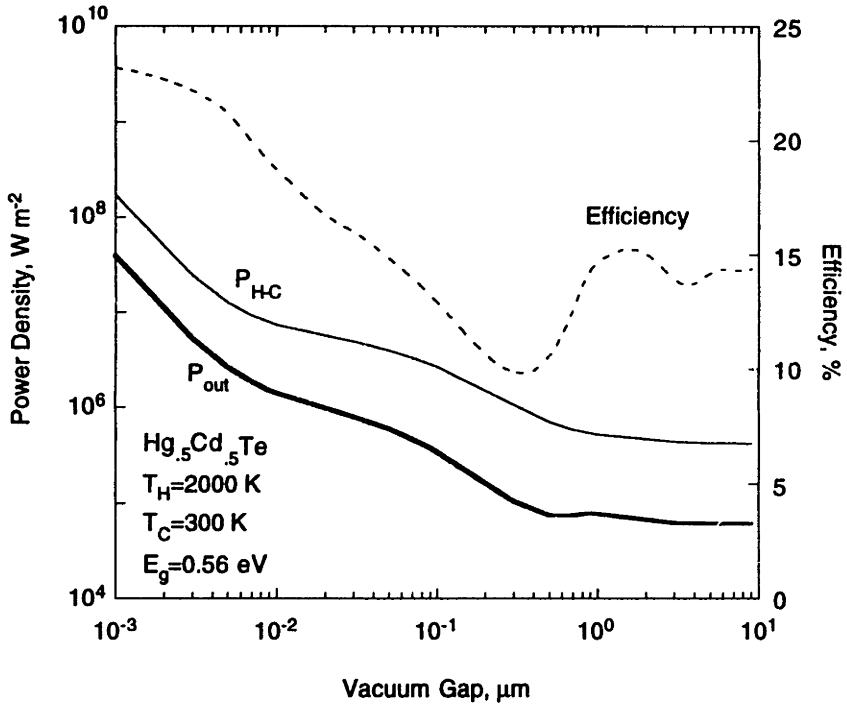

Figure 41: Output power and efficiency as a function of vacuum gap for $Hg_{1-x}Cd_xTe$ at low band gap.

6.3.4 Influence of Band Gap on Efficiency

Figures 42 and 43 show the efficiency as a function of vacuum gap for several values of the band gap. While the trends are very similar, the alloy composition plays an important role in determining the depth of the minimum and the height of the maximum. Only for very low band gap does the minimum in efficiency disappear. For all other band gaps, the increase in efficiency occurs only after the minimum at a larger gap. Figure 43 shows clearly that as the band-gap is increased, the minimum starts to appear, and the maximum decreases.

To get a better sense of the influence of band-gap energy on the performance, consider the efficiency as a function of band-gap energy as shown in Figure 44 and 45 for several vacuum gap sizes. The variation in efficiency with band-gap energy displays the characteristic maximum at intermediate values of the band-gap. As the vacuum gap size decreases, the entire curve shifts to lower total efficiency. As the gap is decreased further, the efficiency begins to increase, growing to a value greater than that at large gap.

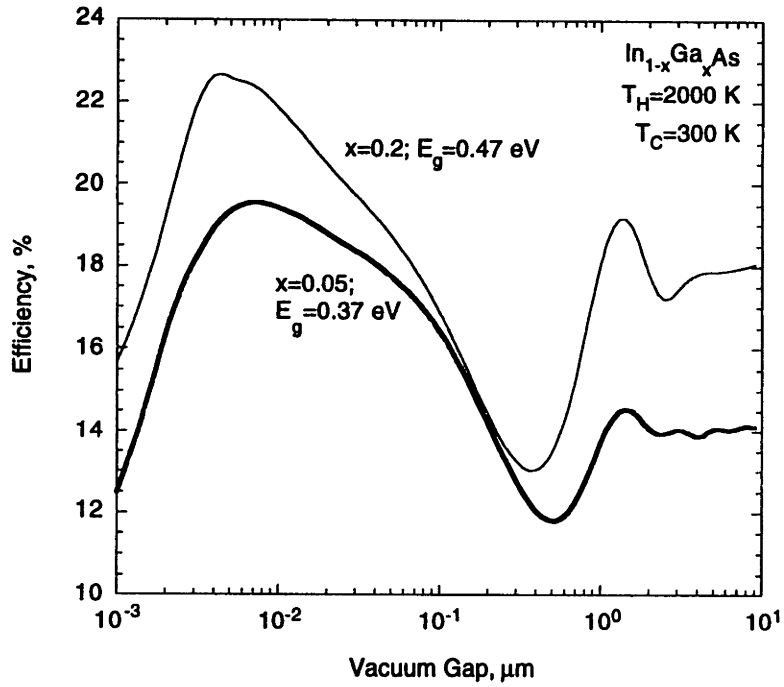

Figure 42: Efficiency as a function of vacuum gap for $In_{1-x}Ga_xAs$ at several alloy compositions.

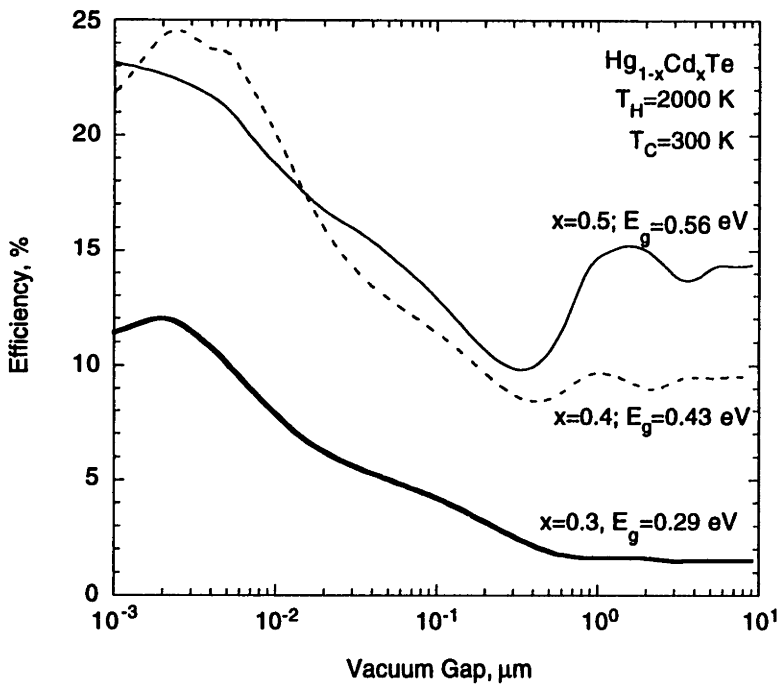

Figure 43: Efficiency as a function of vacuum gap for $Hg_{1-x}Cd_xTe$ at several alloy compositions.

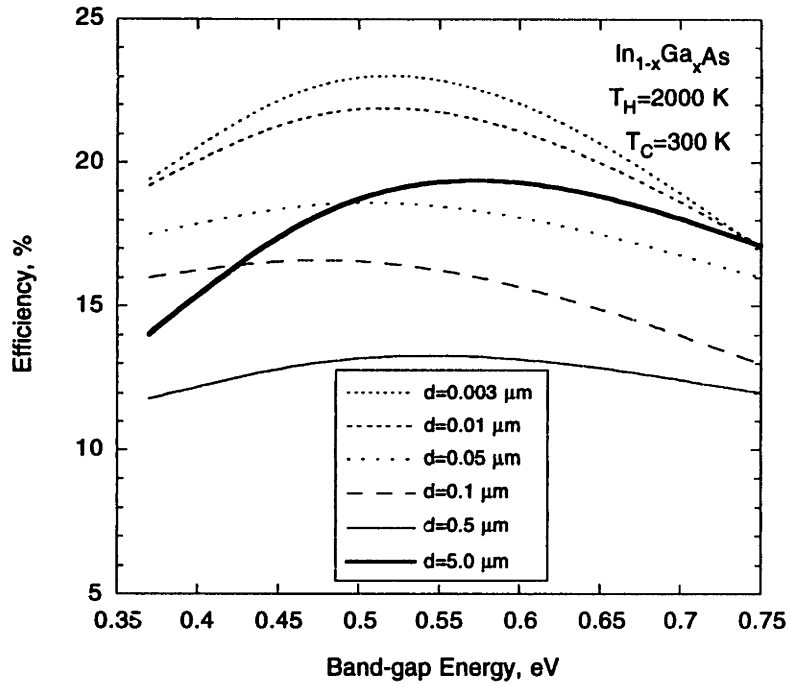

Figure 44: Efficiency versus band-gap energy for $In_{1-x}Ga_xAs$ at several vacuum gaps.

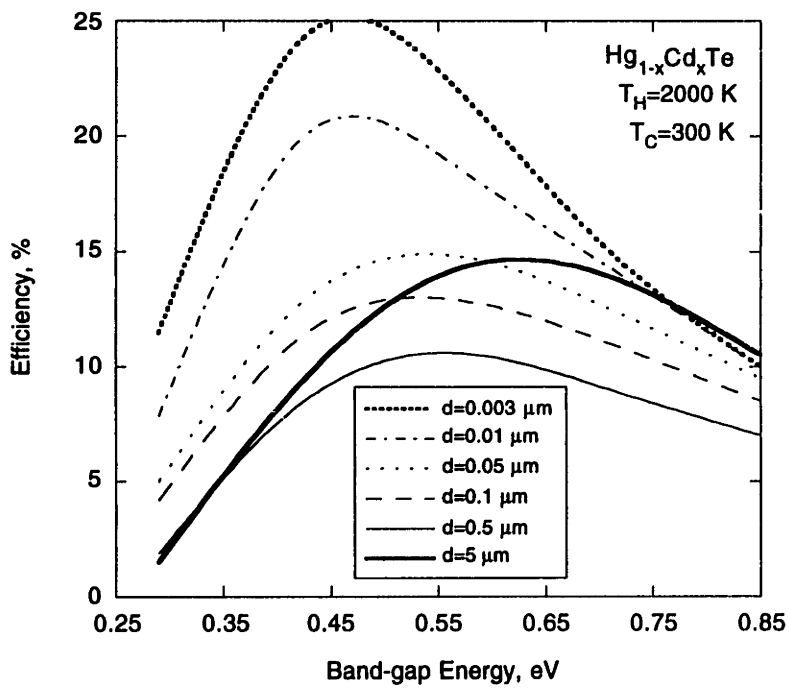

Figure 45: Efficiency versus band-gap energy for $Hg_{1-x}Cd_xTe$ at several vacuum gaps.

The efficiency does not simply increase equally over all band gaps. Two characteristics are apparent in the numerical predictions. The maximum efficiency occurs at lower band-gap energy, and there are alloy compositions for which the spacing effect cannot improve the efficiency at all. The shift in the maximum is due to the tendency of the cannot improve the efficiency. The shift in the maximum is due to the tendency of the spacing effect to enhance the low-energy radiation. The spacing effect, therefore, will alter the current density most noticeably in the low band-gap material. This effect is most strongly evident in $Hg_{1-x}Cd_xTe$.

The results of the computation suggest that the spacing effect may only be useful in increasing the efficiency for a range of alloy compositions. This range is for band gaps below the location of the maximum at large spacing and the upper limit of which increases with decreasing vacuum gap. This upper limit is the point at which the thin curves intersect the bold solid curve. The higher the band-gap energy, the smaller the vacuum gap needed to bring the efficiency to a value equal to its large spacing value. Careful consideration of the alloy composition and spacing can lead to both increased power density with improved efficiency.

6.3.5 Influence of Carrier Lifetime and Doping

These predictions seem to imply that the efficiency will continue to increase as the vacuum gap decreases. While this is true for the net heat flux, the same cannot be said for the power output since recombination plays an important role in limiting the maximum efficiency that can be obtained.

The increased power produced in a microscale thermophotovoltaic device results from the enhanced flux of photons as the vacuum gaps decreases. Both the light-induced current and voltage will increase until the concentration of carriers is so large that recombination attenuates the power output. The model used for the microscale device presented in Chapter 5 includes the effects of Auger recombination. Recall Eq. 72, which

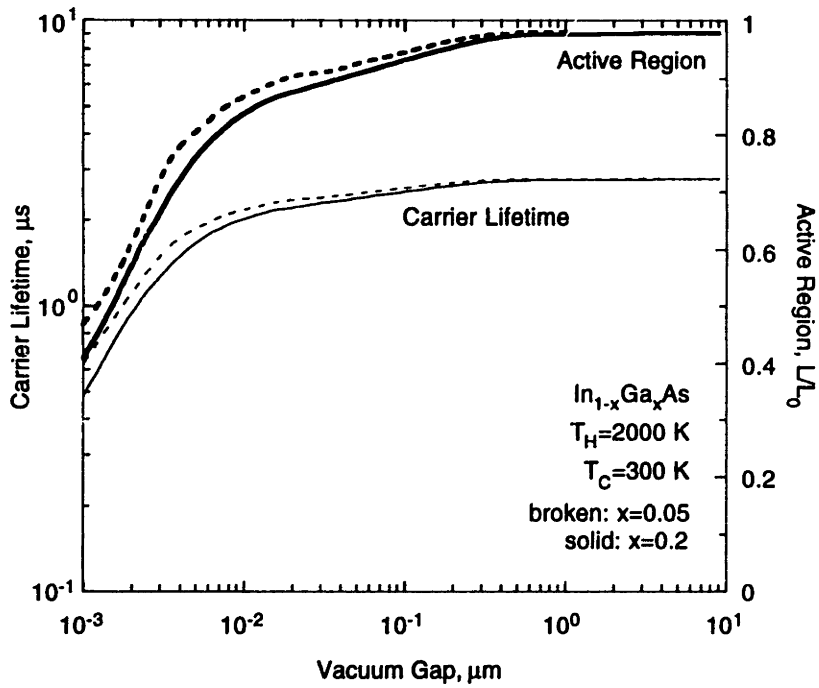

Figure 46: Carrier lifetime and the active region for $In_{1-x}Ga_xAs$.

gives an expression used to account for this recombination mechanism. The carrier lifetime will decrease due to the enhance generation of carriers. As Auger recombination increases, it will dominate the trap recombination (Eq. 66).

Figure 46 shows the carrier lifetime as a function vacuum gap in $In_{1-x}Ga_xAs$ and Figure 47 shows the values for $Hg_{1-x}Cd_xTe$. Note that the carrier lifetime at large spacing equals that of the lifetime due to trap recombination. As the emitter and receiver are brought close together, the near-field produces greater numbers of electrons and holes. These unpaired carries begin to recombine more quickly as their concentration grows. The result is a decrease in lifetime of the carriers. The carriers must diffuse to the junction interface in order to contribute to the current. Since their lifetime is shorter, and they move with the same diffusion coefficient, fewer carriers will survive long enough to reach the depletion region of the pn-junction cross through it and travel to the contacts. The light-generated current, therefore, is limited by recombination effects.

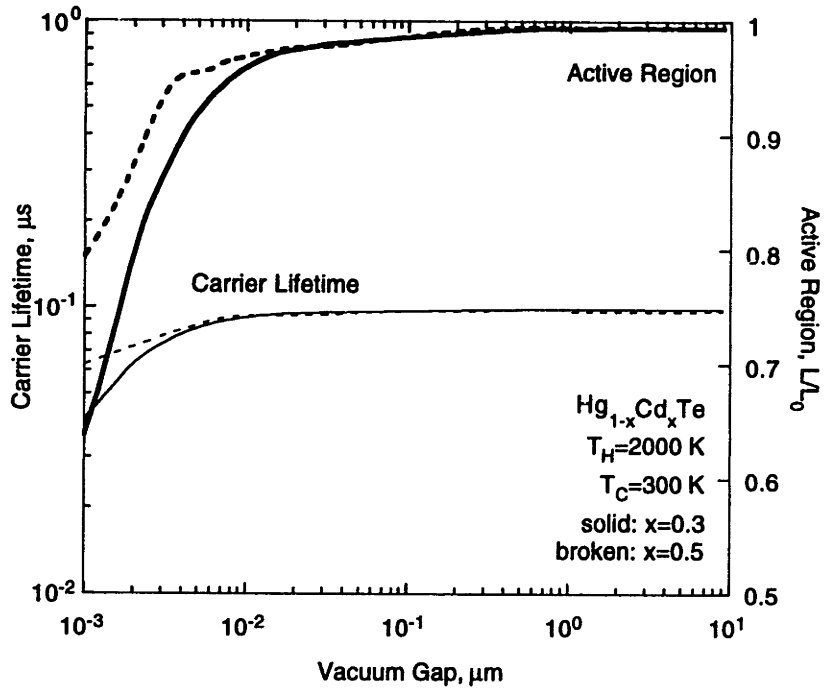

Figure 47: Carrier lifetime and the active region for $Hg_{1-x}Cd_xTe$.

This decreased lifetime manifests itself as a decreased in the effective active region of the cell. The active region is that part of the cell extending to a diffusion length on either side of the depletion width of the junction. From Eq. 62, these lengths are proportional to the square root of the carrier lifetime, and so decrease as shown in Fig. 46 and Fig. 47 with the carrier lifetime. This length is used to model the average concentration of photon-generated electrons and holes in the device by assuming a uniform generation rate at large spacing. As the gap decreases, the active region decreases, while the generation rate remains averaged over the initial (large-vacuum gap) active region. In this manner, the reduced carrier lifetime limits the performance.

Note that such active regions are quite large, especially for $In_{1-x}Ga_xAs$ which has a high mobility. These values are larger than typical thermophotovoltaic devices themselves, which are on the order of ten microns (Wilt et al. 1995). The active region reduces strongly once Auger recombination dominates the predictions of the carrier lifetime. Bringing the emitter close enough to the receiver will increase the photon flux

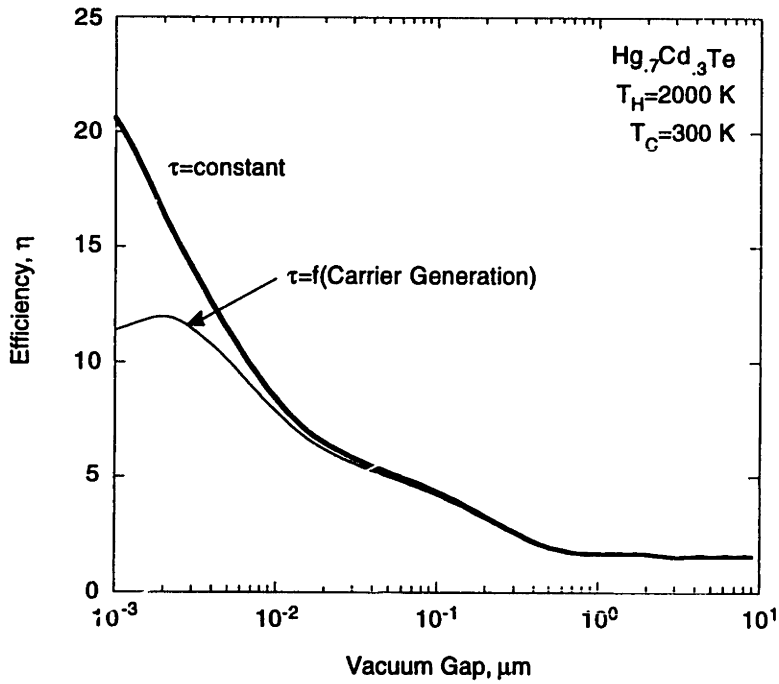

Figure 48: The effect of neglecting Auger recombination on the prediction of the increase in efficiency for $Hg_{1-x}Cd_xTe$.

so much that the active region will be smaller than the device size. Once this occurs, the active region will become so small that very little power can be obtained from the device.

Figure 48 indicates the effect of neglecting the Auger recombination on carrier lifetime: the efficiency apparently grows without bound. This result is due to the dependence of voltage on the short-circuit current. The short circuit current is related to a fraction of the incident power, but the voltage is proportional to the natural logarithm of the current. Near equilibrium conditions, this relation holds, since the minority carries are at a

small concentration. At very small vacuum gaps, the carrier concentrations become large, and the application of the standard equilibrium analyses such as the one used here to determine the microscale device performance will be in error.

The level of doping plays a crucial role in the performance of thermophotovoltaic devices. It is important to keep the doping as high as possible, so that the dark current is

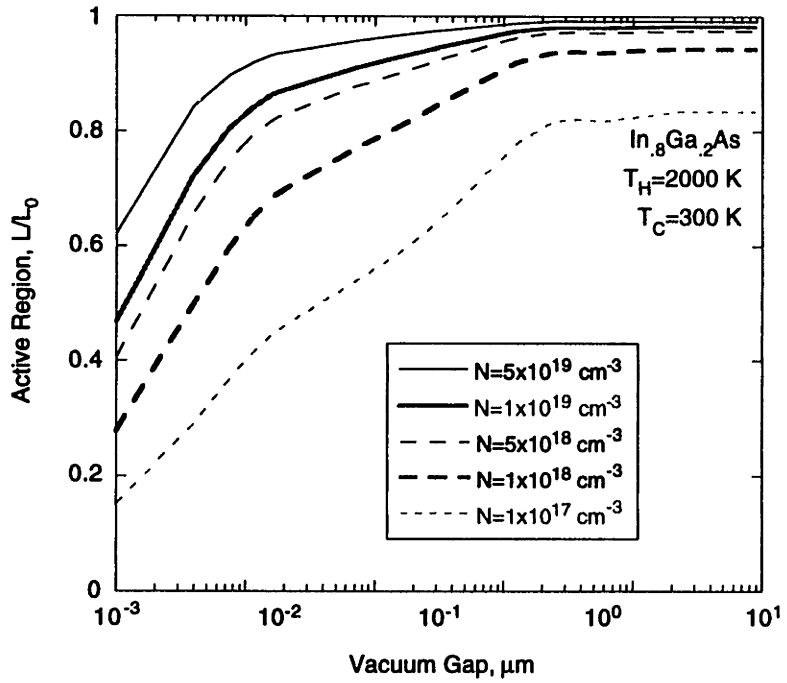

Figure 49: Influence of dopant concentration on active region for $In_{.8}Ga_{.2}As$.

minimized permitting a larger open-circuit voltage. The doping also affects the microscale performance by influencing the size of the active region. The model for the microscale device of Chapter 5 assumes that the carrier lifetime is proportional to the square of the carrier concentration. The trap portion of this lifetime is set by experimental measurements of carrier lifetime with doping levels. By setting the trap recombination lifetime, the constant of proportionality for the Auger recombination is determined. From Eq. 76, the ratio of active region is:

$$\frac{L}{L_0} = \left[1 + \left(\frac{\Phi_p \sqrt{\tau_T}}{\left(\sqrt{D_e} + \sqrt{D_h}\right) N_D}\right)^{2/3}\right]^{-1/2} = \left[1 + \left(\frac{\Phi_p \tau_r / L_e}{N_D}\right)^{2/3}\right]^{-1/2} \tag{115}$$

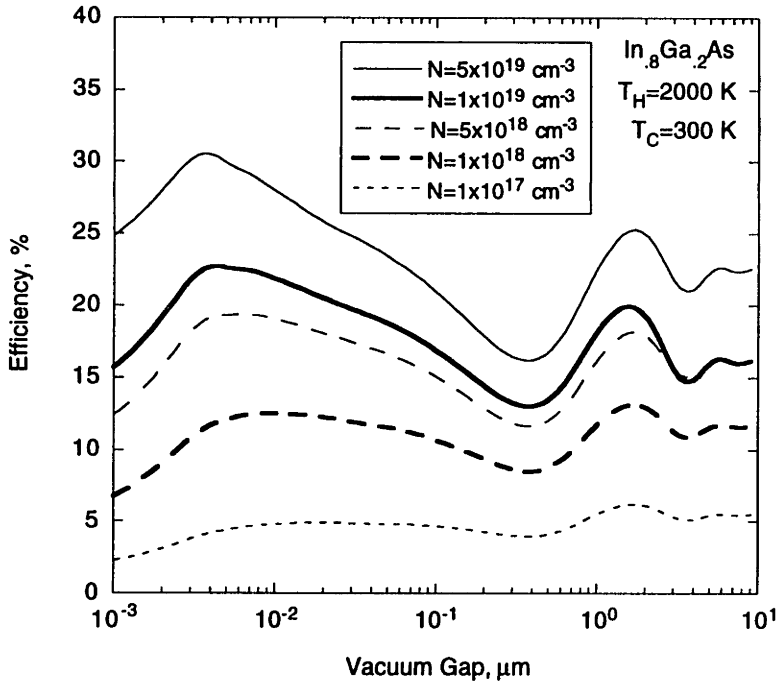

Figure 50: Influence of dopant concentration on efficiency for $In_{.8}Ga_{.2}As$.

The ratio involving the doping compares the concentration of light-generated carriers in the initial active region to the doping concentration. Figure 49 shows the influence of doping on the active region of $In_{.8}Ga_{.2}As$.

At high doping, the active region maintains its initial size over a substantial range of vacuum gaps. Increasing the doping from this level shifts the efficiency curve higher as depicted in Fig. 50. Decreasing the doping while keeping the trap recombination lifetime constant causes the Auger recombination to dominate even at large vacuum gaps. As a result, the active region does not approach unity at large vacuum gaps, since the active region over which the light-induced carrier concentration is averaged is greater than the actual active region. Low doping causes a substantial dark current, which produces low efficiency as indicated in Fig. 50.

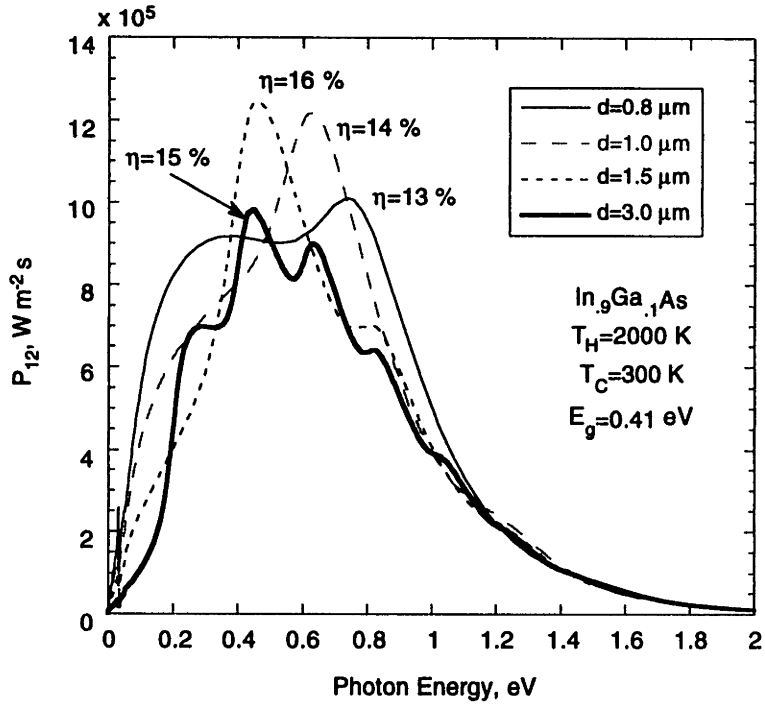

Figure 51: The uni-directional energy flux in the interference region of vacuum gaps for $In_{.9}Ga_{.1}As$.

6.3.6 Performance in the Interference Region

The previous sections have examined the performance of microscale thermophotovoltaic devices at small vacuum gaps where the near-field is the only contribution to the energy density in the gap. Figures 42 and 43 indicate that the efficiency oscillates around its large gap value until it reaches a minimum. This oscillation is due to wave interference caused by the small vacuum gap between the emitter and the receiver.

As the gap decreases, longer traveling waves cannot meet the boundary conditions, and so are excluded from the space between the surfaces. Figure 51 shows the effect of interference on the distribution of energy incident on the cell. At a large vacuum gap, there are an infinite number of traveling waves, and the spectrum is smooth as indicated by Fig. 38. For a gap of 3 μm, the spectrum is no longer smooth and the peaks and valleys that represent the effects of wave interference become evident. These peaks move

off to higher energy as the gap decreases until the final peak which represents the longest traveling wave (λ=2d) passes over the peak. As it does so, the spectrum of energy increases by a factor of almost 2. The minimum in efficiency comes after this peak has shifted to higher energy, because the near-field begins to enhance the low energy portion of the spectrum. By 0.8 μm, there is a substantial enhancement of the low energy portion of the spectrum. This shift in the energy distribution causes a decreased efficiency.

The wave interference effect may prove useful for operating a device at an improved efficiency level, while permitting a higher power output. The gap size of the device must be controlled carefully in order to maintain the peak in the appropriate location relative to the band-gap energy.

6.3.7 Heterojunctions: Influence of Multiple Band Gaps

Each photon with energy greater than the band gap creates a single electron-hole pair regardless of its energy. For high energy photons, the electron is elevated to energy levels greater than the conduction-band edge. (The hole is injected below the valence-band edge.) The electron and hole, however, quickly relax back to the band edge by recombination. Though the photon's energy may be much greater than the band gap, the electron and hole are separated only by the band-gap energy. This relaxation limits the achievable efficiency (Green, 1982).

The efficiency can be improved by the use of a heterojunction. By creating a layered structure in which each layer has a different band-gap, the power loss due to relaxation can be attenuated. High energy photons are absorbed near the surface of the receiver, and lower energy photons penetrate to a greater depth. By placing a high band gap material at the surface, electron-hole pairs formed from high energy photons will be subject to less thermalization. For the deeper layers, successively smaller band-gaps permit lower energy photons to be absorbed. These lower energy photons, however, cannot be absorbed by the top layer since its absorption below the band-gap is zero.

By prudent choice of layer thickness and band gap, the light-induced current can be maintained at a level equal to that of a homojunction. The performance improves, since the dark current associated with the recombination process will decrease, thereby, increasing the voltage output of the device.

For the purpose of analysis, consider a two-layered heterojunction fabricated from $In_{1-x}Ga_xAs$. The total current is the sum of the current generated within each layer. The expression for the generation rate must be modified to account for the difference in absorption within the two-layer structure. From Bouger's Law (Siegel and Howell, 1981), the fraction of the energy absorbed in a layer from S to $S+dS$ below the surface is:

$$-\frac{di_\lambda(S)}{i_\lambda(0)} = a_\lambda(S)\exp\left(-\int_0^S a_\lambda\left(S^*\right)dS^*\right) \tag{115}$$

where $a_\lambda=4\pi\kappa/\lambda$ is the absorption coefficient. For the case of materials for which the extinction coefficient is independent of position, the fraction absorbed is:

$$-\frac{di_\lambda(S)}{i_\lambda(0)} = \frac{4\pi\kappa}{\lambda}\exp\left(-\frac{4\pi\kappa}{\lambda}S\right) \tag{116}$$

The carrier generation rate in the nth layer is the fraction of photon flux absorbed in this layer:

$$\begin{aligned} G_{n\lambda} &= \frac{\Phi_{p\lambda}}{l} \times \text{ (fraction absorbed)} \\ &= \frac{\Phi_{p\lambda}}{l} \times \int_{(n-1)l}^{nl} a_\lambda \exp(-a_\lambda S)dS \\ &= \frac{\Phi_{p\lambda}}{l e^{n a_\lambda l}}\left[e^{a_\lambda l} - 1\right] \end{aligned} \tag{117}$$

where each layer is of thickness l. The total generation rate for layer n is the integral over all frequencies of incident photons:

$$G_n = \int_0^{\lambda_g} G_{n\lambda} d\lambda = \frac{1}{l} \int_0^{\lambda_g} \frac{\Phi_{p\lambda}}{e^{na_\lambda l}} \left(e^{a_\lambda l} - 1 \right) d\lambda \tag{118}$$

where λ_g is the wavelength of the photon with an energy equal to the band gap. Note that for a single homojunction model of Chapter 5, there is a semi-infinite single layer. Substituting n=1 with $l \rightarrow$ into the integrand of Eq. 118 yields the familiar expression for the generation rate.

Consider a two level structure for which the top layer is l microns below the surface and the second layer extends from l to l_{bot}. The generation rate is:

$$\begin{aligned} G_{top_\lambda} &= \frac{\Phi_{p\lambda}}{l} \left(1 - e^{-a_\lambda^{top} l} \right) \\ G_{bot\lambda} &= \frac{\Phi_{p\lambda}}{l e^{a_\lambda^{top} l}} \left(1 - e^{-a_\lambda^{bot} (l_{bot} - l)} \right) \\ G_n &= \int_0^{\lambda_g^{top}} G_{top_\lambda} d\lambda + \int_0^{\lambda_g^{bot}} G_{bot\lambda} d\lambda \end{aligned} \tag{119}$$

To examine the performance of such a device, the generation rate expressed by Eq. 119 is combined with the model introduced in Chapter 5. The only adaptation necessary is to determine the dark current in each layer based on the band-gap of the material comprising the layer. From Eq. 111, the dark current becomes:

$$I_d = e \left(\frac{\left(n_i^2 \right)^{top} \sqrt{D_e}}{N_A \sqrt{\tau_e}} + \frac{\left(n_i^2 \right)^{bot} \sqrt{D_h}}{N_D \sqrt{\tau_h}} \right) \tag{120}$$

Notice that the junction was formed such that the diffusion coefficient of the holes combines with the intrinsic carrier concentration of the bottom layer. This combination ensures that the contribution of the low band-gap material to the dark current is attenuated by the low diffusion coefficient of the holes. The high band-gap material of the top layer has a lower intrinsic carrier concentration, thereby, counteracting the high electron

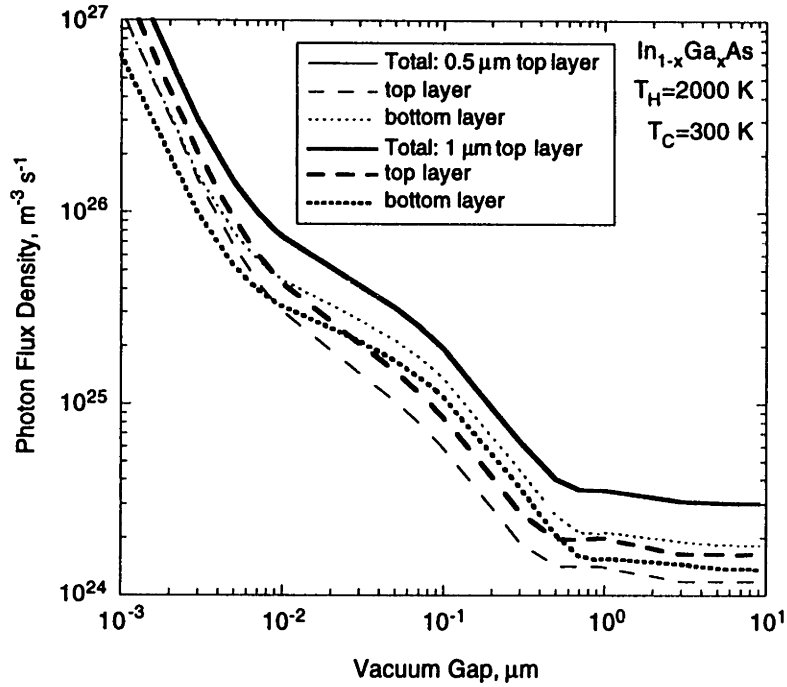

Figure 52: Distribution of light-generated carriers for a heterojunction between $In_{.8}Ga_{.2}As$ and $In_{.95}Ga_{.05}As$ placed at 0.5 μm or 1 μm below the surface.

mobility. The resulting dark current is less than that of the homojunction. It is this decreased dark current that permits improved performance of the heterojunction.

Figure 52 compares the photon flux density in the top and bottom layer of a 2-layer heterojunction. These results are for a device whose total thickness is 10 μm. The density of photons absorbed in each layer depends on the thickness of the layer. For a relatively thin top layer, most of the current is generated in the bottom layer. Notice that the total photon density for the entire device is the same for the case of a top layer of 0.5 μm thickness or 1 μm thickness, arising from the top layer's transparency to photons near, but just below, the band gap. The current, therefore, is the same as that for a homojunction of the lower band-gap material.

The decreased dark current improves the performance of the microscale device. Figure 53 shows the efficiency of a heterojunction device comprised of a 0.5 μm top layer of $In_{.8}Ga_{.2}As$ and a bottom layer of $In_{.95}Ga_{.05}As$. Also shown are the predicted

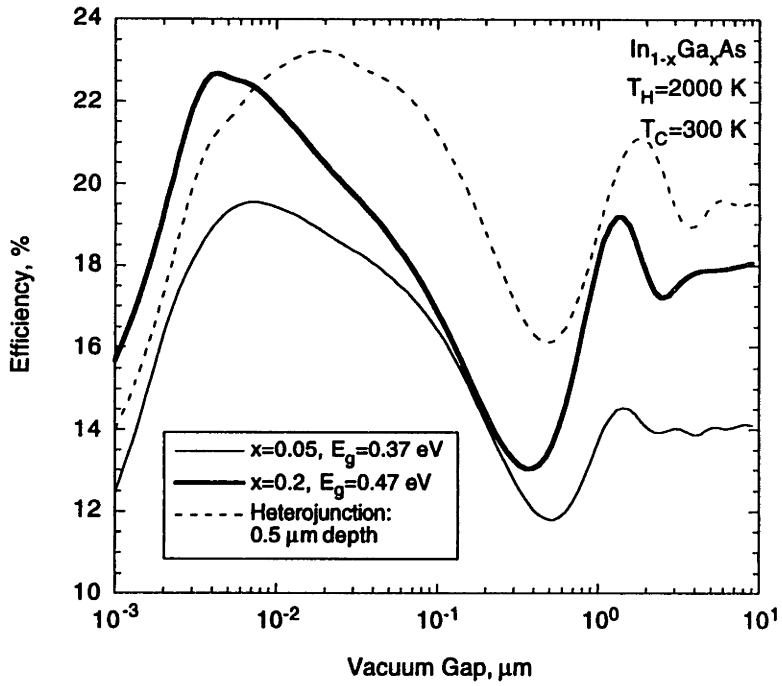

Figure 53: Comparison of efficiency for a heterojunction between $In_{.8}Ga_{.2}As$ and $In_{.95}Ga_{.05}As$ placed at 0.5 μm below the surface and homojunctions of the same band gaps.

efficiencies for the homojunctions formed from the materials of each of the layers. The efficiency at large spacing improves substantially over that of the low band-gap material. In addition, the efficiency increases at a higher value of the vacuum gap. Also noteworthy, is the increase in the minimum efficiency to levels greater than the homojunction.

The improvement due to the grading of the band gap in each level is a promising modification to the microscale thermophotovoltaic device. By examining different combinations of materials, layer thicknesses, and band gaps, the performance can be optimized.

6.4 Second Law Limitations

The results presented in the previous section suggest that the spacing effect may permit the improvement of the efficiency of thermophotovoltaic energy conversion. It is

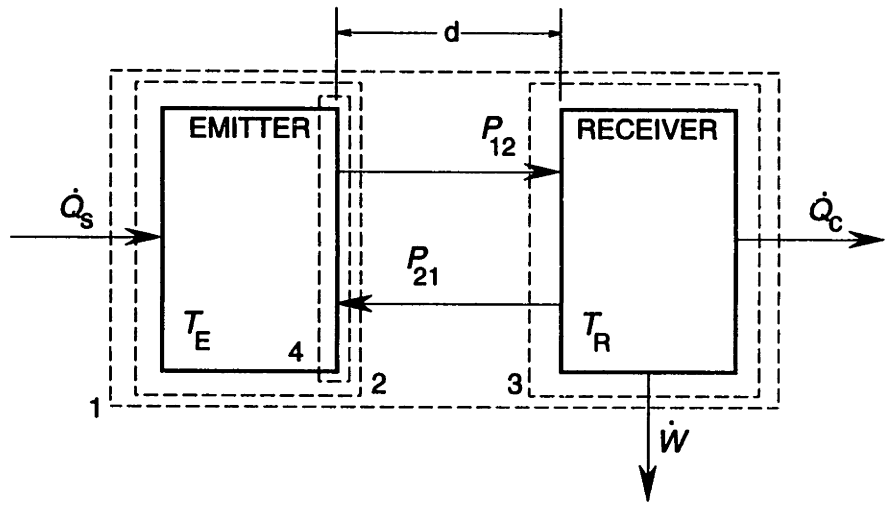

Figure 54: Schematic diagram of an energy converter for the Second Law analysis.

important to examine the entropy transfer for such devices in order to assess the maximum efficiency that this technology permits. The thermodynamic efficiency of the conversion of radiation into other forms of energy has been widely discussed. Landsberg and Tonge (1980) review the work prior to 1979, and Landsberg and Baruch (1989) offer corrections and extensions to the earlier work.

Consider an energy conversion device as shown in Fig. 54, which consists of an emitter and a receiver separated by a vacuum gap. The emitter is maintained at a constant temperature of T_E by a heat transfer, $\dot{Q}_s$, from a primary energy source, while the receiver is maintained at a temperature of T_R by another heat transfer, $\dot{Q}_c$, to a cooler environment. A vacuum gap of size d separates the emitter and receiver, so that radiative transfer is the sole thermal interaction between the surfaces. The device delivers work at a rate of $\dot{W}$ from the receiver. Figure 54 shows four control volumes whose surfaces are defined by dashed lines. Control volume 1 refers to the combined system of the emitter, receiver, and vacuum gap. Control volumes 2 and 3 refer to only the emitter and receiver, respectively. Control volume 4 is a very thin control volume extending from the surface of the emitter to about a penetration depth below the surface.

To examine the maximum efficiency of the system, consider the energy and entropy balances on control volume 1 in Fig. 54.

$$\begin{aligned} \dot{E} &= \dot{E}_E + \dot{E}_R \\ &= \dot{Q}_s - \dot{Q}_c - \dot{W} \\ \dot{S} &= \dot{S}_E + \dot{S}_R \\ &= \dot{Q}_s/T_E - \dot{Q}_c/T_R + \dot{S}_{g_E} + \dot{S}_{g_R} \end{aligned} \tag{121}$$

where the entropy generation within the device, due to internal process not otherwise specified, is $\dot{S}_g \geq 0$ and consists of contributions from both the emitter and receiver.

Note that the emitter and receiver are not assumed to operate in steady state; i.e. the energy and entropy of the device change at rates $\dot{E}$, $\dot{S}$. Steady state cannot be assumed *a priori,* because the stipulation that the emitter and receiver interact only through the transfer of radiative energy does not guarantee that the entropy transfer into the emitter by the heat interaction equals that leaving the emitter by radiation into the vacuum. It will be shown that for large vacuum gaps, the difference between the two is provided by entropy generation in the device, which permits steady-state operation. As the vacuum gap diminishes, however, the thermal field within the gap changes such that the entropy within it deviates from the equilibrium case. The resulting imbalance does not permit steady state operation, though the Carnot efficiency is still the maximum efficiency achievable for the *overall* system.

When the heat transfers into the emitter and out of the receiver maintain the temperatures of each surface, the energy of the emitter and receiver are constant. The energy and entropy balances become:

$$\begin{aligned} \dot{W} &= \dot{Q}_s - \dot{Q}_c \\ \dot{Q}_c &= \dot{Q}_s T_R/T_E - T_R\left(\dot{S}_E - \dot{S}_{g_E}\right) - T_R\left(\dot{S}_R - \dot{S}_{g_R}\right) \end{aligned} \tag{122}$$

The efficiency of the device is obtained by comparing the work delivered by the receiver to the heat needed to drive the device. From Eq. 122, the ratio is:

$$\begin{aligned}\eta &= \frac{\dot{W}}{\dot{Q}_s} \\ &= 1 - T_R/T_E - T_R/\dot{Q}_s\left(\dot{S}_E - \dot{S}_{g_E}\right) - T_R/\dot{Q}_s\left(\dot{S}_R - \dot{S}_{g_R}\right)\end{aligned} \tag{123}$$

For steady-state operation of a device in which all the interactions are reversible, the last two terms are zero, and the efficiency equals the Carnot efficiency.

To evaluate the rate of entropy storage or loss in the emitter and receiver for the unsteady case, entropy and energy balances must be obtained for each surface separately. For control volume 2, the energy and entropy balances are:

$$\begin{aligned}0 &= \dot{Q}_s - P_{12} + P_{21} \\ \dot{S}_E &= \dot{Q}_s/T_E - S_{12} + S_{21} + \dot{S}_{g_E}\end{aligned} \tag{124}$$

For control volume 3:

$$\begin{aligned}0 &= P_{12} - P_{21} - \dot{Q}_c - \dot{W} \\ \dot{S}_R &= S_{12} - S_{21} - \dot{Q}_c/T_R + \dot{S}_{g_R}\end{aligned} \tag{125}$$

where the heat interactions are assumed to maintain the temperature of the each surface such that the energy within each control volume is constant. The rate of entropy change in the emitter and receiver are obtained by eliminating the heat transfer in the entropy balance by using the energy balance.

$$\begin{aligned}\dot{S}_E - \dot{S}_{g_E} &= (P_{12} - P_{21})/T_E - S_{12} + S_{21} \\ \dot{S}_R - \dot{S}_{g_R} &= S_{12} - S_{21} - \left(P_{12} - P_{21} - \dot{W}\right)/T_R\end{aligned} \tag{126}$$

Combining Eq. 126 with Eq. 123 yields the efficiency of the overall system.

$$\begin{aligned}\eta &= 1 - T_R/T_E - T_R/\dot{Q}_s\left((P_{12} - P_{21})/T_E - \left(P_{12} - P_{21} - \dot{W}\right)/T_R\right) \\ &= 1 - T_R/T_E - \left(T_R/T_E - 1 + \dot{W}/\dot{Q}_s\right)\end{aligned} \tag{127}$$

which re-arranges to give the Carnot efficiency:

$$\eta = 1 - T_R/T_E = \eta_C \tag{128}$$

This analysis indicates that the overall device does not violate the Second Law; the maximum efficiency for the overall system is the Carnot efficiency, even when operating under unsteady conditions. In the Section 6.3, however, the efficiencies were determined by examining only the transfer of energy to and from the receiver. By examining the receiver and emitter separately, an upper limit to the efficiencies of Section 6.3 can be determined.

For the case where the emitter and receiver are separated by a vacuum gap that is large compared to the characteristic wavelength of the radiation in the gap, Planck's distribution provides the expressions for energy and entropy flux. Use of Planck's equilibrium expression implicitly assumes that the temperatures of the emitter and receiver are not too different. The net radiation field within the gap can be treated as a superposition of the contributions from each surface, which equals the radiation field of the isothermal cavity situation. The difference in temperature of the two surfaces, however, means that for a particular surface, there is a net imbalance in the amount of energy and entropy contributed *to* the field in the gap and the amount received *from* it. The net imbalance constitutes a flux of energy and entropy to the other surface via the vacuum gap. The assumptions implicit in this model require more analysis, but keeping in mind these reservations, it is used here to obtain expressions for the flux of entropy and energy into the gap from each surface.

For microscale devices, it is necessary to examine the influence of the vacuum gap on the transport of entropy from the emitter to the receiver, without assuming the equilibrium radiation given by Planck's distribution or modeling the emitter as a reservoir. From Eq. 125, the efficiency for the energy conversion in the receiver is:

$$\eta_R = \frac{\dot{W}}{P_{12} - P_{21}} = 1 - \frac{\dot{Q}_c}{P_{12} - P_{21}} \tag{129}$$

where the net radiative flux through the surface of the receiver is used as the net input to the "device". By using the entropy balance, the efficiency of the energy conversion in the receiver is:

$$\begin{aligned} \eta_R &= 1 - \frac{T_R\left(S_{12} - S_{21} + \dot{S}_{g_R} - \dot{S}_R\right)}{P_{12} - P_{21}} \\ &\leq 1 - T_R \frac{S_{12} - S_{21}}{P_{12} - P_{21}} \end{aligned} \tag{130}$$

where the equality holds for the limiting case: $\dot{S}_R - \dot{S}_{g_R} = 0$ or the device is operating reversibly in steady-sate.

Landsberg and Tonge (1980) introduce the effective *flux temperature* defined as the ratio of energy to entropy flux into a device to permit the examination of the performance of devices subjected to non-equilibrium radiation fields. The effective flux temperature is a means to characterize the source of energy "seen" by the device. Considering the receiver as a device subject to non-equilibrium radiation equal to the net flux across the vacuum gap yields a definition of the effective flux temperature of the source.

$$T_F \equiv \frac{P_{12} - P_{21}}{S_{12} - S_{21}} \tag{131}$$

For the moment, consider this definition as a purely mathematical substitution; its relation to the thermodynamic temperature is discussed later. Using this definition, the efficiency for the receiver from Eq. 130 becomes:

$$\eta_R \leq 1 - \frac{T_R}{T_F} \tag{132}$$

which is the expression for the Carnot efficiency based on the effective flux temperature.

To determine the limiting efficiency of the energy conversion within the receiver, it is necessary to determine the effective flux temperature as defined by Eq. 131. The net energy flux is given by the fluctuational electrodynamic formulation in Chapter 3.

Determination of the entropy transfer for a microscale device is required to evaluate the effective flux temperature.

Landsberg and Tonge (1980) provide a general means of evaluating the entropy transfer that can be used away from equilibrium. Their approach is used here to consider the effect of spacing on the entropy transfer. Let $P(N_1, N_2,...)$ be the probability of finding N_1 bosons in a single-particle quantum state 1, N_2 in state 2, etc. Assuming that the probability of each state, $p_j(N_j)$, is independent of the other quantum states (the particles are bosons) yields:

$$P(N_1, N_2,...) = p_1(N_1)p_2(N_2)... \tag{133}$$

The probability of an additional particle occupying the state j is independent of the number already in the state. Thus $p_j(N_j) \propto q_j^{N_j}$ where q_j is an undetermined positive number. Normalization then gives:

$$p_j(N_j) = (1-q_j)q_j^{N_j}, \quad 0 \le q_j \le 1 \tag{134}$$

The mean occupancy number n_j of state j is:

$$n_j = \sum_{N=0}^{\infty} N q_j^{N_j}(1-q_j) = \frac{q_j}{1-q_j} \tag{135}$$

The entropy of the system is obtained by summing the probability over all possible states:

$$\begin{aligned} S &= -k_b \sum_{N_1=0}^{\infty} \cdots \sum_{N_j=0}^{\infty} \cdots P \ln(P) \\ &= -k_b \sum_j \sum_{N_j} \left[(1-q_j)q_j^{N_j} \ln\left[(1-q_j)q_j^{N_j} \right] \right] \\ &= k_b \sum_j \left[(1+n_j)\ln[1+n_j] - n_j \ln n_j \right] \end{aligned} \tag{136}$$

This expression for the entropy of a gas of bosons can be adapted for a continuous spectrum of quantum states by assuming that the sum can be replaced by an integral. The influence of the small gap on the validity of changing from a summation to an integral needs a more thorough examination. In the present case, for which the radiation is unpolarized and the emitter subtends a half-angle of 90° at the receiver, the results of Landsberg and Tonge (1980) reduce to:

$$S = \frac{2\pi k_b}{c^2} \int \left[\left(1 + n_\nu\right) \ln\left[1 + n_\nu\right] - n_\nu \ln n_\nu \right] \nu^2 d\nu \tag{137}$$

where n_ν is the spectral variation in the mean occupancy number. Equation 137 relates the entropy of the boson gas to a non-equilibrium occupancy number. By decreasing the size of the vacuum gap, the mean occupancy number changes from the equilibrium value. The influence of the vacuum gap size on the mean occupancy number can be determined from the fluctuational electrodynamic formulation:

$$n_\nu = \left(\frac{c}{2\nu}\right)^2 \frac{P_{12_\nu}}{E_p} = \left(\frac{c}{\omega}\right)^2 M n_b \quad \text{where } n_b = \frac{1}{\exp\left(\dfrac{h\omega}{2\pi k_b T_1}\right) - 1} \tag{138}$$

This expression for the occupancy number with Eq. 137 provides the contribution of entropy in the gap from the surface at temperature T_1, by assuming that the surface at this temperature contributes a radiation field equal to the isothermal equilibrium situation. Due to the presence of the factor M, the expression for entropy given by Eq. 137 is a non-equilibrium entropy flux into the gap. The expression for n_b is the occupancy number for an equilibrium boson gas, and M is the proximity function from the fluctuational electrodynamic approach. For large vacuum gaps, M approaches $(\omega/c)^2$ and Bose-Einstein statistics obtained. This expression for the occupancy comes from accounting for the total allowed momentum values between k and $k+dk$, including both polarizations:

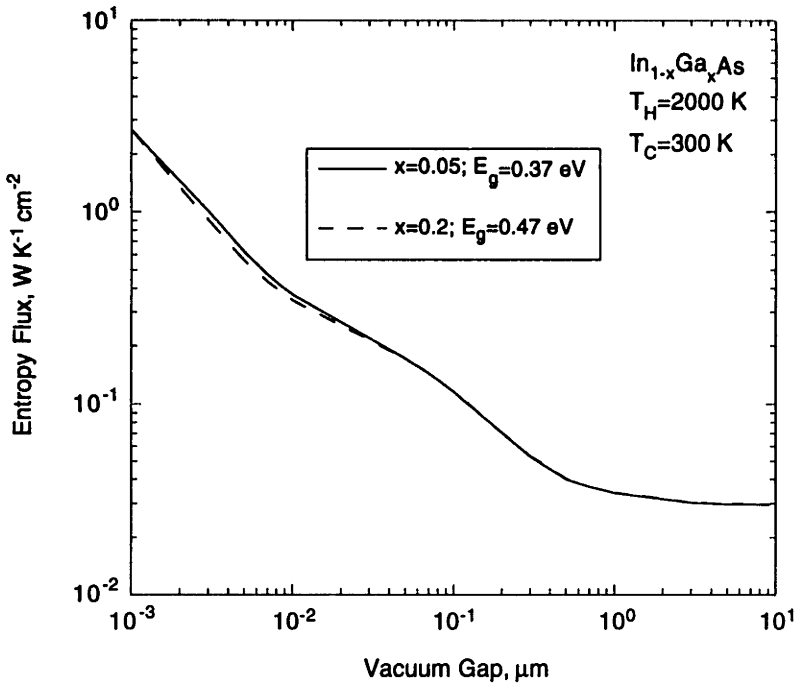

Figure 55: Entropy transfer associated with microscale radiative transfer between the emitter and receiver.

$$P_{12_k}dk = \left(2f(k)4\pi k^2 dk\right)\frac{h\omega}{2\pi} \quad \text{but} \quad f(k) = \frac{n_{\mathrm{p}}}{(2\pi)^3}$$
$$\therefore \quad n_{\mathrm{p}} = \frac{\pi^2 P_{12_k}}{k^2 E_{\mathrm{p}}} = \frac{c^2 M}{\omega^2} n_{\mathrm{b}} \tag{139}$$

This derivation assumes that the near-field is discretized in the same manner as the far-field. The possible frequencies of the photons are found by examining the normal modes of oscillation that create standing waves within the vacuum gap, and differentiating to find the number of states in a frequency range from ν to $\nu+d\nu$ (Grossman, 1969). In other words, the imaginary wave numbers discretize in a manner exactly equal to the real wave numbers.

The entropy flux can be calculated for a particular device by specifying the material properties and integrating over all frequencies. Figure 55 shows the result of a computation for several band gaps. The entropy flux increases as the emitter and receiver

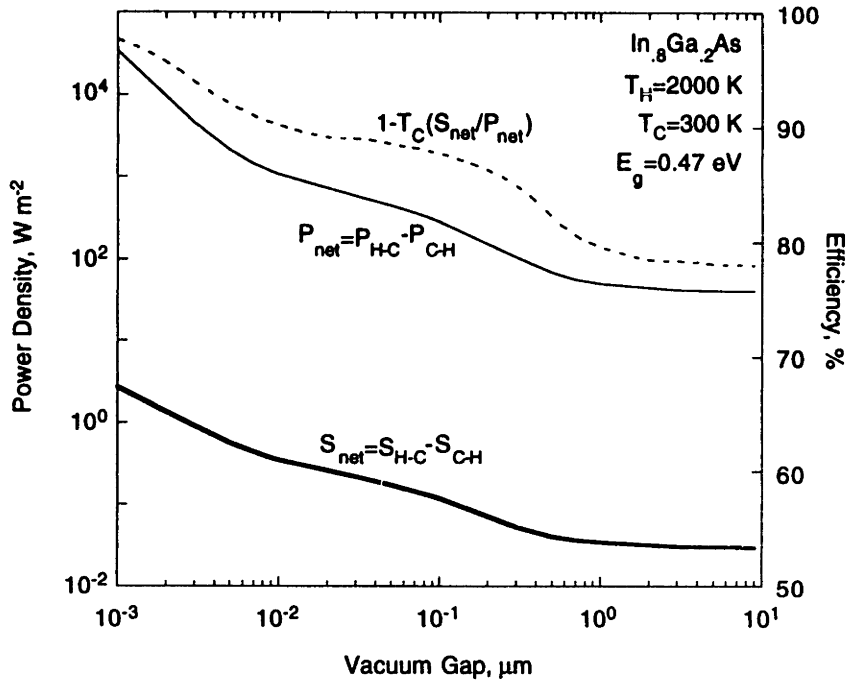

Figure 56: Comparison of the entropy and energy fluxes as a function of vacuum gap.

are brought close together. The effect of the enhanced entropy flux due to the spacing effect is illustrated in Fig. 56, where the net energy and entropy fluxes are shown for a device modeled with the properties of $In_{0.8}Ga_{0.2}As$.

The broken line in Fig. 56 is the efficiency of the energy conversion within the receiver using the definition of the effective flux temperature. Consider the result at large spacing. For equilibrium black body radiation, Landsberg and Tonge (1980) relate the energy and entropy fluxes through a surface to the energy and entropy density of black body radiation within an enclosure of volume V. Their derivations yield the familiar expressions for the energy and entropy fluxes of equilibrium black body radiation:

$$\dot{E} = \frac{c}{4}\frac{U}{V} = \sigma T_E^4$$
$$\dot{S} = \frac{c}{4}\frac{S}{V} = \frac{4}{3}\sigma T_E^3 \qquad (140)$$

where the temperature of the emitter is used to characterize the radiation in the gap. Substitution of these expressions into Eq. 130 provides a rough estimate of the efficiency at large vacuum gaps; the efficiency is less than the Carnot efficiency:

$$\begin{aligned} \eta_R &\le 1 - T_R \frac{\frac{4}{3}\sigma T_E^3}{\sigma T_E^4} \\ &\le 1 - \frac{4}{3}\frac{T_R}{T_E} < \eta_C \end{aligned} \tag{141}$$

For the case shown in Fig. 56, T_R=300 K and T_E=2000 K, which yields an efficiency of 80%. At large spacing, the fluctuational electrodynamic analysis of the microscale device predicts an efficiency completely consistent with the black body result. The difference is due to the non-black body material properties of $In_{1-x}Ga_xAs$.

The spacing effect enhances the energy density in the vacuum gap to a greater degree than it does the entropy, owing to the reduced number of microstates that the radiation field can obtain within the small vacuum gap for the same macroscopic properties, T_R and T_E. As a result, the effective flux temperature, T_F, increases, and by Eq. 132, the limiting efficiency of the energy conversion within the receiver also increases. The broken line in Fig. 56 indicates that the maximum efficiency increases from the large spacing result as the vacuum gap decreases. At first glance, this result seems to be in violation of the Second Law, since the efficiency increases beyond the Carnot efficiency as evaluated using the *thermodynamic* temperature of the emitter. The use of the absolute thermodynamic temperature, however, is valid only when the radiation interaction can be considered a heat interaction with a reservoir at the absolute temperature.

Recall that for the overall system a maximum efficiency equal to the Carnot efficiency was obtained. For the receiver considered independent of the emitter, however, the maximum efficiency increases due to the spacing effect. Because of the

stipulation that a heat interaction into the emitter drives the device, the overall system performance is limited to the Carnot efficiency. Because the small gap enhances the energy flux to a greater degree than the entropy flux, the entropy within the emitter must increase.

Consider the entropy balance of control volume 2. The entropy balance in Eq. 126 can be re-arranged using the definition of the effective flux temperature (Eq. 131).

$$\begin{aligned} \dot{S}_E - \dot{S}_{g_E} &= (P_{12} - P_{21})/T_E - S_{12} + S_{21} \\ &= (P_{12} - P_{21})/T_E \left[1 - \frac{T_E}{T_F} \right] \end{aligned} \tag{142}$$

At large vacuum gaps, T_F was found to be $3/4T_E$, and therefore:

$$\dot{S}_E - \dot{S}_{g_E} = -\frac{1}{3} \frac{P_{12} - P_{21}}{T_E} \tag{143}$$

The entropy storage within the emitter is less than the entropy generation. At large spacing, therefore, the emitter can operate in steady state, but does so irreversibly. This irreversibility is generated near the surface of the emitter by the generation of the radiation field.

As the vacuum gap decreases, the effective flux temperature tends toward a value very much larger than the emitter temperature, because of the large increase in energy flux. From Eq. 142, therefore, the difference between the entropy storage and entropy generation rates is a positive quantity:

$$\dot{S}_E - \dot{S}_{g_E} \approx \frac{P_{12} - P_{21}}{T_E} \tag{144}$$

The entropy within the emitter must increase, since the heat interaction carries more entropy into the emitter than the emission at the surface into the gap can support. The emitter cannot operate at steady-state as the gap decreases.

Because the spacing effect influences the entropy of the radiation field, it is important to investigate alternative methods of providing energy to the emitter other than heat interactions, so that the efficiency of the overall system can be improved. The present analysis suggests that the spacing effect augments the radiation field such that the non-equilibrium distribution of radiation no longer resembles a heat interaction. There is a component of the energy flux from the emitter that could be considered work rather than heat. As a result, the effective flux temperature is greater than the absolute thermodynamic temperature defined as:

$$\frac{1}{T_A} \equiv \left(\frac{\partial S}{\partial U}\right)_V \tag{142}$$

Landsberg and Tonge (1980) compare the absolute thermodynamic temperature and the effective flux temperature for several different types of radiation distributions. For black body radiation they find, as shown by Eq. 140:

$$T_A = T_E \quad \text{while} \quad T_F = \frac{3}{4} T_E \tag{143}$$

Thus, T_E is an absolute thermodynamic temperature, while T_F is not. For near-monochromatic radiation in a box isolated from its surroundings, Landsberg and Tonge (1980) show that T_E=T_F; i.e. for such situations, which arise when analyzing photosynthesis, the flux temperature is an absolute thermodynamic temperature.

To model diffuse and direct conversion of solar radiation, Landsberg and Tonge (1980) introduce the concept of dilute black body radiation, which is based on a spectrum whose mean occupancy number, n_ν, is given by:

$$n_\nu = \frac{\varepsilon}{\exp\left(\frac{h\nu}{k_b T}\right) - 1} \tag{140}$$

which resembles the Bose-Einstein statistics multiplied by a factor ε. For cases where $\varepsilon<1$, Landsberg and Tonge (1980) name the distribution *dilute black body radiation*, which represents a non-equilibrium situation. For microscale devices, the factor $\varepsilon>1$ for sufficiently small vacuum gap, and therefore, becomes an intensifying factor. The result, as shown in Fig. 56, is the definition of an effective flux temperature that characterizes the field of radiation in the microscale vacuum gap, which is greater than the absolute thermodynamic temperature of the emitter.

This characterization of the radiation field permits an alternative interpretation of the spectral distribution of the energy due to the spacing effect. Recall Fig. 9, which shows the radiative flux in the vacuum gap. As the spacing decreases, the distribution resembles a Planckian distribution at a higher absolute temperature. The entropy analysis given above indicates that this higher temperature is in fact the effective flux temperature of the radiation field caused by the influence of the small vacuum gap.

The microscale thermophotovoltaic device represents a means to increase the limiting efficiency of photovoltaic energy conversion. The predictions of Section 6.3 indicate that there are substantial irreversibilities involved with the absorption of photons and the creation of electron-hole pairs by the photovoltaic effect. So called two-level models of solar cells have been developed to analyze these irreversibilities (Baruch, 1985; Parrott, 1982; De Vos and Pauwels, 1981). The determination of the effect of microscale radiative transfer on these models is reasonable next step in the analysis of the ideal performance of microscale thermophotovoltaic energy conversion.

6.5 Development of Microscale Thermophotovoltaic Devices

The analysis of microscale thermophotovoltaic devices using the fluctuational electrodynamic formalism indicates several promising improvements that can be made to thermophotovoltaic energy conversion. The most important prediction of the analysis is the determination that the power density in a microscale device can be as great as ten

times that of a standard thermophotovoltaic device. This increase in power density will permit smaller and lighter systems whose initial cost will be dramatically reduced.

The improved power density comes with marginal gains in efficiency. The loss of the traveling wave components of the field reduces the efficiency over a small vacuum gap range. However, for low enough band-gap and vacuum gap, the efficiency can also increase. The magnitude of the increase in efficiency depends in an interrelated way on the temperature, alloy composition, and doping of the materials comprising the device.

Introducing materials such as mercury cadmium telluride that have favorable material properties at low temperature will permit the increase in efficiency by cooling the receiver. The fabrication of the receiver as a heterojunction will permit even further increases in efficiency, over all vacuum gaps. The efficiency of such devices increases at a larger band gap than the homojunction devices.

A Second Law analysis indicates that the microscale thermophotovoltaic device permits an increase in the maximum efficiency by changing the relative amount of energy and entropy that are transferred by microscale radiative transfer. The large difference between the predicted efficiency using the device model and the maximum efficiency from the Second Law analysis indicates that improvements in junction design may be necessary to utilize the near-field energy more effectively.

This thesis provides a firm basis for the concept of microscale thermophotovoltaic energy conversion. There are a number of issues, introduced in this work, that may lead to better improvement of the device performance.

The careful design of the emitter may decrease low energy photons in the vacuum gap. The present model examines only Drude-like materials for the emitter. By using selective emitters of rare-earth oxides, improved performance should be attainable since these materials emit in a narrow frequency range.

The heterojunction analysis indicates that a series of layers with a graded band gap may permit a further reduction in the dark current. An examination of the influence of multiple layers and layer thickness may lead to further performance improvements.

There are several thermophotovoltaic-system configurations that the microscale concept may take. The standard configuration includes a hot emitter placed directly opposite the receiver separated by a small vacuum gap, which is the system analyzed in this thesis. The emitter provides the energy to drive the conversion process in the cooler receiver. The receiver is a pn-junction diode with one or more junctions, each of which may have a different band-gap energy.

An alternative system is an intermediate re-radiator configuration. This system includes a material between the emitter and receiver, which absorbs the energy from the emitter and re-radiates it across a different frequency range, thereby acting as a band-pass filter with characteristics more closely matched to the receiver.

Another alternative involves a solar source re-radiator that absorbs energy from the sun and acts as an effective emitter. The solar energy elevates the free-electron gas into a non-equilibrium state that permits the gas to radiate photons at lower frequency than the sun. By optimizing the material properties of the re-radiator, the emitted radiation can be tuned to the frequency range most suitable for the microscale thermophotovoltaic device.

In all of these alternative configurations, the close proximity of the receiver to the emitter or re-radiator marks the technology as a microscale energy conversion device.

Microscale thermophotovoltaic device performance will be further enhanced by developing new materials with properties specifically fashioned to compliment this new technology. The results of the analysis in Section 6.3 indicate that materials with the properties summarized in Table 6 will permit better performance from these devices. The focus on developing materials to meet the criteria of microscale thermophotovoltaic energy conversion constitutes a new avenue of research for material science.

Property	Desired Range	Reference
Optical Constants	Receiver: $n=\kappa \ll 1$ $E < E_g$ $n=\kappa \ 1$ $E > E_g$ Emitter: $n=\kappa \gg 1$ $E < E_g$ $n=\kappa \ 1$ $E > E_g$	6.1.1 6.1.3
Band gap, eV	$E_p = T(\mathrm{K})/2333$ $E_g < E_p$ $E_g > E_p/2$	5.1 6.3.4
Mobility, $cm^2\ V^{-1}\ s^{-1}$	low: < 900	6.1.2
Dopant Concentration, cm^{-3}	high: $N_A\ N_D > 10^{19}$	6.3.5
Intrinsic Carrier Concentration, cm^{-3}	low: $< 10^{14}$	6.2.2

Table 6: Desired material properties for the improvement of microscale thermophotovoltaic energy conversion devices.

Appendices

Appendix A: Numerical Integration Considerations

The complex nature of the integrands of Eq. 43 and Eq. 88 through Eq. 91 does not permit analytical evaluation of the integrals. The integrands of these equations have numerous integrable singularities at unknown places between the upper and lower bounds. Simpson's rule or Romberg's method can be adapted by picking out each singularity and integrating between them. For large vacuum gaps, however, the number of singularities goes to infinity, and the computation time becomes prohibitive. Therefore, a variable-step-size differential equation integration routine must be employed.

A fourth-order Runge-Kutta method with adaptive step-size control achieves good accuracy by taking many small steps through the regions where the integrands vary a great deal (Press et al., 1986). Where the function is more smooth, the routine takes large steps. Step-doubling was used together with a fifth-order Runge-Kutta step to permit the variation in step size. Press et al. (1986) provide a very good discussion of the subtleties involved in using such a routine to solve sets of ordinary differential equations. The only changes made here were a reduction in function calls, which can be obtained since in the present study the set of equations consisted of only *one* equation. The same values for the parameters that govern the operation of the integration listed in Press et al. (1986) gave fast convergence with reasonable accuracy.

This routine was used for the integration over wave number for the net flux between the surfaces and also for the integration of the full expressions for the proximity function from the fluctuational electrodynamic formulation.

Appendix B: Fluctuational Electrodynamic Formulation

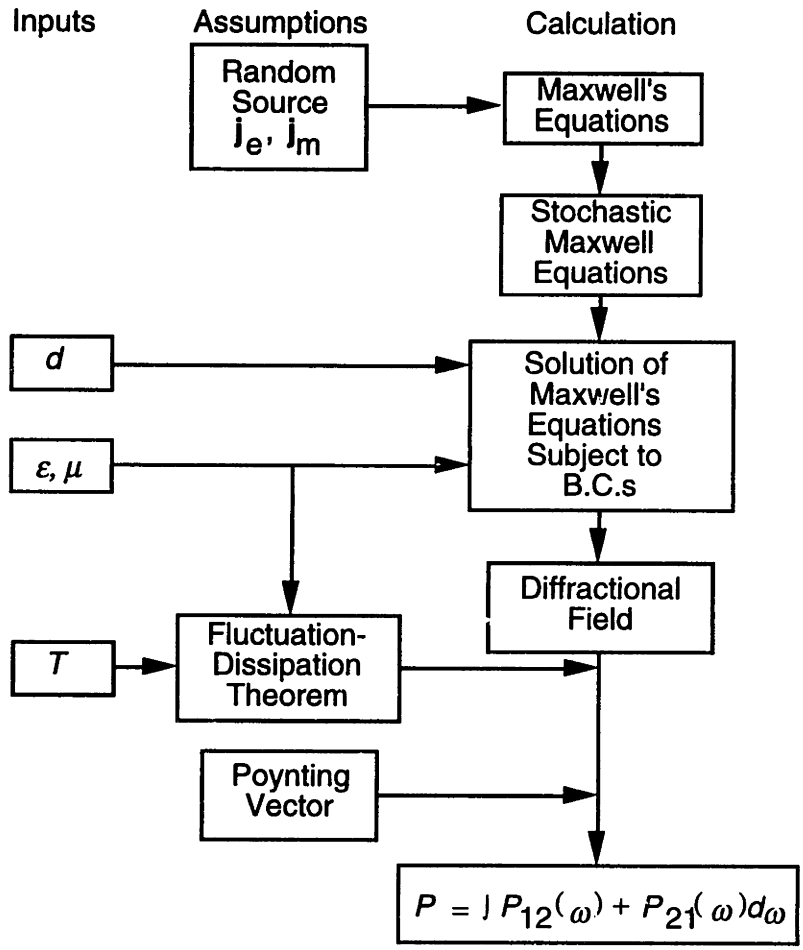

Figure 57: Schematic representation of the fluctuational electrodynamic formulation used to calculate the net flux between two surfaces.

References

Ahrenkiel, R.K., Wangensteen, T., Al-Jassim, M.M., Wanlass, M., and Coutts, T., 1995, "Recombination Lifetime of $In_{1-x}Ga_xAs$ Ternary Alloys," *AIP Conference Proceedings 321: The First NREL Conference on Thermophotovoltaic Generation of Electricity*, American Institute of Physics, New York, pp. 412-424.

Amirtharaj, P.M., 1991, "Mercury Cadmium Telluride ($Hg_{1-x}Cd_xTe$)," *Handbook of Optical Constants of Solids II*, ed. E. D. Palik, Academic Press, New York, pp. 655-689.

Anderson, W.W., 1977, "Tunnel Current Limitations of Narrow Bandgap Infrared Charge Coupled Devices," *Infrared Physics*, Vol. 17, pp. 147-164.

Aspnes, D.E., and Arwin, H., 1984, "Nondestructive Analysis of $Hg_{1-x}Cd_xTe$ (x=0.00, 0.20, 0.29, and 1.00) by Spectroscopic Ellipsometry," *J. Vac. Sci. Technol. A*, Vol. 2, pp. 1309-1325.

Baruch, P., 1985, "A Two-Level System as a Model for a Photovoltaic Solar Cell," *J. Appl. Phys.*, Vol. 57, pp. 1347-1355.

Boehm, R.F., and Tien, C.L., 1970, "Small Spacing Analysis of Radiation Transfer Between Parallel Metallic Surfaces," *J. Heat Transfer*, Vol. 92, pp. 405-411.

Boltzmann, L., 1884, "Ableitung des Stefan 'schen Gesetzes betreffend die Abhängigkeit der Wärmestrahlung von der Temperatur aus der electromagnetischen Lichttheorie," *Ann. Phys.*, Vol. 22, pp. 291-294.

Born, M., and Wolf, E., 1965, *Principles of Optics*, Pergamon Press, New York, p. 64.

Borrego, J., Zierak, M., and Charache, G., 1995, "Parameter Extraction for TPV Cell Development," *AIP Conference Proceedings 321: The First NREL Conference on Thermophotovoltaic Generation of Electricity*, American Institute of Physics, New York, pp. 371-378.

Broman, L., Jarefors, K., Marks, J., and Wanlass, M., 1996, "Electricity from Wood Powder Report on a TPV Generator in Progress," *AIP Conference Proceedings 358: The Second NREL Conference on Thermophotovoltaic Generation of Electricity*, American Institute of Physics, New York, pp. 177-180.

Caren, R.P., 1972a, "Radiation Energy Density and Radiation Heat Flux in Small Rectangular Cavities," *J. Heat Transfer*, Vol. 94, pp. 289-294.

Caren, R.P., 1972b, "Radiation Heat Transfer between Closely Spaced Metal Surfaces at Low Temperature: The Impact of Discrete Modes of the Radiation Field," *J. Heat Transfer*, Vol. 94, pp. 295-299.

Caren, R.P., 1974, "Thermal Radiation between Closely Spaced Metal Surfaces at Low Temperatures Due to Traveling and Quasi-stationary Components of the Radiation Field," *Int. J. Heat Mass Transfer*, Vol. 17, pp. 755-765.

Chester, G.V., 1963a, "The Boltzmann Equation for Homogeneous Electric Fields," *Proc. Phys. Soc.*, Vol. 81, pp. 938-948.

Chester, G.V., 1963b, "The Theory of Irreversible Processes," *Rep. Progr. Phys.*, Vol. 26, pp. 411-472.

Coutts, T.J., and Benner, J.P., 1995, *AIP Conference Proceedings 321: The First NREL Conference on Thermophotovoltaic Generation of Electricity*, American Institute of Physics, New York.

Cravalho, E.G., Domoto, G.A., and Tien, C.L., 1968, "Measurements of Thermal Radiation of Solids at Liquid Helium Temperatures," *Progress in Aeronautics and Astronautics*, ed. J.T. Bevans, Vol. 21, pp. 531-542.

Cravalho, E.G., Tien, C.L., and Caren, R.P., 1967, "Effect of Small Spacing on Radiative Transfer Between Two Dielectrics," *J. Heat Transfer*, Vol. 89, pp. 351-358.

De Vos, A., and Baruch, P., 1989, "The Thermodynamics of the Conversion of Radiation Energy for Photovoltaics," *J. Phys. A: Math. Gen.*, Vol. 22, pp. 1911-1926.

DiMatteo, R.S., 1996, *Enhanced Semiconductor Carrier Generation Via Microscale Radiative Transfer; MPC - An Electric Power Finance Instrument Policy; Interrelated Innovations in Emerging Energy Technologies*, S.M. thesis, Department of Electrical Engineering and Computer Science, Massachusetts Institute of Technology.

Domoto, G.A., Boehm, R.F., and Tien, C.L., 1970, "Experimental Investigation of Radiative Transfer between Metallic Surfaces at Cryogenic Temperatures," *J. Heat Transfer*, Vol. 92, pp. 412-417.

Dugdale, J.S., 1977, *The Electrical Properties of Metals and Alloys*, Edward Arnold Publishing Ltd., London, p. 169 and p. 243.

Dyos, G.T., and Farrell, T., 1992, *Electrical Resistivity Handbook*, Peter Peregrinus Ltd., London, p. 132 and p. 207.

Emslie, A.G., 1962, "Fundamental Limitations of Multi-layered Radiation Shields," *Conference of Aerodynamically Heated Structures*, ed. P.E. Glasen, Prentice Hall, Englewood Cliffs, pp. 135-150.

Finkman, E., and Nemirovsky, Y., 1979, "Infrared Optical-Absorption in $Hg_{1-x}Cd_xTe$," *J. Appl. Phys.*, Vol. 50, pp. 4356-4361.

Fraas, L., Ballantyne, R., Samaras, J., and Seal, M., 1995, "Electric Power Production Using New GaSb Photovoltaic Cells with Extended Infrared Response," *AIP Conference Proceedings 321: The First NREL Conference on Thermophotovoltaic Generation of Electricity*, American Institute of Physics, New York, pp. 44-53.

Fragstein, C., 1950, "Energy Transfer at the Interface Between Two Absorbing Media with an Emphasis on the Heat Radiation in Absorbing Bodies," *Ann. Phys.*, Vol. 7, p. 63.

Green, M.A., 1982, *Solar Cells: Operating Principles, Technology, and System Applications*, Prentice-Hall, Inc., Englewood Cliffs, NJ, Chapters 3, 4, and 8.

Grinberg, G.A., 1948, *Selected Problems in Mathematical Theory of Electric and Magnetic Phenomena*, Publishing House, Academy of Science, USSR.

Grossman, L.M., 1969, *Thermodynamics and Statistical Mechanics*, McGraw-Hill Co., New York, Chapter 8.

Hansen, G.L., and Schmit, J.L., 1983, "Calculation of Intrinsic Carrier Concentration in $Hg_{1-x}Cd_xTe$," *J. Appl. Phys.*, Vol. 54, pp. 1639-1640.

Hansen, G.L., Schmit, J.L., and Casselman, T.N., 1982, "Energy-gap versus Alloy Composition in $Hg_{1-x}Cd_xTe$," *J. Appl. Phys.*, Vol. 53, pp. 7099-7101.

Hargreaves, C.M., 1969, "Anomalous Radiative Transfer between Closely-Spaced Bodies," *Phys. Letts.*, Vol. 30A, pp. 491-492.

Hargreaves, C.M., 1973, "Radiative Transfer between Closely-Spaced Bodies," *Philips Res. Repts. Suppl.*, No. 5, pp. 1-80.

Hebb, J.P., 1993, *Infrared Absorption in Doped Semiconductors Due to Direct Intersubband Transitions*, S.M. thesis, Department of Mechanical Engineering, Massachusetts Institute of Technology.

Heime, K., 1989, *InGaAs Field-Effect Transistors*, Wiley & Sons, New York, Chapter 3.

Iles, P.A., 1995, "Photovoltaic Principles Used in Thermophotovoltaic Generators," *AIP Conference Proceedings 321: The First NREL Conference on Thermophotovoltaic Generation of Electricity*, American Institute of Physics, New York, pp. 67-79.

Jain, R.K., Wilt, D.M., Jain, R., Landis, G.A., and Flood, D.J., 1996, "Lattice-Matched and Strained InGaAs Solar Cells for Thermophotovoltaic Use," *AIP Conference Proceedings 358: The Second NREL Conference on Thermophotovoltaic Generation of Electricity*, American Institute of Physics, New York, pp. 375-386.

Jain, R.K., Wilt, D.M., Landis, G.A., Jain, R., Weinberg, I., and Flood, D.J., 1995, "Modeling of Low-Bandgap Solar Cells for Thermophotovoltaic Applications," *AIP Conference Proceedings 321: The First NREL Conference on Thermophotovoltaic Generation of Electricity*, American Institute of Physics, New York, pp. 202-209.

Krist, K., 1995, "GRI Research on Thermophotovoltaics," *AIP Conference Proceedings 321: The First NREL Conference on Thermophotovoltaic Generation of Electricity*, American Institute of Physics, New York, pp. 54-66.

Kruse, P.W., 1981, "The Emergence of ($Hg_{1-x}Cd_xTe$) as a Modern Infrared Sensitive Material," *Semiconductors and Semimetals*, eds. R.K. Willardson and A.C. Beer, Academic Press, New York, Vol. 18, pp. 1-20.

Kubo, R., 1966, "The Fluctuation-Dissipation Theory," *Rep. Progr. Phys.*, Vol. 29, pp. 255-284.

Kutateladze, S.S., Rubtsov, N.A., and Bal'tsevich, Ya. A., 1979, "Effect of Magnitude of Gap between Metal Plates on their Thermal Interaction at Cryogenic Temperatures," *Sov. Phys. Dokl.*, Vol. 8, pp. 577-578.

Landsberg, P.T., and Pauwels, H., 1981, "On the Thermodynamic Limit of Photovoltaic Energy Conversion," *Appl. Phys.*, Vol. 25, pp. 119-125.

Landsberg, P.T., and Tonge, G., 1980, "Thermodynamic Energy Conversion Efficiencies," *J. Appl. Phys.*, Vol. 51, No. 7, pp. R1-R20.

Leung, E.M.W., Fast, R.W., Hart, R.W., and Heim, J.R., 1979, "Techniques for Reducing Radiative Heat Transfer between 77K and 4.2K," *Advances in Cryogenic Engineering*, Vol. 25, pp. 489-499.

Levin, M.L., Polevoi, V.G., and Rytov, S.M., 1980, "Contribution to the Theory of Heat Exchange Due to a Fluctuating Electromagnetic Field," *Sov. Phys. JETP*, Vol. 6, pp. 1054-1063.

Loomis, J.J., and Maris, H.J., 1994, "Theory of Heat Transfer by Evanescent Electromagnetic Waves," *Phys. Rev. B*, Vol. 50, pp. 18517-18524.

MacDonald, D. K.C., 1956, "Electrical Conductivity of Metals and Alloys at Low Temperatures," *Handbuch der Physik*, Vol. 14, pp. 137-197.

Miller, L.S., and Mullin, J.B., 1991, *Electronic Materials: from Silicon to Organics*, Plenum Press, New York, Chapter 7.

Nyquist, H., 1928, "Electric Agitation of Electric Charge in Conductors," *Phys. Rev.*, Vol. 32, pp. 110-113.

Olivia, J.D., and Eastman, L.F., 1980, "Liquid Phase Epitaxial Growth and Characterization of High Purity Lattice-Matched $Ga_xIn_{1-x}As$ on <111>B InP," *J. Electronic Materials*, Vol. 9, pp. 693-712.

Parrott, J.E., 1982, "Transport Theory of Semiconductor Energy Conversion," *J. Appl. Phys.*, Vol. 53, pp. 9105-9111.

Pierret, R.F., 1987, *Advanced Semiconductor Fundamentals*, Addison-Wesley Publishing Company, Reading, MA, Chapters 3 and 4.

Pines, M.Y., and Stafsudd, O.M., 1980, "Recombination Processes in Intrinsic Semiconductors Using Impact Ionization Capture Cross Sections in Indium Antimonide and Mercury Cadmium Telluride," *Infrared Physics*, Vol. 20, pp. 73-91.

Planck, M., 1959, *The Theory of Heat Radiation*, (English translation of *Wärmestrahlung*, second edition, 1913), Dover Publishing Co., New York.

Polder, D., and Van Hove, M., 1971, "Theory of Radiative Heat Transfer Between Closely Spaced Bodies," *Phys. Rev. B*, Vol. 4, pp. 3303-3314.

Press, W.H., Flannery, B.P., Teukolsky S.A, and Vetterling, W.T., 1986, *Numerical Recipes: The Art of Scientific Computing*, 1st ed., Cambridge University Press, Cambridge, Chapter 15.

Regan, T.M., Martin, J.G., and Riccobono, J., 1995, "TPV Conversion of Nuclear Energy for Space Applications," *AIP Conference Proceedings 321: The First NREL Conference on Thermophotovoltaic Generation of Electricity*, American Institute of Physics, New York, pp. 322-330.

Reine M.B., Sood, A.K., and Tredwell, T.J., 1981, "Photovoltaic Infrared Detectors," Chapter 6 of *Semiconductors and Semimetals*, Vol. 18: Mercury Cadmium Telluride, eds. R.K. Willardson and A.C. Beer, Academic Press, New York.

Reuter, G.E.H., and Sondheimer, E.H., 1948, "The Theory of the Anomalous Skin Effect in Metals," *Proc. Roy. Soc.*, Vol. A195, pp. 336-364.

Rogalski, A., 1988, "Analysis of the R_0A Product in n^+-p $Hg_{1-x}Cd_xTe$ Photodiodes," *Infrared Physics*, Vol. 28, pp. 139-153.

Rytov, S.M., 1953, *The Theory of Electrical Fluctuations and Thermal Radiation*, (English translation by H. Erkku, Air Force Research Center, Bedford MA, 1959), Publishing House, Academy of Science, USSR.

Rytov, S.M., Kravstov, Yu. A., and Tatarskii, V.I., 1987, *Principles of Statistical Radiophysics*, Springer-Verlag, New York, Vol. 3, Chapter 3.

Schock, A., Mukunda, M., Or, C., and Summers, G., 1995, "Analysis, Optimization, and Assessment of Radioisotope Thermophotovoltaic System Design for an Illustrative Space Mission," *AIP Conference Proceedings 321: The First NREL Conference on Thermophotovoltaic Generation of Electricity*, American Institute of Physics, New York, pp. 331-356.

Siegel, R., and Howell, J.R., 1981, *Thermal Radiation Heat Transfer*, 2nd ed., McGraw-Hill, New York, pp. 541-542.

Stefan, J., 1879, "Über die Beziehung zwischen der Wärmestrahlung und der Temperatur," *Sitzber. Akad. Wiss. Wien.*, Vol. 79, pp. 391-428.

Tien, C.L., and Chen, G., 1992, "Challenges in Microscale Radiation and Conduction Heat Transfer," *1992 ASME Winter Annual Meeting*, November 8-13, Anaheim, CA.

Tien, C.L., and Cunnington, G.R., 1973, "Cryogenic Insulation Heat Transfer," *Advances in Heat Transfer*, Academic Press, New York, Vol. 9, pp. 349-417.

Whale, M.D., and Cravalho, E.G., 1997, "Analysis of the Enhancement of Thermal Radiation between Closely-Spaced Surfaces Due to Microscale Phenomena," to be presented at the *1997 National Heat Transfer Conference*, Aug. 8-10, Baltimore, MD.

Whale, M.D., and Cravalho, E.G., 1997, "Regimes of Microscale Radiative Transfer for the Exchange of Thermal Energy between Closely-Spaced Metallic Surfaces," to be presented at the *1997 National Heat Transfer Conference*, Aug. 8-10, Baltimore, MD.

White, D.C., and Hottel, H.C., 1995, "Important Factors in Determining the Efficiency of TPV Systems," *AIP Conference Proceedings 321: The First NREL Conference on Thermophotovoltaic Generation of Electricity*, American Institute of Physics, New York, pp. 425-456.

Wilson, A. H., 1953, *The Theory of Metals*, Cambridge Press, London, Chapter 9.

Wilt, D.M., Fatemi, S.R., Hoffman, Jr., R.W., Jenkins, P.P., Scheiman, D., Lowe, R., and Landis, G.A., 1995, "InGaAs PV Device Development for TPV Power Systems," *AIP Conference Proceedings 321: The First NREL Conference on Thermophotovoltaic Generation of Electricity*, American Institute of Physics, New York, pp. 210-220.

Wojtczuk, S., Gagnon, E., Geoffroy, L., and Parodos, T., 1995, "$In_{1-x}Ga_xAs$ Thermophotovoltaic Cell Performance vs. Bandgap," *AIP Conference Proceedings 321: The First NREL Conference on Thermophotovoltaic Generation of Electricity*, American Institute of Physics, New York, pp. 177-187.

Wooten, F., 1972, *Optical Properties of Solids*, Academic Press, New York.

Xu, J.B., Läuger, K., Möller, R., Dransfield, K., and Wilson, I.H., 1994, "Heat Transfer between Metallic Surfaces at Small Distances," *J. Appl. Phys.*, Vol. 76, pp. 7209-7216.

Yakovlev, V.A., 1994, "Modeling of InGaAs Optical Constants and its Application to Spectroscopic Ellipsometry Study of Strained InGaAs/AlGaAs Based Structures," in *Compound Semiconductor Epitaxy*, eds. C.W. Tu, L.A. Kolodziejski, and V.R. McCrary, Material Research Society Symposium Proceedings, Vol. 340, pp. 373-378.

Zhang, Z.M., Le, T.A., Flik, M.I., and Cravalho, E.G., 1992, "Infrared Optical Constants of the High-T_C Superconductor $YBa_2Cu_3O_7$," *1992 ASME Winter Annual Meeting*, November 8-13, Anaheim, CA.